Study of Stress Measurement Using Polariscope

A Thesis
Presented To
The Academic Faculty

By

Fang Li

In Partial Fulfillment
of the Requirements for the Degree
Doctor of Philosophy in Mechanical Engineering

Georgia Institute of Technology

August 2010

Study of Stress Measurement Using Polariscope

Approved by:

Dr. Steven Danyluk
Manufacturing Research Center
Georgia Institute of Technology

Dr. Shreyes Melkote
School of Mechanical Engineering
Georgia Institute of Technology

Dr. Jianmin Qu
School of Mechanical Engineering
Georgia Institute of Technology

Dr. Ajeet Rohatgi
School of Electrical and Computer Engineering
Georgia Institute of Technology

Dr. Dennis Hess
School of Chemical & Biomolecular Engineering
Georgia Institute of Technology

Date Approved: May 4, 2010

Dedicated to my daughter

Anne X. Li

for all the happiness she brings

Acknowledgements

First, I want to express my sincere gratitude to my advisor, Prof. Steven Danyluk, of the Georgia Institute of Technology, for all the support and guidance throughout my PhD study. I also wish to acknowledge Prof. Ajeet Rohatgi, Prof. Jianmin Qu, Prof. Shreyes Melkote and Prof. Dennis Hess of Georgia Institute of Technology, my committees, with all their helps.

I would also like to thank my lab mates for their support and advice. Special thanks go to Kevin, for his help in the experiments.

Finally I am greatly indebted to my wife, my parents and my daughter for their endless encouragement, support and love.

TABLE OF CONTENTS

List of Tables

List of Figures

List of Symbols

δ	photoelastic retardation
θ	isoclinic angle (principle stress orientation)
I_m	background light intensity in phase-stepping
I_a	light source power
σ_1, σ_2	in plane principal stresses
σ_x, σ_y	normal stresses along x and y respectively
τ_{xy}	shear stress in xy plane
λ	illumination wavelength in the photoelasticity setup
t	effective thickness
h	beam height
M	moment of four-point bending
I	bending inertia
E	Young's modulus
τ	shear stress
$\tau_{\max}$	principal shear stress
φ	Crystal grain orientation
C	isotropic stress-optic coefficient
$C(\theta)$	anisotropic stress-optic coefficient as a function of principle stress orientation
$C(\theta, \varphi)$	anisotropic stress-optic coefficient as a function of principle stress orientation and crystal grain orientation

SUMMARY

The goal of this research was to investigate an experimental infrared transmission technique to extract the full stress components of the in-plane residual stresses in thin multi crystalline silicon wafer, and try to meet the need of photovoltaic industry to in situ measure residual stress for large cast wafers.

Previous research has built a circular polariscope system to measure the maximum shear stress in silicon wafers. The error of the system was analyzed and the resolution of the system was about 1.2 MPa. In this research, a new polariscope system has been designed and built. The system is capable of measuring wafers as large as 156×156mm. Anisotropic stress optic law was proposed in this research and stress optic coefficients were calibrated for different grain orientations and stress orientations. The variation of the maximum stress optic coefficients is about 1.7 times of the minimal ones.

System ambiguity at the boundaries was resolved completely by introducing a new function. Shear different method was used to obtain full stress components by integrating the shear stress map from the boundaries. The integration error was about 1 MPa within 10mm from the starting point of the integration, which was verified by a four point bending CZ single crystal wafer beam.

Chapter 1

Introduction

This thesis investigated stress measurement using polariscope for thin, flat crystalline solids and was applied to multi-crystal silicon as a model material. The anisotropic properties of silicon in the measurement were studied and the anisotropic stress optic coefficients were characterized for different crystal and stress orientations. A new system setup of polariscope was developed to measure large samples. Then the full stress components were extracted from the measurement of the polariscope by the shear difference method. Finally, the thermally induced stress was modeled using ANSYS.

The background of this research is introduced in chapter 2 and an introduction to photoelasticity is described in chapter 3. The research plan is introduced in chapter 4 and the description of this research begins at chapter 5, which summarizes how to characterize the crystal grain orientation and how to obtain stress optic coefficients for different crystal orientations and stress orientations. Crystal grain orientations were characterized by the light transmission intensity. Four point bending experiments were used to calibrate the anisotropic stress optic coefficients for each grains.

Chapter 6 describes the new setup of the polariscope used in this research. Location dependent stress optic coefficients were obtained for the new setup using four point bending experiments. Those coefficients were applied to calculate the maximum shear stress for the entire wafer field. Calibration results showed that the system would have approximately a 35% error without using the location dependent stress optic coefficients.

Chapter 7 presents the methodology to extract full stress components using the shear difference method. The system ambiguity of the polariscope was resolved by using arctan2 function. Finally by applying boundary conditions and using shear different method, the full stress components were obtained.

Chapter 8 summarizes the finite element method models used to study the thermal stress induced by the light source and the analysis proved that the thermal stress was negligible.

Chapter 9 summarizes the systematic and random errors of the system. The response of the infrared camera to light power was tested and linearly adjusted. The procedure to align the polariscope system was also introduced.

Chapter 2

Background

2.1 Summary

The chapter summarizes the literature review of residual stress in thin silicon wafers. First, the sources of residual stresses in silicon are described. Then the residual stresses measurement techniques are reviewed. Finally the approach for residual stress measurement is presented.

2.2 Sources of Residual Stresses in Silicon Wafers

The photovoltaic (PV) industry uses single and polycrystalline crystal silicon in the manufacturing of PV modules. Single crystal wafers are usually grown from the melt into ingots by the Czochralski (CZ) method [1] as shown in figure 2.1. The Czochralski method is used for high volume production of single crystal silicon. A crystal is "pulled" out of a vessel containing liquid silicon by dipping a seed crystal into the liquid which is subsequently slowly withdrawn at a surface temperature of the melt just above the melting point. The diameter of the ingot is determined by the pulling rate and the temperature profile.

Multi crystalline silicon is produced either by the edge-defined film (EFG) growth method [2] or by casting. Wafers produced by the EFG method use a die to define the

thickness of a silicon wafer as shown in figure 2.2 (a). By adjustment of the temperature profile of the graphite die, the silicon sheet crystallizes with large grains. Usually the shape of the ingot produced by the EFG method is large polygons. Recently the technique has been used to produce large cylinders of material as shown in figure 2.2 (b). The large cylindrical material needs to be flattened out for further processing.

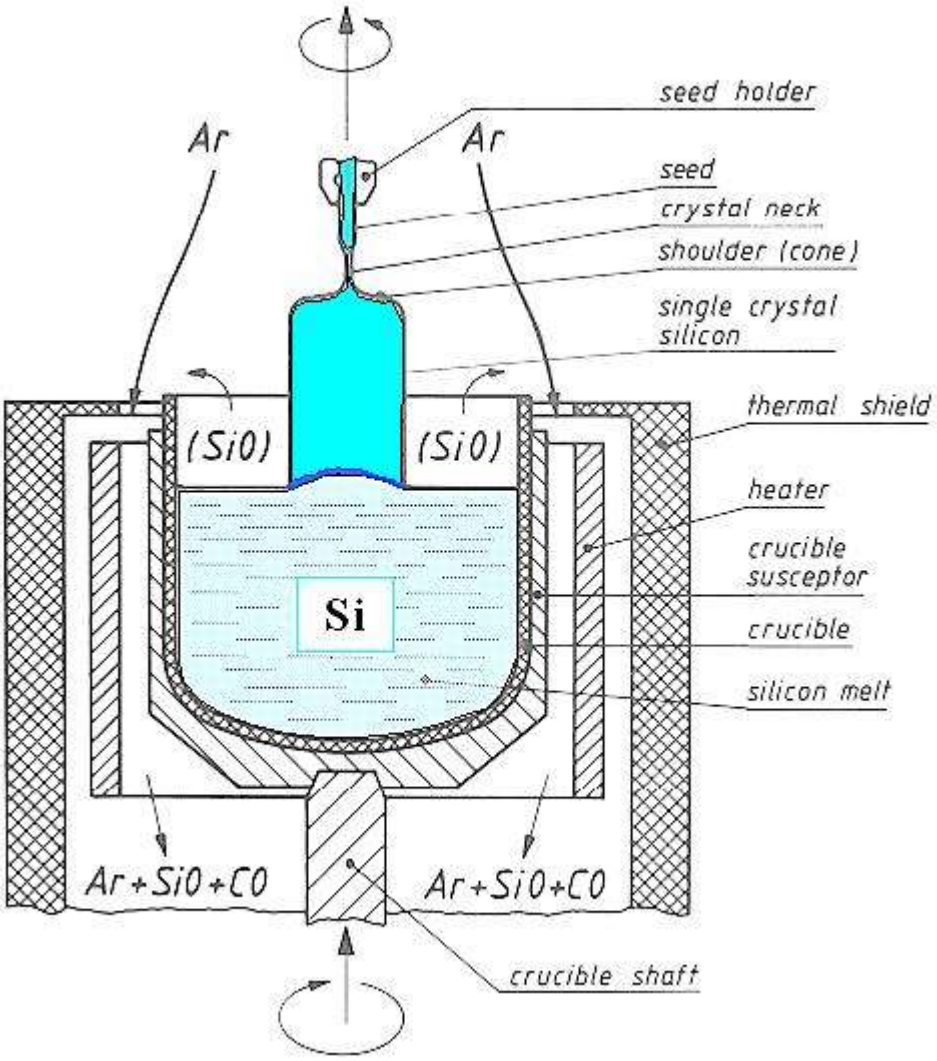

Figure 2.1 Schematic of the CZ growth process.

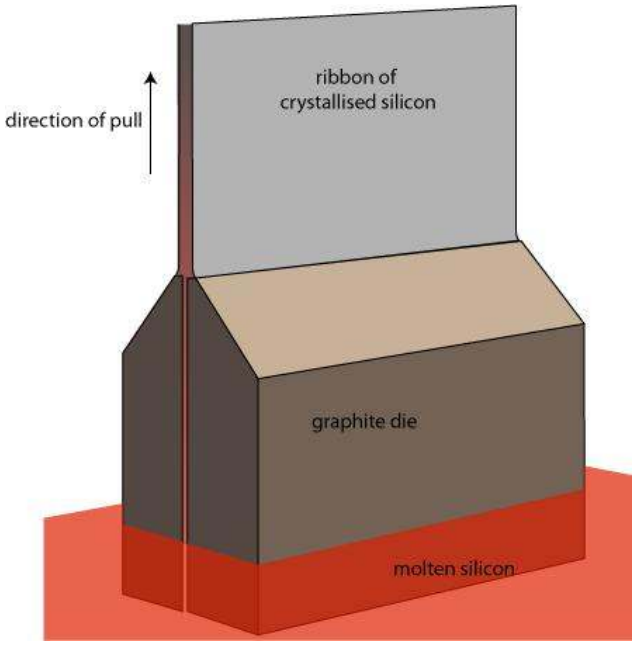

(a) In EFG, the growth is defined by the gap between the two graphite dies.

(b) Photograph of Large thin-walled cylinders grown by EFG process.

Figure 2.2 Edge defined film growth method.

Casting is also used to produce multi crystalline silicon. In the photovoltaic industry, about 60% of solar cells are made from cast wafers with a typical efficiency of 13–16.5% [3] [4]. Multi crystalline silicon is usually cast in a fused silica crucible supported by graphite as shown in figure 2.3. Typically, crystallization starts at the bottom of the crucible where the temperature is lowered below the melting temperature (1450^0C) of silicon [5].

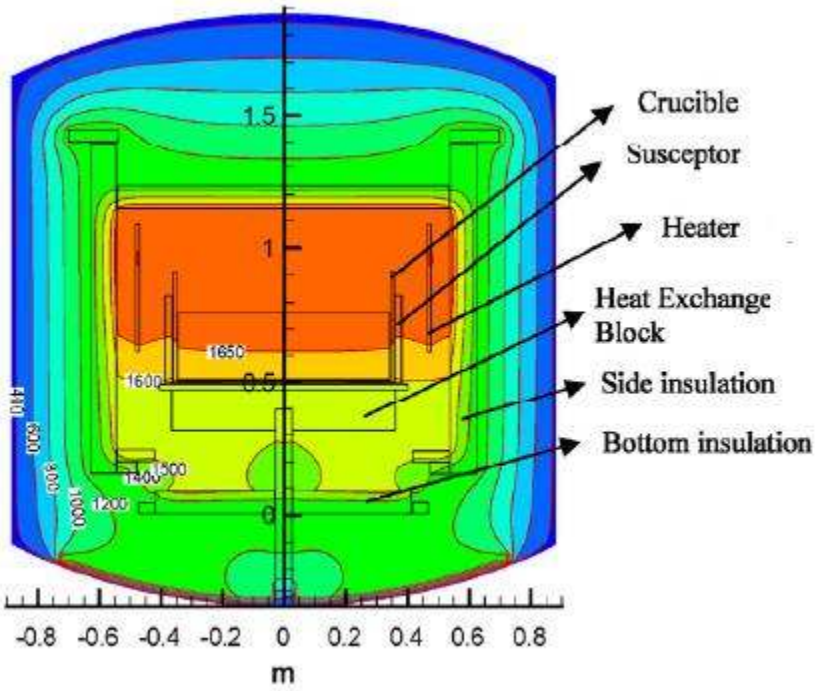

Figure 2.3 Schematic of casting process.

After casting, silicon wafers are produced by sawing. Microelectronic circuits or photovoltaic devices are fabricated on these substrates through various chemical, physical and thermal processes.

During the growth of EFG, the temperature of the silicon melt is 1450^0C, and it drops to room temperature within 0.5 m from the solid-melt interface, therefore, a high thermal gradient is unavoidable at the solid-melt interface. A similar situation occurs during the crystallization of cast wafers as shown in figure 2.3. Thermal gradients can not be removed completely although techniques such as, heat exchange method (HEM) system [6] can reduce the thermal gradient. The magnitude of the thermal stresses is approximately proportional to the curvature of the temperature profile [7]. For this reason, modeling of residual stress usually involves knowledge of the temperature profile, as seen in the work of Bhihe et. al. [8] and Lambropoulos et. al. [9]. The following thermal processing in cell manufacturing such as oxidation and diffusion may also introduce non-uniform heating and cooling which results in a substantial thermal gradient and may introduce additional residual stresses. A combination of thermal and mechanical stresses caused during the production is frozen into the wafers in the form of strain, which can be reduced but not completely removed by post growth annealing [10].

2.3 Effects of Residual Stresses in Silicon Wafer

Residual stresses may enhance the performance of a mechanical structure and the effects of residual stresses on fatigue are covered in detail elsewhere [11]. Residual stresses can raise or lower the mean stress experienced over a fatigue cycle and an example of how this influences metal structures can be seen in the improvement of the fatigue life. The

static loading performance of brittle materials can be improved markedly by the use of residual stresses. Common examples include thermally toughened glass [12] [13] and pre-stressed concrete [14] [15]. For plastically deformable materials, the residual and applied stresses can only be added together directly until the yield strength is reached. In this respect, residual stresses may accelerate or delay the onset of plastic deformation.

In many cases, unexpected failure is due to the presence of residual stresses which have combined with the service stresses to shorten component life. Furthermore, in natural or artificial multiphase materials, residual stresses can result in differences in thermal expansion, yield stress, or stiffness. Residual stresses in silicon may cause mechanical failure during processing and change the optical or electrical properties of the wafer. Tensile residual stresses in silicon will lead to crack growth and reduced electron-hole lifetime and wafer breakage. High tensile stresses will also cause unexpected failure during processing of cells when service stresses are introduced. Furthermore, the regions close to the wafer edges may contain micro-cracks which will eventually propagate and fracture the cell in handling during subsequent device fabrication [16] since cracks will propagate in the region of tensile residual stresses.

As strain due to thermal gradient is introduced during growth, the crystal will relieve the residual stresses by the generation and propagation of dislocations. The relationship between residual stresses and dislocation density in silicon wafers was studied by V. Garcia and an inverse correlation was found between residual stresses and dislocation etch pits [17]. It is believed that this will eventually impact the lifetime and thus the efficiency of photovoltaic cells [18]. As sheet becomes thinner, the grown-in residual stresses, coupled with the stresses imposed during manufacturing, presents a formidable

challenge. There has been a significant effort to develop non-destructive techniques that expose the in-plane residual stresses [19] [20], but that prior work is neither fast enough nor sensitive enough to implement in the manufacturing of solar cells. Our work has focused on developing a robust, non-destructive optical method to determine the stress state in a whole field view of thin silicon sheet.

2.4 Overview of Stress Measurement Techniques

All stress measurement techniques can be divided into one of two classes: one measures actual strain, and the other measures changes in strain. Residual stress measurement techniques may also be classified by whether the technique is destructive or non-destructive. The choice of a measurement technique should be based on the kind of information needed so it is important to recognize the limitations of each technique. Non-destructive methods are needed for in situ quality monitoring for photovoltaic processing. The most common used non-destructive methods are x-ray diffraction, ultrasonic microscopy, shadow Moiré, neutron diffraction and photoelasticity.

X-ray diffraction [21] detects the strain-induced changes in the crystal lattice, which can then be used to obtain the residual stresses. The sensitivity of this technique is reported to be around 10 MPa [22] [23]. X-ray diffraction measures strains within the surface depending on the x-ray source. Penetration of the specimen by the x-ray beam is related to a number of factors, including material density and beam energy. Generally speaking, the information in the diffracted beam comes from a volume that is about 8 to 20μm below the surface [24] and the volume is always slightly larger than the beam size due to scattering.

Ultrasonic microscopy [25] [26] refers to the measurement of residual stresses by the propagation of acoustic waves in a medium under different stresses. Changes in ultrasonic speed can be observed when a material is subjected to stress, the changes providing a measure of the stress averaged along the wave path. The acoustoelastic coefficients necessary for the analysis are usually calculated using calibration tests. A main difficulty of this technique is that the relative change in wave speed is very small, typically of the order of 10^{-5} MPa^{-1}[27]. The method provides a measure of the macro-stresses over large volumes of material. Ultrasonic wave velocities can depend on micro-structural inhomogeneities [28] and there are difficulties in separating the effects of multi-axial stresses. Therefore acoustoelastic microscopy essentially is especially useful in materials uniform both in microstructure and composition, such as single crystal silicon.

Shadow Moiré can detect the residual stresses in circular or rectangular plates. The technique depends on deforming sample and then comparing the deformation to an analysis and deflection. Danyluk and his group [29-33] have developed the analytical theory for beam, rectangular and circular plates and used this analysis to extract residual stresses from the displacement measured by shadow Moiré. The limitation of this method is that a certain profile needs to be assumed for the residual stresses. For example, an axis-symmetrical profile is assumed for circular plate. Since the residual stresses are forced to comply with the assumed profile, this technique is not sensitive to the local stress concentrations.

Neutrons have the advantage over x-rays since the wavelengths are comparable to the atomic spacing and their penetration into engineering materials is typically many

centimeters [34]. The technique allows for collection of a full stress tensor, or simple tri-axial stresses, depending on how many vectors are measured. Beam penetration is about 152 mm in aluminum, 38 mm in iron and steel, and varies significantly in materials such as titanium and zirconium [35]. Unfortunately, since this technique requires a nuclear reactor to supply the neutrons, it is limited to access to these facilities and the technique can be prohibitively expensive.

In the last number of years we have worked on various experimental techniques to obtain the in-plane residual stress in silicon, especially in poly-crystalline silicon, in order to improve the efficiency and reliability of photovoltaic cells. Wafers used in the photovoltaic industry are becoming larger and thinner. The residual stresses are generally higher in thin materials and it takes more effort to measure bigger samples. Fundamental work on the development of a non-destructive and non-contact residual stress measurement technique for solar silicon wafers has been carried out by Professor Danyluk and his group in the last few years [36-40]. This work has resulted in an IR-polariscope based method for such measurements. The system developed to-date is able to measure the in-plane maximum shear residual stress distribution in silicon wafers of thickness ranging from 100μm to 2mm and sizes of up to 156×156 mm. This technique measures the stress-induced birefringence, which is proportional to the magnitude of the residual stresses, by measuring the change in the polarization state of the transmitted light. The residual stresses are determined from an expanded anisotropic stress optic law. This technique senses strain directly as opposed to Shadow Moiré, whose accuracy is often deteriorated by the differentiation of the measured displacement. Furthermore we use the phase-stepping technique, which provides a fast and automatic way to extract the

principal shear stress and its orientation. System ambiguities are resolved by introducing a new function. A new system setup was built to enable the measurement of full field wafers as large as 156×156 mm. Furthermore, the new system can capture the whole boundary conditions properly. Finally, using the shear difference method, the full stress components are calculated from the photoelasticity parameters.

2.5 Overview of Photoelasticity

The photoelastic phenomenon was first described by Brewster [41] [42] and extended by the works of Coker and Filon of the University of London. In 1853, Maxwell related the birefringence to stress and developed the stress-optical laws. Coker and Filon [43] applied this technique to structural engineering in 1902.

Photoelasticity is an experimental method to determine the stress distribution in a material where mathematical methods become quite cumbersome. Unlike the analytical methods of stress determination, photoelasticity gives a fairly accurate picture of stress distribution even around abrupt discontinuities in a material. The method serves as an important tool for determining the critical stress points in a material and is often used for determining the stress concentration factors in irregular geometries.

The method is based on the property of birefringence, which is exhibited by certain transparent materials. Birefringence is a property where a ray of light passing through a material experiences two refractive indices. The property of birefringence or double refraction is exhibited by many optical crystals. But photoelastic materials exhibit the property of birefringence only on the application of stress and the magnitude of the refractive indices at each point in the material is directly related to the state of stress at

that point. When a ray of light passes through a photoelastic material, it becomes polarized and gets resolved along the two principal stress directions and each of these components experiences different refractive indices. The difference in the refractive indices leads to a relative phase difference between the two component waves, which is usually called phase retardation as shown in figure 2.4. The magnitude of the relative retardation is given by the stress optic law.

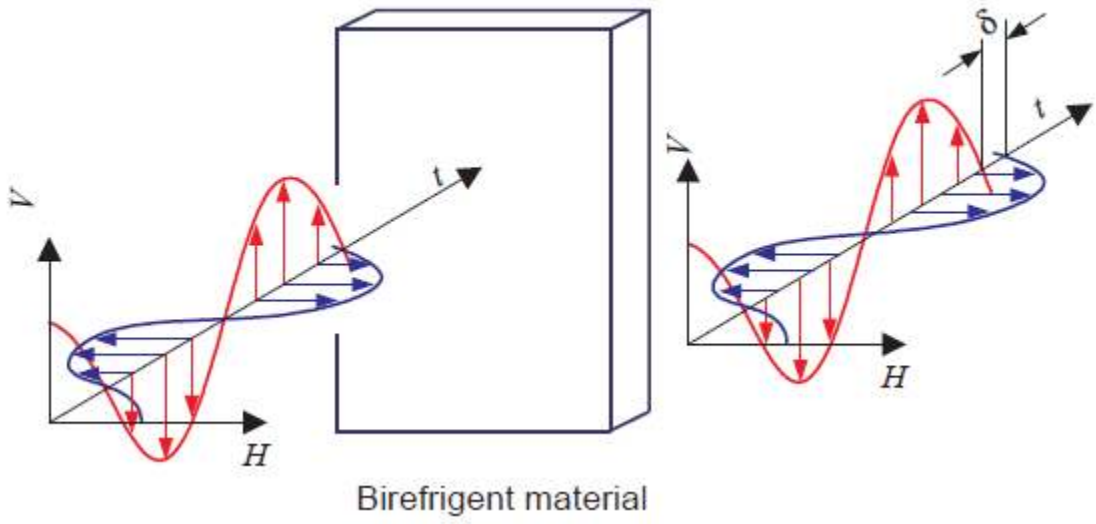

H : Horizontally polarized
V: Vertically polarized
δ: Phase retardation
Figure 2.4 Schematic diagram showing the effect of birefringence.

Photoelasticity can be applied to three and two dimensional states of stress [44]. However the application of photoelasticity to the two dimensional plane stress system is much easier to analyze especially when the thickness of the sample is much smaller as compared to dimensions in the plane. In this case, the only stresses act in the plane of the

solid, as the other stress components are zero. The experimental setup varies from experiment to experiment but the two basic kinds of setup used are the plane and circular polariscope.

A commonly used technique to obtain the photoelasticity parameters is phase stepping. The phase stepping concept for photoelasticity was first introduced by Hecker and Morche [45] in 1986, who used plane and circular polariscopes to extract isochromatic and isoclinic angle respectively. This technique records multiple images, normally three to six images, corresponding to different optical arrangements and uses the image intensities to solve for the photoelastic parameters for each pixel. A six step phasing method is used to extract the photoelastic parameters from the measurement in the current research. Calibration methods (four point bending) and full-field illumination have been used to calibrate the stress optic coefficients, increase system resolution and produce full field stress.

Researchers have spent a good deal of effort in obtaining full components of the stresses from the measured maximum shear stresses. The first step is to resolve the ambiguity of the photoelastic parameters, including isoclinic and isochromatic phase maps. In this research, isoclinic angle will first be extended from $[-\pi/4, \pi/4]$ to $[-\pi/2, \pi/2]$ using arctan2 function. Applying the shear difference method, the full components of stresses can be found by accurately introducing the boundary conditions.

2.6 Conclusions

A brief description of wafer production was given and techniques for residual stress measurement for silicon wafers were discussed. A circular polariscope based on the theory of photoelasticity was chosen for this research based on the accuracy and the potential for in situ stress measurement.

Chapter 3

Introduction to Photoelasticity

3.1 Summary

This chapter describes the principles of the polariscope and it's relation to silicon, and the procedure used for phase stepping.

3.2 Principles of Photoelasticity

When light passes through a homogeneous isotropic media, such as glass, it is governed by the Snell's Law of refraction and reflection as shown in figure 3.1. The figure describes the reflection and refraction of an incoming light ray. The reflected light (R) is plane polarized and the refracted light (r) is a single light ray without polarization.

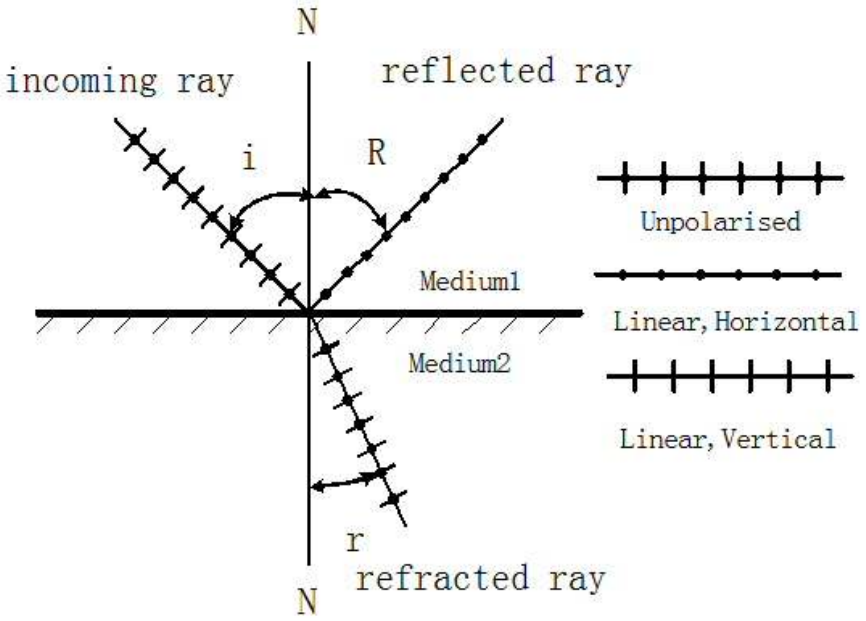

Figure 3.1 Snell's Law for an isotropic medium.

Certain crystalline solids, such as silicon carbide, which are optically anisotropic [46], will refract a single incident ray and produce two refracted rays, called ordinary (r_1) and extraordinary (r_2) rays, as shown in figure 3.2. This phenomenon is called double refraction or birefringence. One of the refracted rays is extraordinary in the sense that it violates Snell's law so that the ray in an anisotropic solid travels at a different speed and direction to that of the ordinary ray. The two indices of refraction for the ordinary and extraordinary rays are equal only in the direction of an optic axis. An optical axis is a line along which there is some degree of rotational symmetry in an optical system such as a camera lens or microscope. In a doubly refracting crystal, the optical axis is the line in the direction of which no double refraction occurs. The ordinary and extraordinary rays are plane polarized and their planes of polarization are orthogonal.

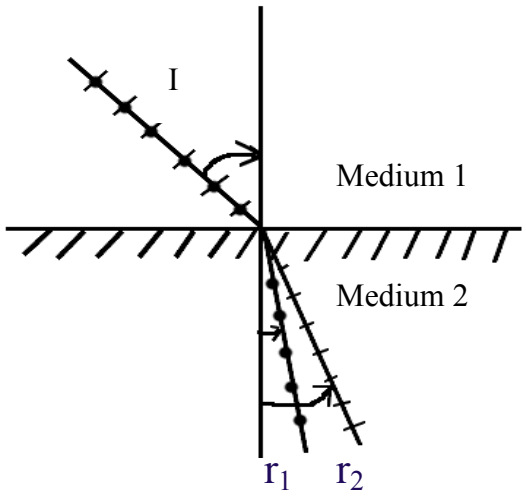

Figure 3.2 Diagram showing the passage of light through an anisotropic crystal media.

If the incident rays are parallel to the optic axis, the ordinary ray and the extraordinary ray will travel in the same direction and behave as if in an isotropic medium. However, if the incident light ray is perpendicular to the optic axis, the extraordinary ray will travel faster but in the same direction as the ordinary ray. The photoelastic phenomenon occurs when the incident rays are perpendicular to the optic axis. The two rays coming out of the crystal are then perpendicular and polarized. When the light emerges, the relative phase difference between the refracted rays will form fringes.

3.3 Photoelasticity for Crystalline Silicon Wafer

Crystalline silicon is diamond cubic [47] and there is no double refraction effect in the stress free state. The existence of stress will induce strain which results in optically anisotropic behavior. Silicon wafers are generally thin flat plates and assumed to exhibit plane stress. As mentioned above, photoelasticity occurs when the incident rays are

perpendicular to the optic axis. It is relatively easy to illustrate how double refraction occurs in the special case of a thin single crystal wafer that is subjected to four point bending as shown in figure 3.3. Figure 3.3 (a) is an illustration of the stress state of a thin silicon beam loading on edge. Figure 2.3 (b) shows an example of atom strain with the assumption that the crystal is simple cubic. The strain at the top part of the beam compresses the atom bonds while the tensile strains at the bottom part of the beam stretch the atom bonds. When unpolarized light passes through the single crystal beam, the electric and magnetic field of the light interacts with the electrons of the atoms. Double refraction occurs due to the strain difference between the horizontal direction and vertical direction. For example, at the top part of the beam, compressive strain in the horizontal direction makes atoms more closely packed compared to the vertical direction, where the strain is zero. Thus the light ray traveling in the horizontal direction is slower than the light ray traveling in the vertical direction. When the two rays emerge, there is phase difference between them. Figure 3.3 (c) is the light transmission intensity image of infrared light transmitted through a simple crystal silicon wafer 0.2 mm thick, undergoing four point bending by an infrared camera. The light transmitted in the middle is more intense than at the edges because of double refraction. Double refraction changes the polarization state of the emerging polarized beam, and this change results in the formation of fringe patterns. Fringes can't be seen for the beam in figure 3.3 because the stress levels and the thickness are small. For comparison, figure 3.4 shows the fringes captured from a polymeric compression disk observed by a polariscope [48], where fringes can be seen clearly.

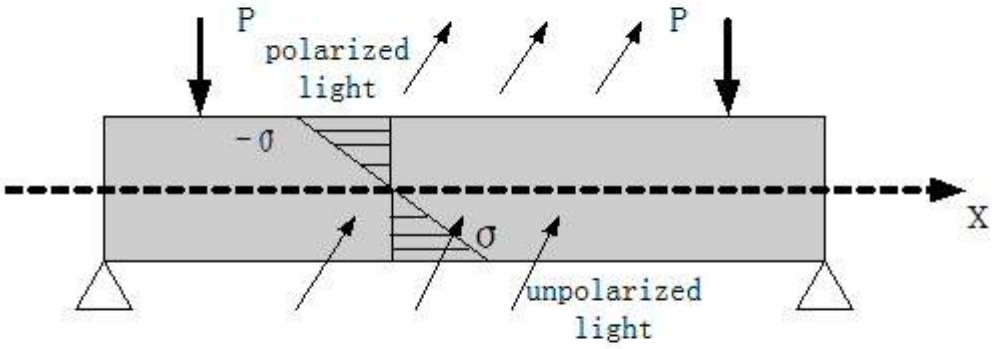

(a) Light passing through a single crystal silicon four point bending beam.

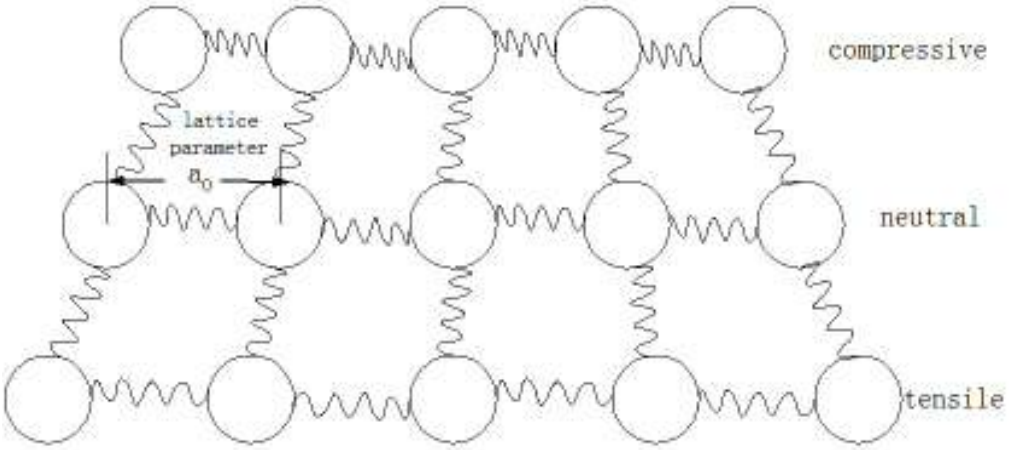

(b) Schematic diagram of a simple cubic atomic arrangement of atoms and the strain under bending.

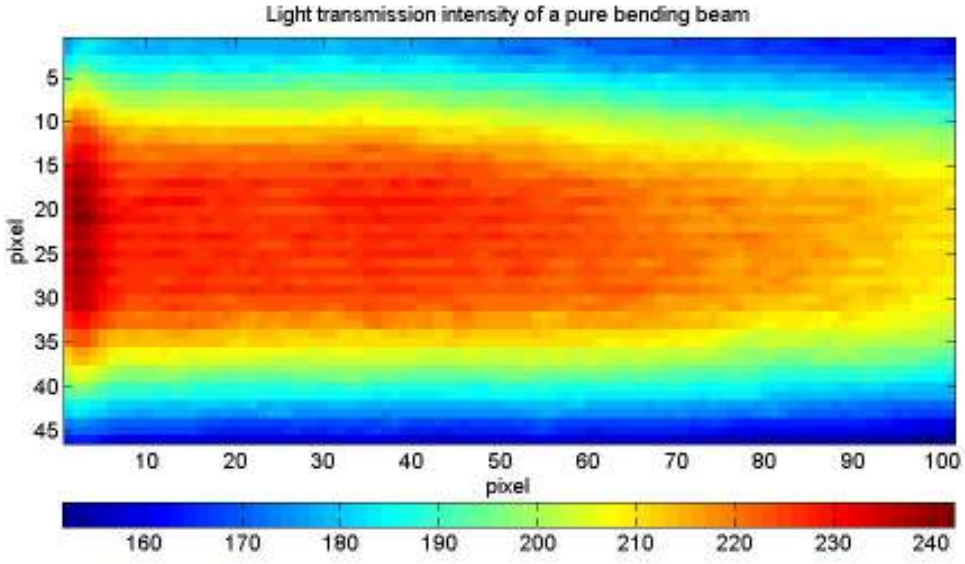

(c) Light transmission intensity of the pure bending region.

Figure 3.3 Demonstration of stress induced double refraction.

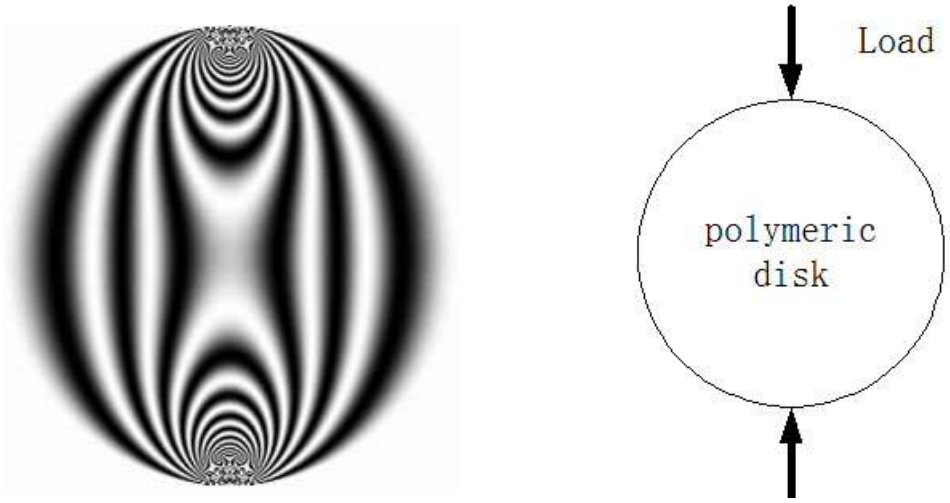

Figure 3.4 Fringes of a polymeric disk under compression.

The experimental setup to capture birefringence is called a polariscope. A polariscope can convert birefringence into fringes and the number of the fringes is proportional to the stress magnitude. The experimental results obtained from the polariscope are photoelastic parameters, namely isochromatic and isoclinic, which represent the magnitude and direction of the principal stresses respectively. The photoelastic parameters are converted to maximum shear stress using an isotropic or anisotropic stress-optic law. In 1853, Maxwell related the birefringence to stress through the stress-optical law which is expressed in equation 3.1.

$$2\tau_{max} = |\sigma_1 - \sigma_2| = \frac{\lambda}{2\pi t C}\delta \qquad (3.1)$$

Where C is the stress-optic coefficient, t is the thickness of the sample ， λ is the wavelength of the light source, and σ_1, σ_2 are the two principal stresses . δ is the phase difference between the two refracted rays, and is called phase retardation. τ_{max} is the

maximum shear stress and related to the absolute value of the difference between the largest and smallest principle stresses.

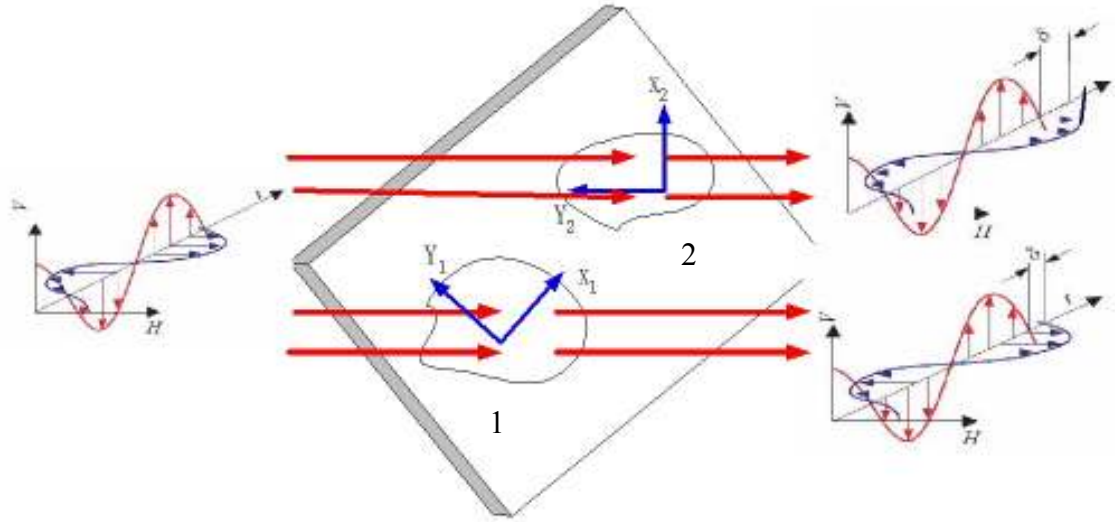

Figure 3.5 Demonstration of light transmissions through stressed multi crystalline silicon.

Figure 3.5 demonstrates how the stress optic law relates to a multi-crystalline material such as silicon. In Figure 3.5 the stressed sample contains two different grains which are stressed with different stress magnitudes. Since the stress magnitude is different for the two grains, the phase difference of the refracted rays is also different, which results in different light transmission.

3.4 Light Transmission through Silicon

When light passes through a crystalline solid, the photons interact with the atoms of the solid, where some photons are absorbed with a wavelength shorter than the band gap and converted to charge carriers and others are transmitted. The transmission spectrum for silicon in Figure 3.6 shows that silicon is opaque to the ultraviolet and visible light but the transmission ratio rises sharply to over 50% around 1100 nm, being almost constant in the whole near infrared spectrum range. A wavelength of 1150 nm, which is close to the edge of the transparent window, was chosen as the light source for the experiments done in this thesis. This wavelength is obtained using an interference band pass filter with a bandwidth of 10 nm.

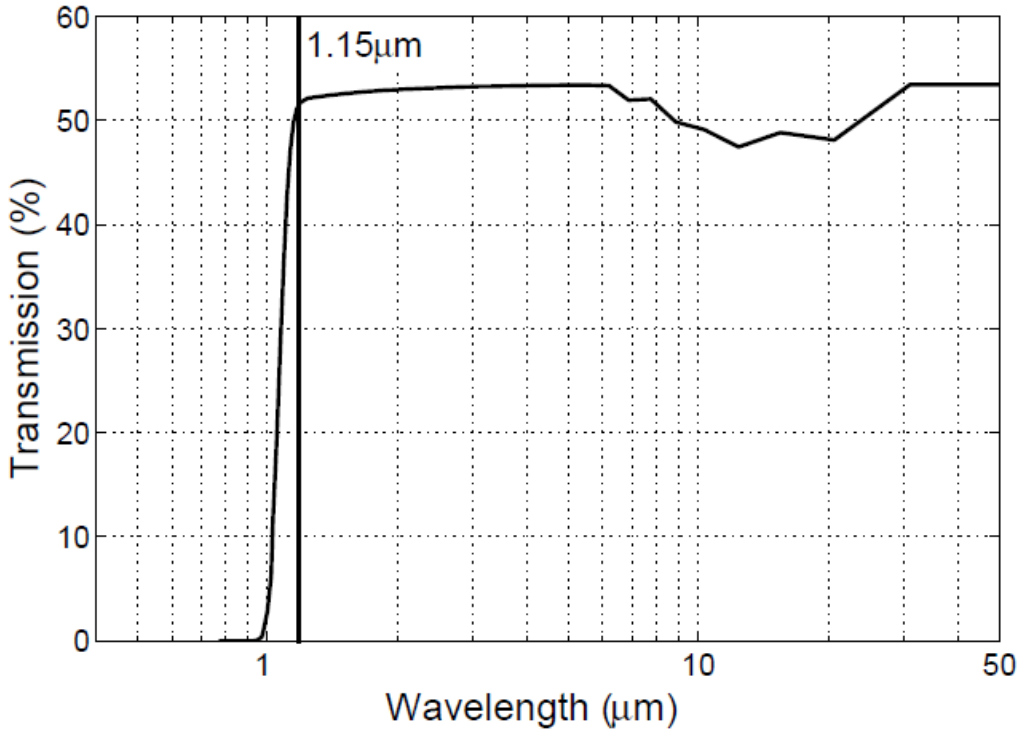

Figure 3.6 Transmission spectrum of silicon.

The light transmission spectrum is related to the band gap of crystal silicon. The band gap generally refers to the energy difference between the top of the valence band and the bottom of the conduction band. It is the amount of energy required to raise a valence electron into the conduction band.

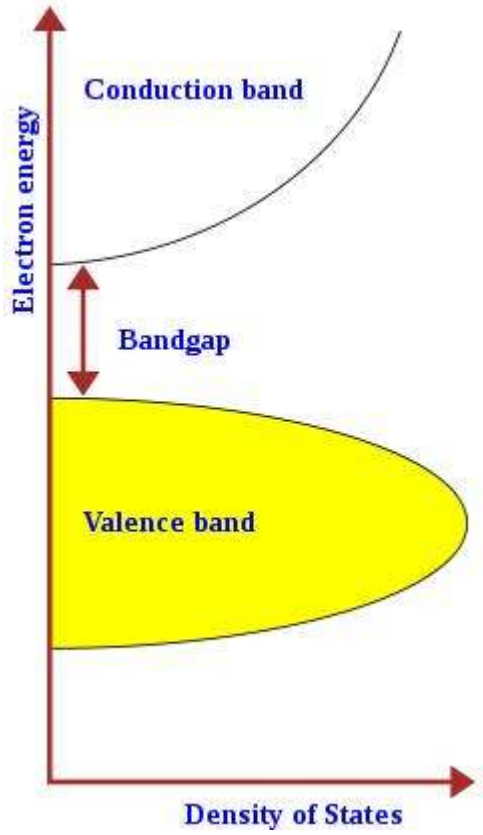

Figure 3.7 Schematic diagram of the band gap of a semiconductor.

Figure 3.7 is a crude schematic of the band gap in a semiconductor. For crystal silicon, at room temperature, the band gap is approximately 1.1eV. Photons that contain energy higher than the band gap will be absorbed. The wave length of the photon containing

energy with1.1eV is about 1.15um. Thus most of the visible light is absorbed and only the IR light is transmitted.

3.5 Experimental Setup of the Circular Polariscope

Figure 3.8 shows a schematic diagram of the principle features of a circular polariscope [49] [50]. The setup includes a white light tungsten-halogen lamp, two spherical lenses 240 mm in diameter, two near infrared linear polarizers 100 mm in diameter, two first-order quarter waveplates with a wavelength of 1150 nm and 100 mm in diameter, two beam splitters of 240 mm in diameter, a specimen stage, a spatial filter, an interference filter with a wavelength of 1150 nm and half magnitude full width (HMFW) of 10 nm, an imaging lens of 75 mm in diameter, an Electrophysics high-sensitive infrared video camera, a image grabber board and a computer. The system is placed on an optic table, and can be used to measure samples as large as 75 mm in diameter.

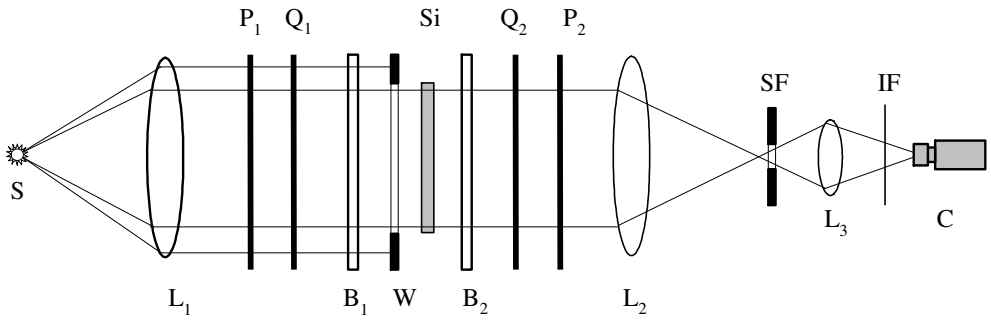

Figure 3.8 Schematic diagram of the system setup of a circular polariscope.

The light emitted from the tungsten light source(S) will pass through the first spherical lens (L_1), where the light beams are collimated. After the beam passes the first polarizer (P_1), the light will be plane polarized, and the optic axis of the first quarter waveplate (Q_1) is kept at 45 degree with the first polarizer. Thus after light passes through the first quarter waveplate, it will be circularly polarized. The purpose of the two beam splitters (B1 and B2) is to increase the sensitivity of the polariscope [37].The light passes through the sample and is reflected back and forth several times, and thus the photoelastic retardation is amplified by the times light travels through the sample.

The opaque window (W) is used to block any unwanted light around the system. When the collimated circularly polarized light enters the sample, double refraction will occur if the sample is stressed. Silicon is acting as a waveplate if it contains residual stresses. The polarization state of the light will be further changed by the sample based on the magnitude of the maximum shear stress and the principle stress orientation. In order to determine the phase change caused by the sample, another quarter waveplate (W2) and polarizer (P2) is used to review the state change of the light. Then light is focused by the second spherical lens (L2). In the case where partial mirrors are used to increase the sensitivity, a spatial filter has to be added in order to pick the correct magnification of the system. Finally another lens (L3) will further focus the light before it enters the camera.

The light source used in this thesis is a tungsten-halogen lamp, whose typical spectrum is shown in Figure 3.9. It covers a broad range in both visible and near infrared regions. As shown in the figure, the band pass filter only selects a bandwidth $\Delta\lambda = 10$ nm, which significantly reduces the light intensity. The lost intensity can be compensated for by using a higher output power of the tungsten-halogen bulb. With a 150 W bulb, the

remaining power after narrow band filtering is over 200 mW, which is acceptable for the full field measurement. To further compensate for the excessive loss in high fringe multiplication, a broad band pass filter with a FMHW of 100 nm can be used at the cost of wavelength mismatch in the quarter waveplates. Using an infrared laser is another choice for the light source, especially for the benefit of reducing the loss in spatial resolution in fringe multiplication. But the self-interference normally dominates the photoelastic fringes of low stress. Therefore, the tungsten-halogen bulb was chosen as the near infrared point light source for the system.

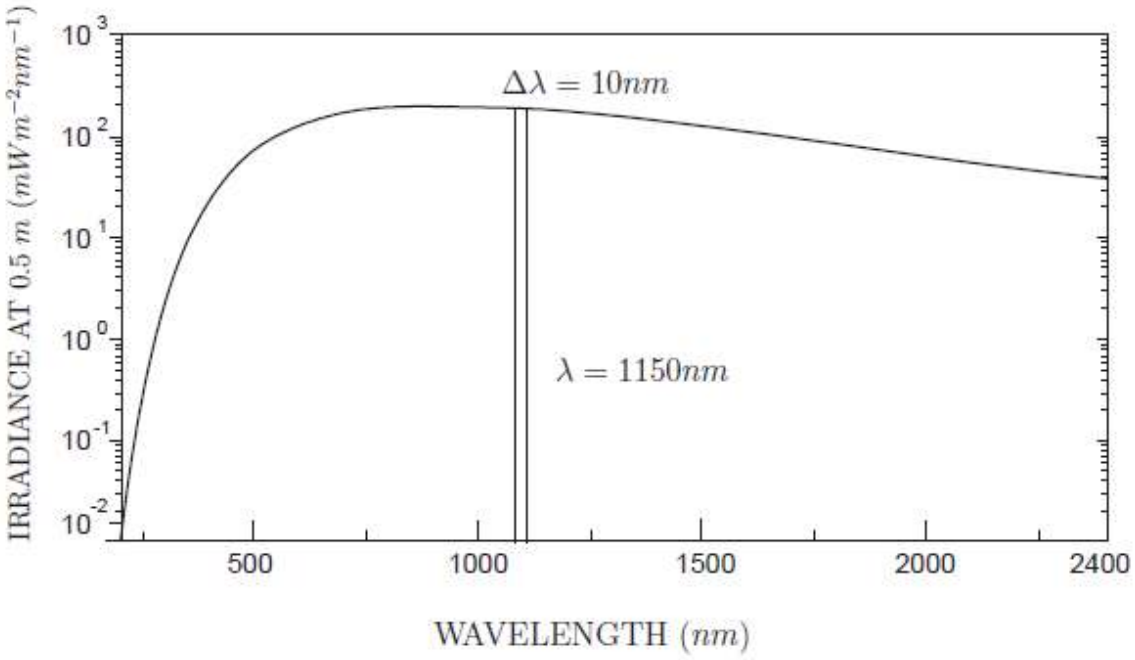

Figure 3.9 The relation between power and wavelength of the tungsten light source.

The camera is connected to an image grabber board installed on a computer. The gray-level images are digitized by the grabber with 640 × 480 pixels and depth of 8 bits, or 256 gray levels. The digitized images normally contain electronic noise, especially when using high camera gains and for dark images, which can result in high inaccuracy for stress calculation. In order to reduce the noise, 30 to 300 sequentially grabbed images were averaged out with respect to the same object, thus the random noise can be minimized at the expense of taking a little more time for grabbing the images. The image grabbing software, TZGrab, is implemented in Microsoft Visual C++ with a Windows interface shown in Figure 3.10. This software is capable of adjusting image contrast and brightness, checking for the saturation, filtering electronic noise and saving images. The optimal images captured are those with highest maximum allowed brightness and reasonable contrast. The brightness is limited by the 256 gray levels of the digitizer. For low stress, normally the first image in the phase stepping has the highest brightness and will be adjusted to the maximum gray level as 255 by increasing the image contrast and brightness or increasing the light power. The saturation of the image can be checked by pressing the “Check” button, which detects the percentage of pixels that are saturated. Usually the percentage is controlled at 0.2% to avoid excessive saturation. The adjustment of the brightness and contrast usually needs to be repeated several times. It should be pointed out that no further adjustment is made during phase stepping.

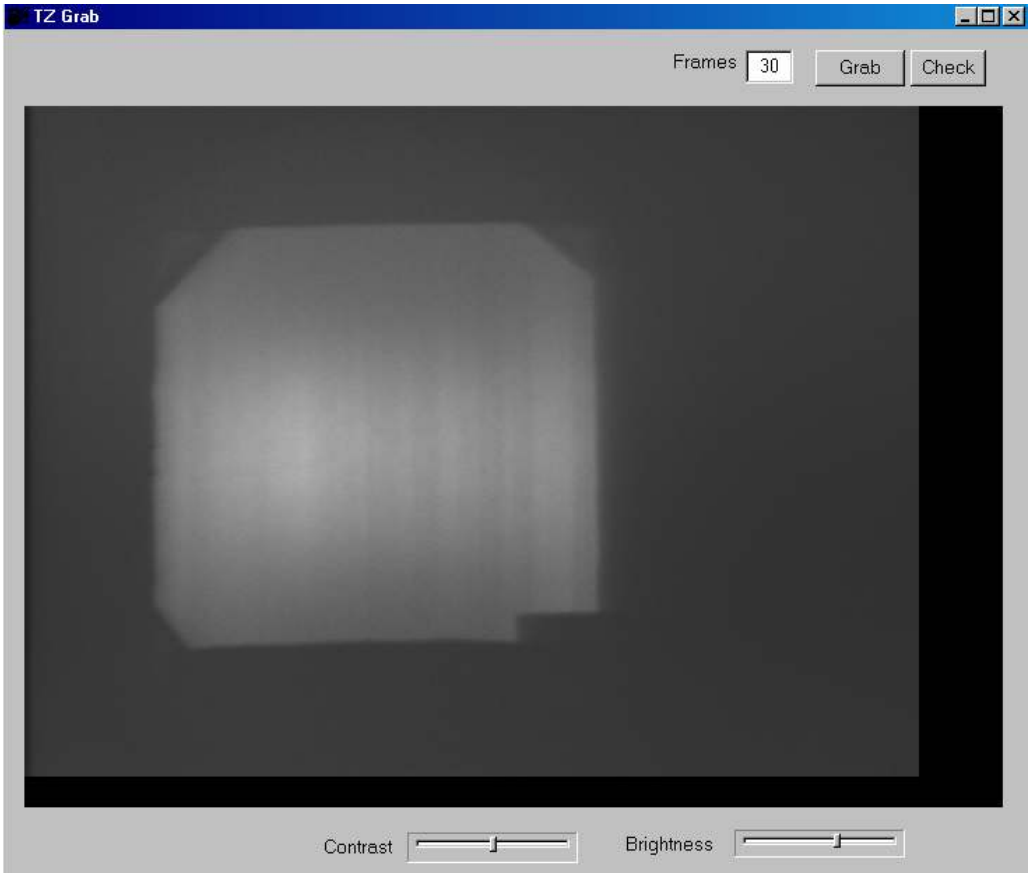

Figure 3.10 Computer image of the Windows interface of image grabbing program.

3.6 Six Phase Stepping

Wafers used for solar cells are generally very thin, usually 100 to 300 um. As can be seen from the stress optic law shown in equation 3.1, the phase difference of the emerging light rays is proportional to the sample thickness. Thus for silicon wafers, only partial fringes can be obtained as shown in figure 3.3(c). Fringes are not present but only the light intensity difference from the edge to the center is seen. Thus stress can't be evaluated by the fringes counting techniques.

Phase stepping is used to extract photoelastic parameters from the transmitted light automatically in the case of partial fringes [51-55]. For a general setup as shown in Figure 3.3, the light emergence from the analyzer is not location dependent and will take the form such as

$$I(x,y) = I_m + I_a\left[\sin 2(\beta-\alpha)\cos\delta - \sin 2(\theta-\alpha)\cos 2(\beta-\alpha)\sin\delta\right] \qquad (3.2)$$

where I is the image captured by the camera, I_m takes account of the stray light; I_a is the light power, which is the intensity emerging when the axes of the specimen and all the optical elements in the polariscope are parallel; α and β are the orientation angles between the reference axis and the slow axis of the analyzer, second quarter waveplate respectively, and θ is the isoclinic angle.

There are four unknowns in equation 3.2, at lease four independent equations need to be used for solving this equation. By selecting six angular combinations of the second quarter waveplate and the second analyzer, as shown in Table 3.1, six simultaneous equations containing the unknowns of phase retardation δ and isoclinic angle θ, are generated, which can be used to solve for these two unknowns.

Table 3.1 Six phase stepping of a circular polariscope.

ϕ	β	Light intensity
0	$\pi/4$	$I_1 = I_m + I_a(1+\cos\delta)/2$
0	$-\pi/4$	$I_2 = I_m + I_a(1-\cos\delta)/2$
0	0	$I_3 = I_m + I_a(1-\sin 2\theta\sin\delta)/2$
$\pi/4$	$\pi/4$	$I_4 = I_m + I_a(1+\cos 2\theta\sin\delta)/2$
$\pi/2$	$\pi/2$	$I_5 = I_m + \frac{I_a}{2}(1+\sin 2\theta\sin\delta)$
$3\pi/4$	$3\pi/4$	$I_6 = I_m + \frac{I_a}{2}(1-\cos 2\theta\sin\delta)$

The simultaneous equations are solved for θ and δ as:

$$\theta = \frac{1}{2}a\tan(I_5 - I_3, I_4 - I_6) \tag{3.3}$$

$$\delta = a\tan\left[(I_5 - I_3)\sin 2\theta + (I_4 - I_6)\cos 2\theta,\ I_1 - I_2\right] \tag{3.4}$$

Which give θ in the range of $-\pi/4$ to $\pi/4$ and α in the range of $-\pi/2$ to $\pi/2$. The isoclinic angle is also the principle stress orientation. In order to represent all the random stress states, the range of θ given by 3.3 is not sufficient and at lease a θ in the range of $-\pi/2$ to $\pi/2$ is needed. This is a system ambiguity and will be discussed in chapter 7.

Double refraction is an inhere property of stressed material and not limited to silicon wafers. The only requirement is that proper wavelength of light need to be chosen for the material so that the material is transparent. Then phase stepping method can be used to

calculate the two photoelastic parameters. And by applying stress optic law, maximum shear stress can be calculated.

3.7 Conclusions

The principle of photoelasticity was introduced and the setup of circular polariscope was described. Six phase stepping method was used to extract the photoelasticity parameters in this thesis.

Chapter 4

Research Plan

4.1 Objective

The objective of this research is to expand the effort of the non-destructive method using polariscope to obtain in-plane residual stress for thin, flat silicon wafers. A new system setup of polariscope was introduced and calibrated to obtain stresses of the entire field in large commercially used silicon wafers as large as 156×156mm. Then full stress components were extracted from the experimental data by using the shear difference method.

4.2 Approach of the Research

In this research, a full-field near infrared (NIR) polariscope was built and calibrated. The prior system was not suitable for in situ measurement since it can only measure a small potion of the wafer. Also only the maximum shear stress can be measured using the polariscope.

In the PV industry, 80% of the wafers are multi-crystalline. For multi crystalline wafers, different grains affect light transmission differently due to different atom densities along the light transmission direction for each orientation. In order to measure multi crystalline wafers correctly and accurately, this research extends the stress optic law by adding the new factor of grain orientation, which makes the theory more comprehensive and complete. For both single and multi crystalline wafers, grain

orientation information needs to be input to the program. It is very time consuming to using x-ray diffraction (XRD) to determine grain orientations for multi crystalline wafers. This research points out that light transmission is a function of the grain orientation and can be used for determining the grain orientations. In this way, the polariscope system can identify grain orientations automatically.

Another trend in the photovoltaic industry is that wafers become larger and larger. Now 156×156mm wafers are widely used. All the existing polariscopes can only measure a small potion of the wafers from 25mm to 75mm. It takes ten to twenty measurements for 156mm wafers using the existing system. A new setup to measure the whole field of the wafers in one measurement was built. The new system enabled the in situ measurement of large wafers.

Due to the inherent system ambiguity, polariscope can only measure the maximum shear stress. However knowledge of the maximum shear stress is not sufficient to determine crack growth and wafer breakage. The biggest contribution of this research is a description of a method to obtain full stress state using the shear difference method (SDM). The system ambiguity is resolved mathematically by introducing a new function which extends the range of the isoclinic angle to $-\pi/2$ to $\pi/2$ and it can be proved that under the current setup, the full stress state can be calculated using SDM. Another critical part for SDM is how to properly capture the boundary conditions. By using the new setup built in this thesis, the whole boundaries can be easily captured. The methodology was verified by successfully obtaining the full stress state for a four point bending beam.

The flow chart of the research on the polariscope is shown in Figure 4.1. The boxes in yellow are the researches conducted in this thesis. The objective is to measure the full

stress components in crystalline silicon. To ensure the reliability of the polariscope, an error analysis was conducted. The system was calibrated for both the principle stress orientation and crystal orientation so as to expand the method to multiple crystalline silicon wafers. Then a new setup of polariscope was used to capture the edges of the wafers. By applying boundary conditions and equilibrium equations, the full stress components were eventually obtained.

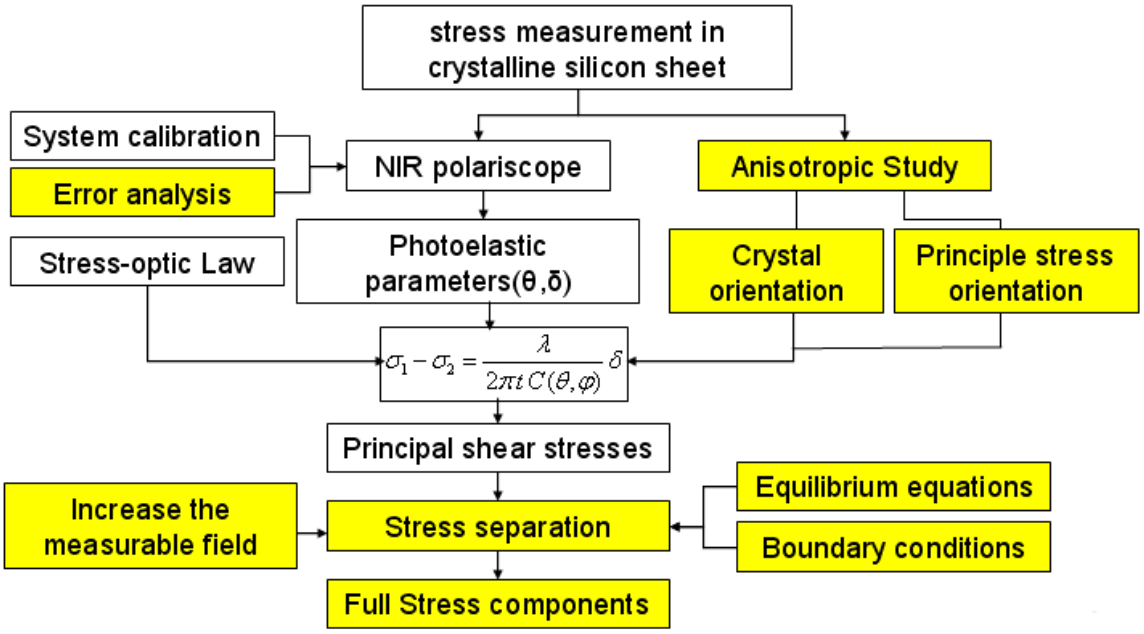

Figure 4.1 Flow chart of research conducted in this thesis.

Chapter 5

Grain Characterization and Determination of Anisotropic Stress Optic Coefficients

5.1 Summary

This chapter summarizes the calibration of the stress optic coefficients for different stresses and crystal orientations. Shijiang He [37] pointed out that the stress optic coefficient of EFG wafers could be 1.7 times of the CZ wafers, which shows that the effect of crystal orientation on the stress optic coefficients can't be neglected.

5.2 Expansion of Stress Optics Law

The isotropic stress optic law was shown as equation 3.1, which for an isotopic material the maximum shear stress is proportional to the phase retardation of light. Shijiang He et. al. [40] proved that the stress orientation also influenced the phase change of the light. He extended the stress optic law by replacing a constant stress optic coefficient with a stress orientation dependent stress optic coefficient as shown in equation 5.1, where θ is the principle stress orientation.

$$\sigma_1 - \sigma_2 = \frac{\lambda}{2\pi t C(\theta)}\delta \tag{5.1}$$

Recent research shows that the stress optic coefficients are not only a function of the principle stress orientation but also a function of grain orientations. The reason is that different grain orientations have different atom alignments and atom densities. For example, the ratio of atom density for silicon between (111) and (100) is 2: 1. Thus light speed is different when it passes through different orientations.

The most general case of the stress optic law is shown in equation 5.2. In equation 5.2, the stress optic coefficients are functions of both the crystal orientation φ and the principle stress orientation θ.

$$\sigma_1 - \sigma_2 = \frac{\lambda}{2\pi t C(\theta, \varphi)}\delta \tag{5.2}$$

The stress optic law is used to calculate the maximum shear stresses if the stress optic coefficient is known. In Equation 4.2, C is the stress optic coefficient which is a function of θ (the principle stress orientation) and φ (the crystal grain orientation), t is the thickness of the sample, λ is the wavelength of the light source, and σ1, σ2 are the maximum and minimum principal stresses and δ is the phase retardation .

5.3 Calibration of Stress Optic Coefficients

Stress optic coefficients need to be calibrated before the polariscope can be used to measure the residual stresses in silicon wafers. The process to obtain the stress optic coefficients is the reverse procedure to that of stress measurement. To calibrate the stress optic coefficient for an orientation, a known stress field needs to be applied. The applied stress needs to be large enough so that the residual stress, if there is any, can be ignored.

A good deal of work has already been done in this area. Stress optic coefficients for (001) and (111) orientations are derived and calibrated by Shijiang He and S. Danyluk.[40]. The cast silicon was taken to have the isotropic coefficient of the (111) orientation of silicon [37].

5.3.1 Determine Crystallography Using Back Laue System

V. Garcia [17] used a back Laue procedure to determine the crystal orientation in cast wafers. Since silicon has a well known crystal structure, the Laue system could be used to check the orientation of the grains with respect to the surface by analyzing the x-ray diffraction pattern. A pattern reflected by a certain orientation can be pre-determined by knowing the crystal structure (diamond cubic for silicon) and invoking Bragg's law as shown in figure 5.1

.

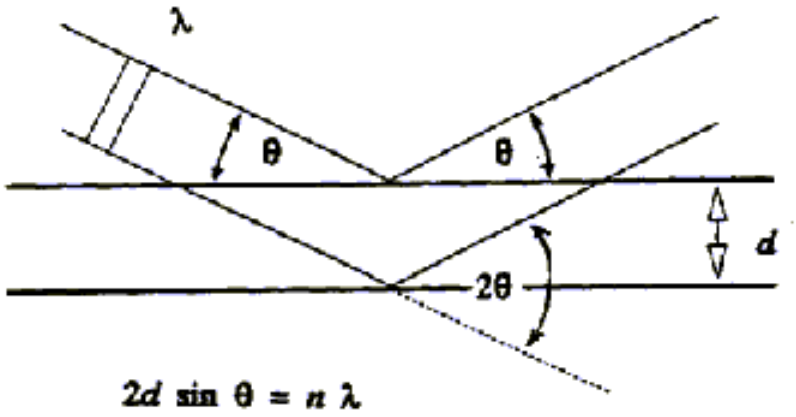

Figure 5.1 Principle of the Bragg's Law.

Figure 5.2 is an optical image of a silicon beam cut from a 156×156 mm cast silicon wafer. Table 5.1 lists the grain orientations (corresponding to the φ value in equation 5.1) and the rotations (which is the pole angle of the grain corresponding to the θ value in equation 5.1) of a multi crystal wafer beam. A graph summarizing the frequency of the grain orientations for a group of cast wafers is shown in Figure 5.3. As can be seen, the majority of the orientations are (100), (011), (111), (211) and (321). Figure 5.3 also demonstrates that there is a great deal of variations of the wafer grain orientations, thus it is necessary to calibrate the stress optic coefficients for each grain orientation.

Table 5.1 Grain characterization of a multi crystalline silicon beam.

Grains	3	6	8	9	10	14	16	17	24
Orientations(φ)	344	211	100	211	321	432	321	211	321
Rotations(θ)	-23	-69	60	-71	-100	-42	60	31	131

Figure 5.2 Optical image of the multi crystalline wafer beam.

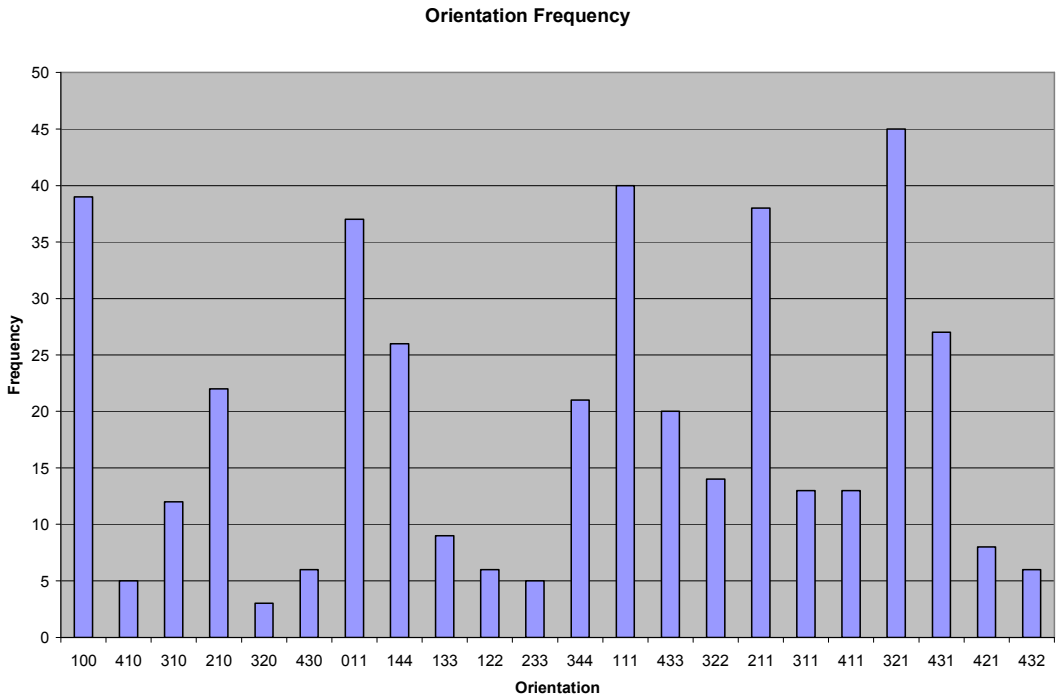

Figure 5.3 Orientation Frequency versus grain orientations.

5.3.2 Obtaining Stress Optic Coefficients by Four Point Bending Experiment

Four-point bending, shown in Figure 5.4, was used to apply known stresses in order to calibrate the anisotropic stress optic coefficients. Silicon beams with dimensions 150 × 10 × 0.2 mm, were removed by dicing from 156×156 mm cast wafers. The load was applied by adding weight and the residual stresses in the beams were assumed small compared to the applied stresses.

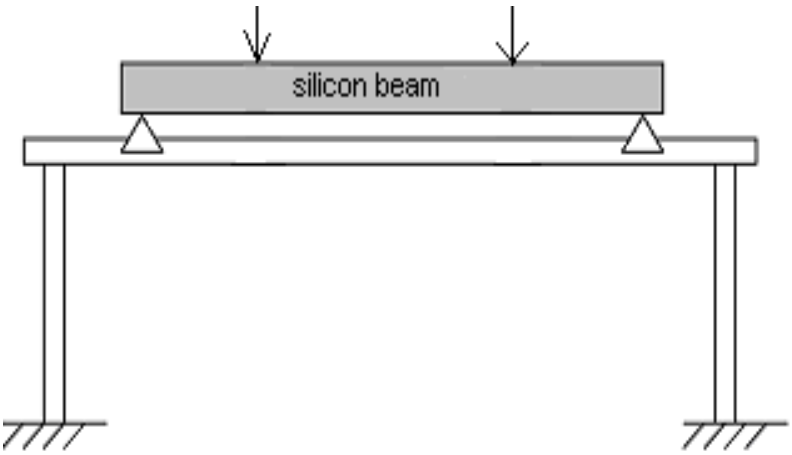

Figure 5.4 Schematic diagram of the four point bending setup.

Figure 5.5 shows the schematic of a multi crystalline wafer loaded by four-point bending, sitting in the polariscope system. Compressive strain is at the half portion above the neutral axis and tensile strain is at the half portion below the neutral axis. I_a is the light source intensity. I_i is the light intensity captured by the camera and i is from 1 to 6 which representing light intensity of the six images captured from six phase stepping method.

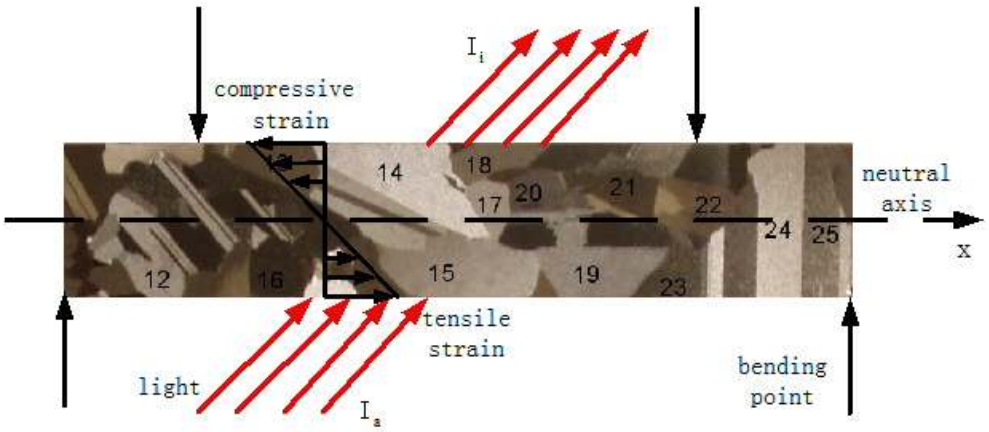

Figure 5.5 Schematic diagram of a multi crystalline bending wafer beam in the polariscope.

Phase retardation and the isoclinic angle are calculated using equation 3.3 and 3.4 respectively. Figure 5.6 shows a typical result of the retardation δ and isoclinic angle of a multi crystalline cast wafer. The physical size of the measured area is about 200 × 50 pixels, or 40 × 10mm. The retardation is nearly uniform along the longitudinal direction and linear along the transverse direction. The non-uniformity phase retardation along the horizontal direction is due to the anisotropic light transmission among the grain orientations.

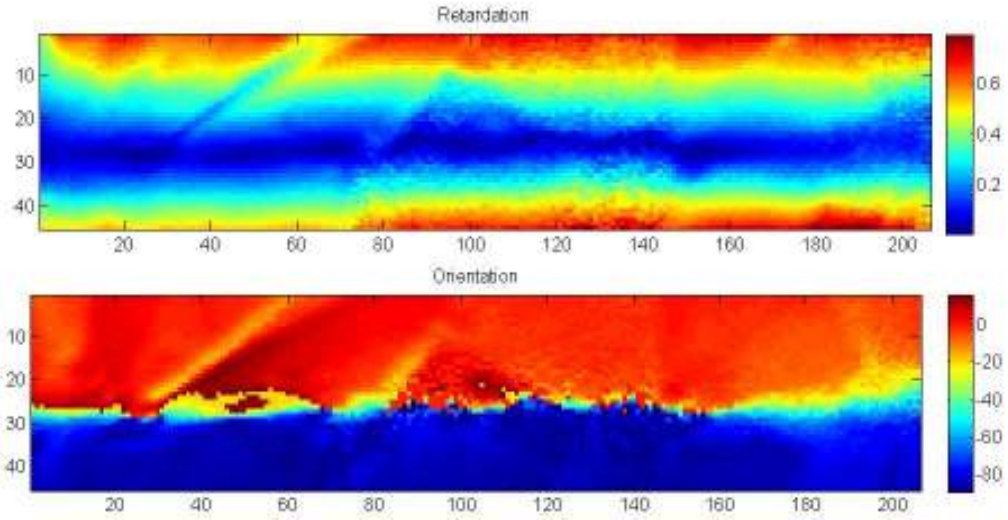

Figure 5.6 Phase retardation and isoclinic angle of a bending cast wafer beam.

In order to calibrate a grain of interest, only a potion of the pure bending beam needs to be studied. Figure 5.7 shows the phase retardation and isoclinic angle of grain 14 in figure 5.2. Within a single grain, the phase retardation is uniform, which suggest that the stress optic coefficients are constant throughout the grain.

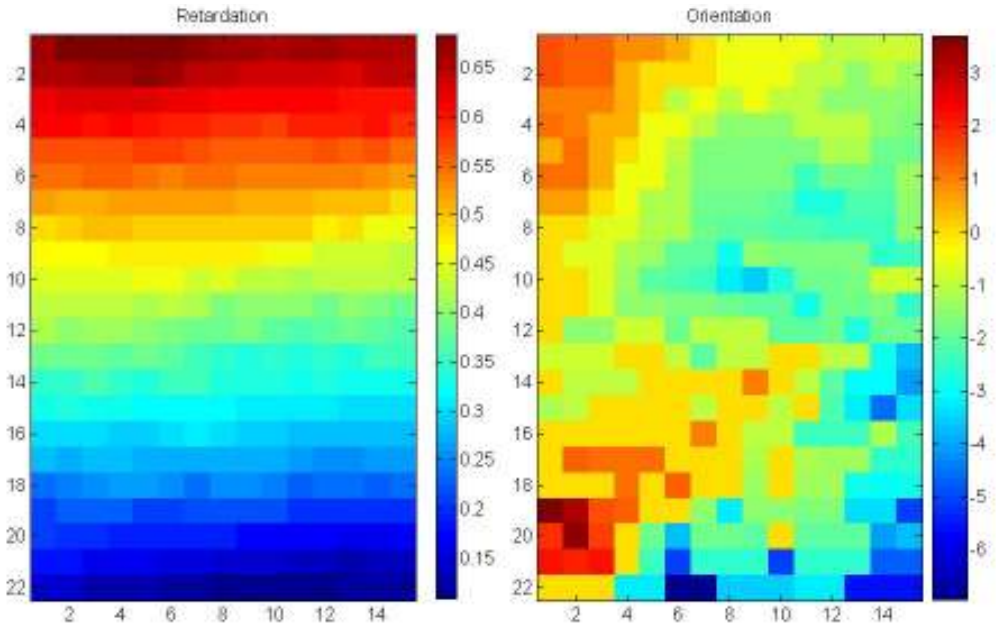

Figure 5.7 Phase retardation and isoclinic angle of grain 14.

Usually the maximum stress is used for purposes of characterization. However, the maximum stress cannot be determined with enough accuracy because the edges of the beam are not clearly defined in the images, and a variation of one pixel, or 0.2 mm, can introduce an error of 5%. The stress optic coefficient is related to the slope of the retardation, $d\delta / dy$, which can be determined with high accuracy using a linear least-square fit method. Figure 5.8 is the least-square fit of the retardation to the vertical location relative to the neutral axis. The double refraction, which is related to δ, is plotted versus the vertical location (relative to the center of the beam). The correlation coefficient of the linear fit is 0.98. The principal stresses for pure bending are,

$$\sigma_1 = \frac{M}{I} y \,, \quad \sigma_2 = 0 \tag{5.3}$$

where $I = h^3 t / 12$ is the moment of inertia of the cross section, M is the applied moment, and y is the vertical location from the center. By substituting Equation 5.3 into Equation 5.2, the

stress optic coefficients can be obtained in terms of the slope of the retardation as shown in equation 5.4,

$$C = \frac{d\,\delta}{dy} \Big/ \left(\frac{2\,\pi\,t}{\lambda} \frac{M}{I} \right) \tag{5.4}$$

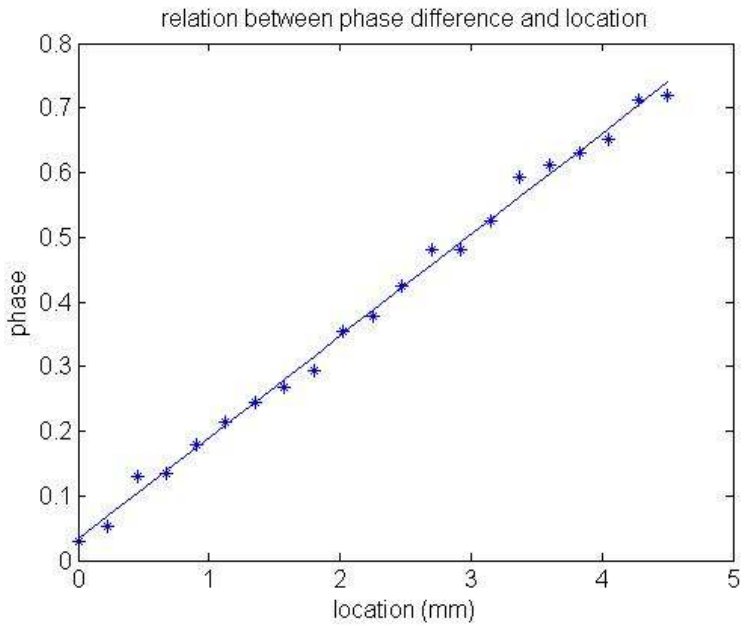

Figure 5.8 Least squares fit of retardation of grain 14.

Table 5.2 shows the stress optic coefficients for grains of cast wafers. About 80 different grains orientations and pole angles were measured in the experiments. For those grains orientations which are not covered, a linear fit could be used to determine the stress optic coefficient. The variation of the maximum stress optic coefficients to the minimum is about 1.7.

Table 5.2 Stress optic coefficients of grains with a certain pole angle.

Orientations (φ)	100	111	111	111	210	211	321	322	421
Rotations (θ)	20	53	-5	65	-8	31	-100	106	73
Stress optic coefficient($10\text{-}11\times Pa^{-1}$)	2.40	2.54	2.53	2.55	2.08	2.75	1.87	2.35	1.75

5.4 Characterization of Grain Orientations

In order to apply the calibrated stress optic coefficients to measure stresses for different grains, crystal orientations for each grain have to be determined first. The most general technique to determine grain orientation is x-ray diffraction which was discussed in chapter 3. X-ray diffraction is a point method and usually takes several hours to measure a 156×156 mm cast wafer, which is not acceptable for in situ measurement for the photovoltaic industry. Shijiang He [37] used an average stress optic coefficient for multi crystalline silicon wafers to enable in situ measurement. However due to big variation of stress optic coefficients, the accuracy of the measurement is decreased about 35%.

In this research, it was found that the transmitted light intensity is correlated to the orientation determined by x-ray diffraction, which is usually called optically anisotropic. When light pass through stress free single crystal silicon, no anisotropic can be observed. The light transmission image captured by the infrared camera is uniform as shown in figure 5.9 (a), which is a (100) single crystal silicon wafer. The uniformity of the image shows that at stress free state, single crystal silicon is optically isotropic. Figure 5.9 (b) is light transmission image of a (111) single crystal wafer under the same light power.

Figure 5.9 indicates that (111) orientation has much higher light transmission rate than (100) orientations. Thus, for multi crystalline silicon wafers which contain all kinds of grain orientations, they are optically anisotropic. A typical infrared transmission intensity image of a multi crystalline silicon wafer is shown in figure 5.10. It can be seen that some grains are much brighter than the others. This correlation was validated by comparing infrared transmission to grain orientations from several wafers. Samples were prepared by dicing wafers into 125 × 10 mm beams and optical image of one beam is shown as figure 5.11. Each grain is labeled by a number for later reference. X-ray diffraction was used to determine orientations of each grain and light transmission images were taken by the infrared camera using the polariscope system.

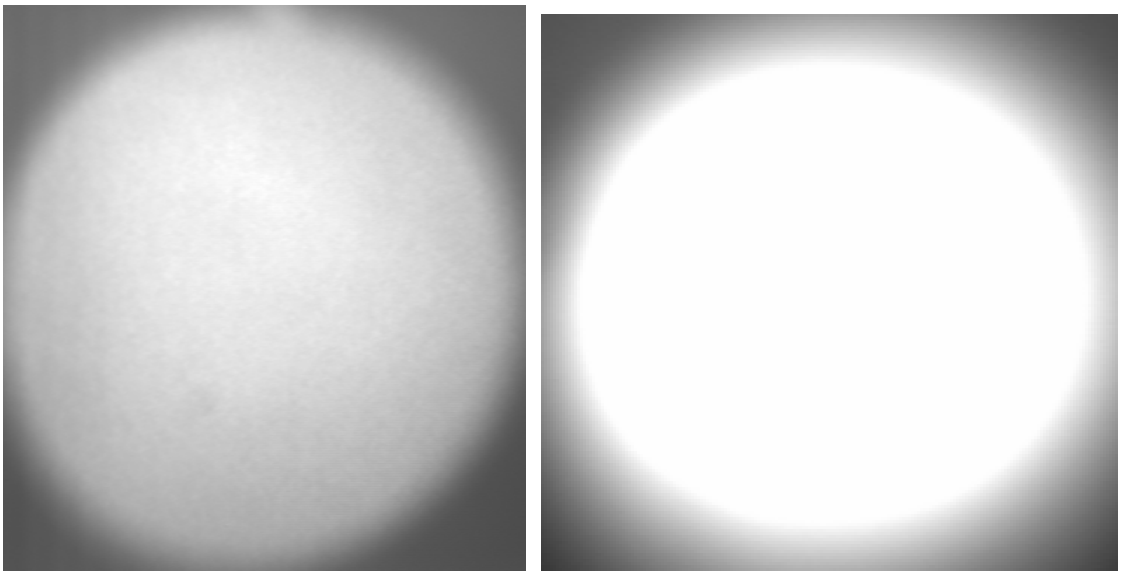

(a) Transmission image of (100) wafer. (b) Transmission image of (100) wafer.

Figure 5.9 Comparison of light transmission between (100) and (111) wafers.

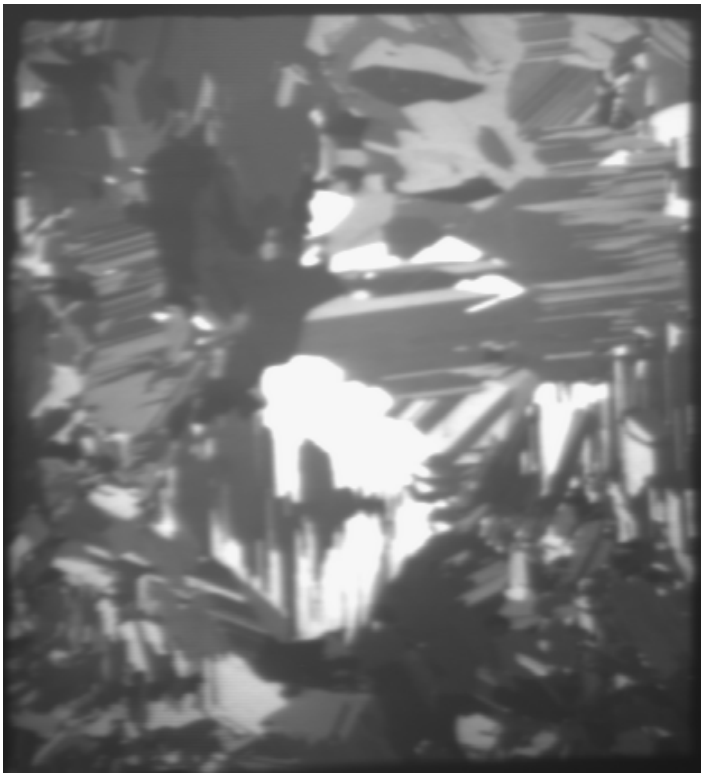

Figure 5.10 IR light intensity image captured by the CCD camera.

Figure 5.11 A photograph of a silicon beam with labeled grains prepared for x-ray diffraction.

Figure 5.12 IR light transmission image of the beam shown in figure 5.10.

It can be readily verified that the intensity of figure 5.11 and figure 5.12 is inversely correlated. If a grain in the optic image is bright, then it appears dark in the light transmission image. Table 5.3 summarizes the light intensity of some grains both from the optical image and the transmission image, which verified that optical image and transmission image are inversely correlated.

Table 5.3 Gray levels of different grains in both optical image and transmission images.

Grain ID	optical image	transmission image
A4-10	bright	dark
A4-14	bright	dark
A4-16	bright	dark
A4-17	medium	medium
A4-26	bright	dark
A4-3	dark	bright
A4-6	dark	bright
A4-8	bright	dark
A4-9	dark	bright
A5-1	bright	dark
A5-11	bright	dark
A5-12	dark	bright
A5-15	medium	medium
A5-22	bright	dark
A5-4	bright	dark
A5-5	medium	medium
A7-5	dark	bright
A7-7	bright	dark
A7-8	middle	median

Grain orientations as identified by the miller indices are correlated to the image intensity as shown in Table 5.4. From Table 5.4, it can be seen that some orientations transmit infrared light better than other orientations. Among the three major directions (111) (110) and (100), (111) directions have the brightest light transmission.

Table 5.4 Orientations and gray levels of transmission image for different grains.

Orientation	Grain ID	Rotation	Transmission image
100	I7-3	5	dark
100	I5-18	20	dark
100	A2-12	30	dark
100	G6-5	32	dark
100	G9-3	32	dark
100	G9-5	32	dark
100	G5-1	35	dark
100	G5-5	45	dark
100	G5-6	46	dark
100	A4-8	60	dark
100	I3-22	60	dark
111	I2-8	-5	bright
111	I3-15	3	bright
111	A8-12	4	bright
111	I3-6	4	bright
111	I6-10	5	bright
111	G9-20	20	bright
111	A7-5	25	bright
111	A5-15	28	bright
111	A5-21	28	bright

Table 5.4 (continued)

111	A8-2	29	bright
111	A5-12	30	bright
111	A8-3	30	bright
111	A8-4	30	bright
111	A8-5	30	bright
111	G9-15	30	bright
111	I2-7	53	bright
111	I5-17	65	bright
210	A5-4	-120	median
210	A5-17	-65	median
210	G7-2	-47	median
210	G7-5	-30	median
210	I3-9	-8	median
210	A8-19	98	median
210	A2-17	125	median
210	A2-14	150	median
110	B4-8	60	median
110	B4-18	85	median
110	AB-55	40	median
100	AB-58	38	median
211	A8-18	-89	median
211	A4-9	-71	median
211	A4-6	-69	median
211	I3-14	-20	median
211	I3-17	-14	median
211	G2-15	1	median

Based on Table 5.4, the grain orientations could be estimated. For a light transmission image of a multi crystalline wafer such as figure 5.9 which is a 8 bit image and has 256 gray levels, all the pixels that have gray value bigger than 200 are characterized as (111), the ones that have a gray value between 100 to 200 is the (110) and the others which have a gray value of below 100 is the (100). In this way, the measurement accuracy is only 10% less than using all the individual grain orientation information. Because of the limited numbers of grains measured by x-ray diffraction, the characterizations of other grain orientations such as (432) could not be obtained. In addition, the infrared camera doesn't have sufficient resolution to distinguish the difference between orientations such as (111) and (655).

The reason why light transmission varies with orientation can be explained by considering the crystal structure of silicon. Different orientations have varying atom densities and bond strengths. The atom density ratio between (111) (110) and (100) is 6:4:3 as shown in figure 5.13. For the (111) orientations, since the in-plane atom density is higher, there are less obstacle on the light path, which results in higher transmission rate for the (111) orientations.

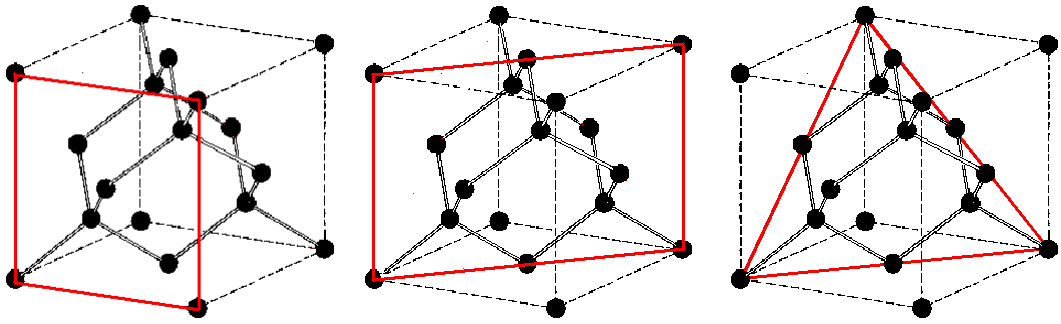

(a) (b) (c)

Figure 5.13 Crystal structure of silicon for orientations (a): (100) (b): (110) (c): (111).

5.5 Conclusions

Grain orientations and pole angles were measured by x-ray diffraction method. Anisotropic stress optic coefficients are then calibrated for each grain using four point bending experiments. In order to apply the anisotropic stress optic coefficients during in situ stress measurement, grain characterization were characterized based on the light transmission intensity. Among (100), (110), (111) orientations, (111) orientation is found to have the highest light transmission and (100) orientation has the lowest light transmission.

Chapter 6

New System Setup

6.1 Summary

A new configuration of an infrared polariscope is presented. The new setup is then used to measure the entire field of the wafer as large as 156×156 mm. Location dependant stress optic coefficients of the new polariscope system were obtained using the four point bending experiments. Edges of the wafers can be detected clearly using the new system.

6.2 System Description

As described in chapter 2, the typical circular polariscope system shown in figure 2.1 is restricted by the size of the quarter waveplates and the polarizers, which is generally 25 to 75 mm. It takes ten to twenty measurements to measure a 156×156 mm wafer. After the piecewise measurement, all the measurements need to be superimposed, which is time consuming and causes inaccuracies.

A new setup of the polariscope is shown in figure 6.1. In the new system, the polarizers and quarter waveplates are moved outside of the lenses and so the illumination field is restricted by the lenses. Two 240 mm lenses are used in our system so that samples as big as 240 mm can be measured in one measurement. The new system setup enables in situ measurement of large wafers and the detection of the wafer edges.

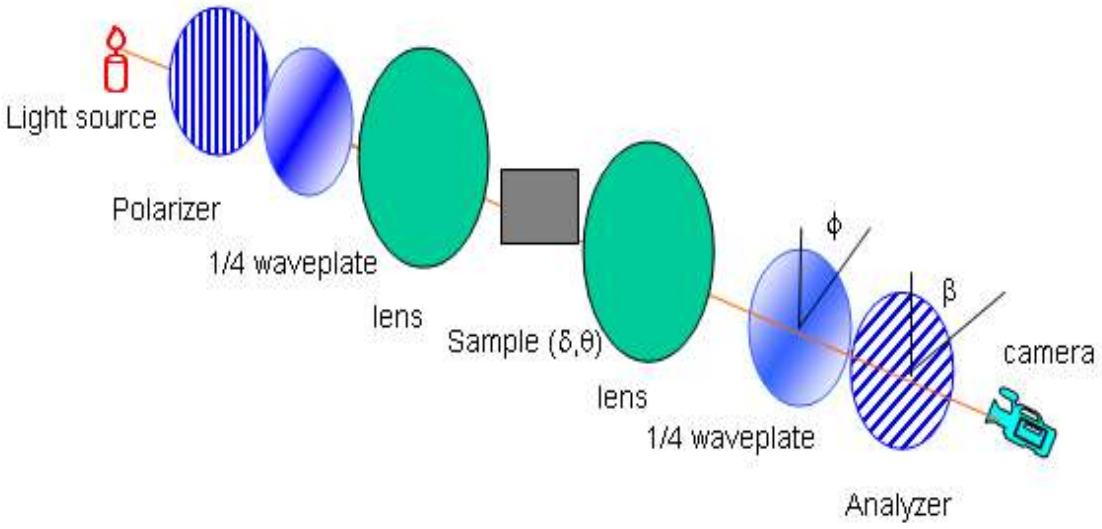

Figure 6.1 New polariscope system for measuring large wafers.

6.3 System Calibration

Large field measurements are not without penalty. Due to the inclined light incident to the waveplates and the un-collimated light induced on the sample, there is an inaccuracy of the phase change of the light by the waveplates and sample. The problem was solved by calibration of the entire illuminating field. The calibration procedure has already been described in chapter 5. Since the system shown is center symmetric, the calibration can be simplified to a calibration of a radial line from the center to the edge. Figure 6.2 indicates the position of a beam in the system. After calibration of a radius of the field, the results can be extended to the whole illumination field.

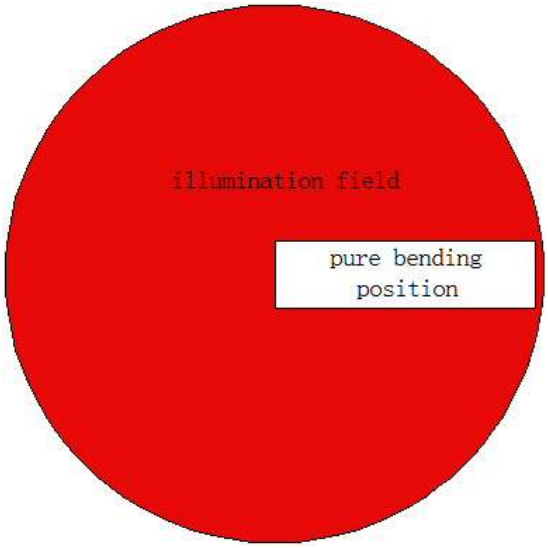

Figure 6.2 Position of the beam in the new polariscope system.

In order to reduce the complexity, a CZ single crystal wafer was used to calibrate the system. The residual stresses in the CZ wafers were assumed to be negligible compared to the applied stresses and rectangular beams were cut from these wafers. Figure 6.3 is the phase retardation map of the CZ silicon beam. The very left point of the image is the center of the illuminated field.

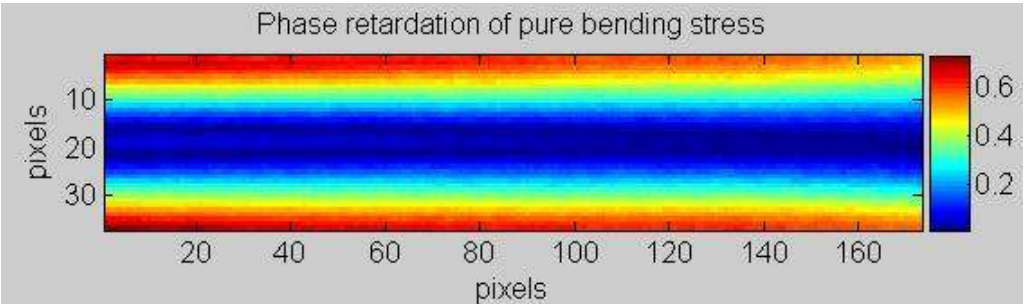

Figure 6.3 Phase map of a four point bending beam cut from a CZ wafer.

Figure 6.3 shows that the phase map of the beam varied monotonically from center to edge, which indicates stress optic coefficients, are different at each point of the radius. Stress optic coefficients were calculated for each cross section of the phase map using the same procedure described in chapter 5. The results are shown in figure 6.4. The variation of the stress optic coefficients from center to edge is about 35%.

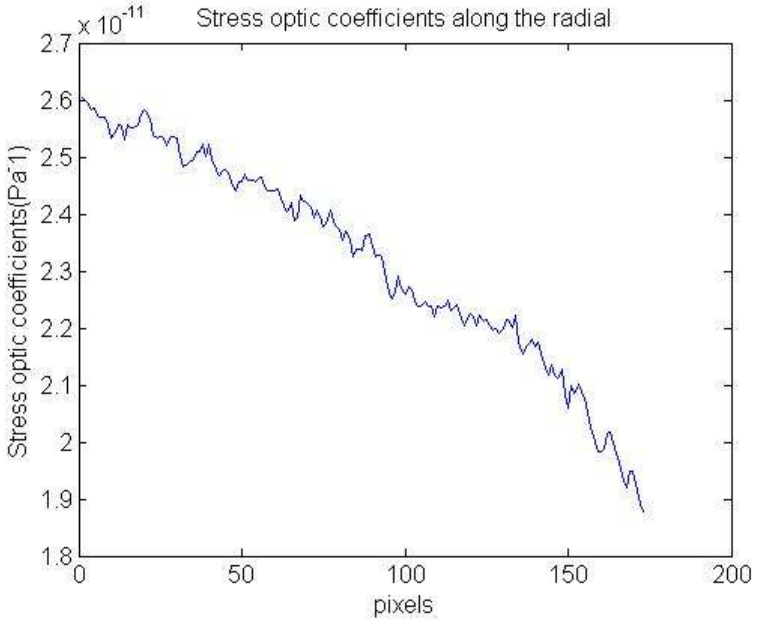

Figure 6.4 Stress optic coefficients along the radius.

The stress optic coefficients are only a function of radial location, x, since the system is centre-symmetric. A curve fitting using equation 6.1 is shown in figure 6.5. The fitting result is shown as equation 6.2. The R-square value is 0.97.

$$C = a \times \cos\left(\frac{x}{r}\right) + b \tag{6.1}$$

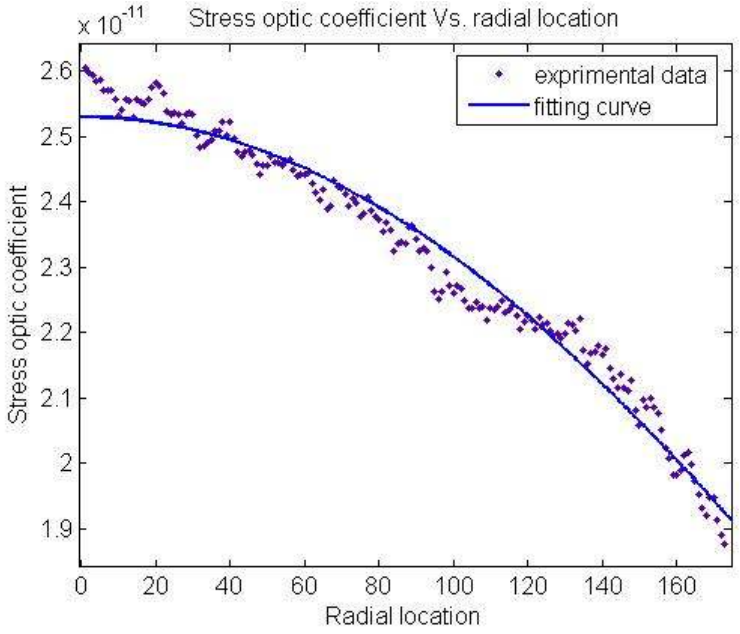

Figure 6.5 Data fitting of the stress optic coefficients for the new polariscope system.

$$C = 1.32\times10^{-11}\cos\left(\frac{x}{r}\right)+1.21\times10^{-11} \tag{6.2}$$

In equation 6.2, C is the stress optic coefficient, x is the radial location and r is the radius of the illuminating field. The results are close to the results measured by S. He, which is from 1.4 to 2.1×10^{-11} [37].

Combining equation 6.2 and the stress optic law shown in equation 4.1, a modified stress optic law for the new system setup is given in equation 6.3. Applying equation 6.3, the maximum shear stress τ_{max} of the whole field is calculated from only one measurement for a 156×156 mm wafer.

$$2\tau_{max} = \sigma_1 - \sigma_2 = \frac{1.32\times10^{-11}\lambda}{2\pi t C(\theta,\varphi)\times\left(\cos\left(\frac{x}{r}\right)+0.92\right)}\delta \tag{6.3}$$

6.4 Explanation of Location Dependent Stress Optic Coefficients

The radial dependant stress optic coefficients are due to the inclined incident light to the waveplates and silicon wafer as shown in figure 6.6 (the dash lines are the line paths for the typical polariscope system as shown in figure 3.8). Since light is inclined to the waveplates, double refraction occurs. The path of light through the waveplates is longer than in the case where light is perpendicular to the waveplates. The relation between the path traveled by the inclined light and normal incident light to the waveplates is shown in equation 6.4. The quarter waveplates are no longer quarter waveplates since it results in phase change bigger than $\pi/2$. The incline light to the sample can also result in additional phase changes of the silicon wafer.

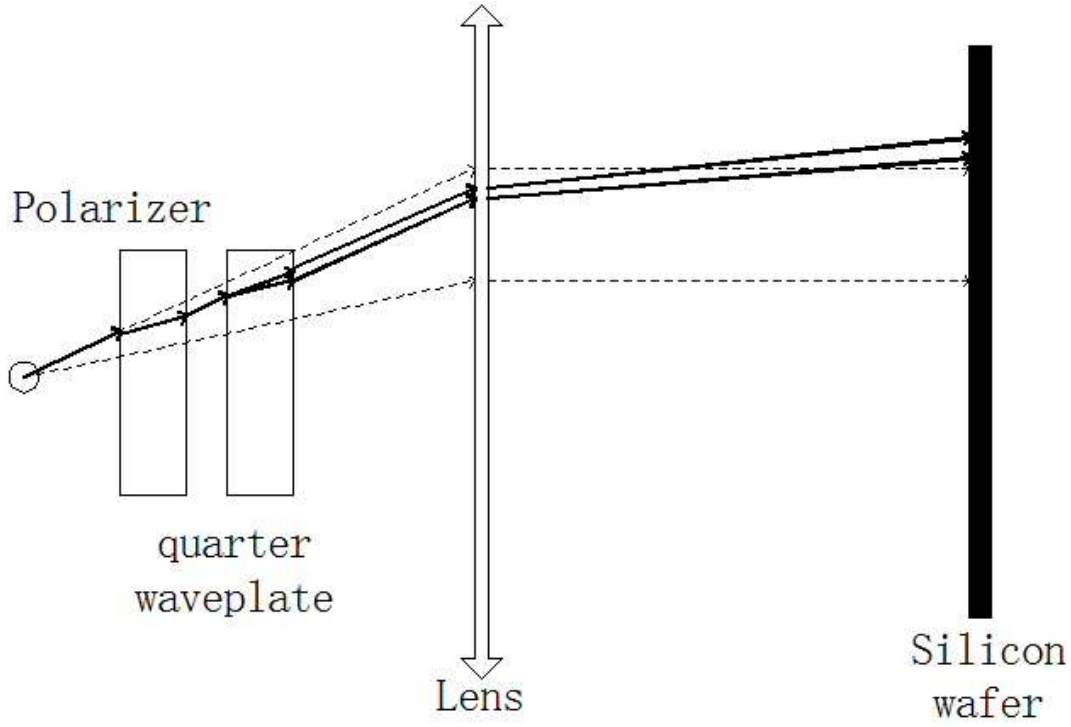

Figure 6.6 Light paths through the new polariscope system.

$$L2 = \frac{L1}{\cos(\theta)} \tag{6.4}$$

6.5 Experimental Results of the New System

Full field stress map is obtained using the radial dependant stress optic coefficients. Figure 6.7 (a) is the full field maximum shear stress of a 100 mm EFG wafer and Figure 6.7 (b) is the light intensity image captured by the infrared CCD camera. The edges of the wafer are indicated as transmissions to a dark portion of the image. Figure 6.8 (a) is the full field maximum shear stress of a 156×156 mm wafer and Figure 6.8 (b) is the corresponding light intensity image. The stresses are calculated using radial location dependant stress optic coefficient shown in equation 6.3.

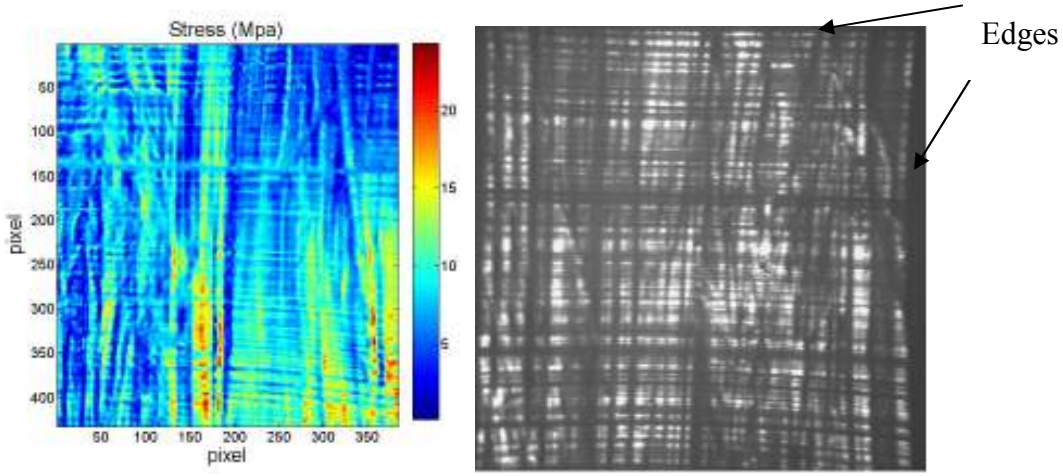

(a) Stress map. (b) Light transmission image.

Figure 6.7 Stress map and light transmission image of a 100×100 mm EFG wafer.

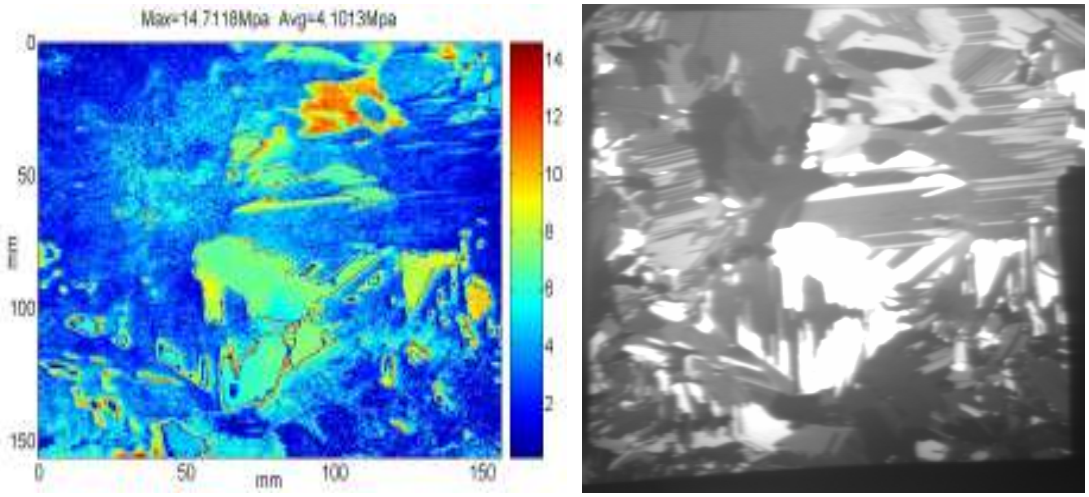

(a) Stress map. (b) Light transmission image.

Figure 6.8 Stress map and light transmission image of a 156×156 mm cast wafer.

To verify the result of the new system, the same location of an EFG wafer was measured both by the typical polariscope and the new polariscope. Figure 6.9 is the stress result measured by the typical polariscope and figure 6.10 is the stress result measured by the new polariscope. The difference is within 10% which verified the new polariscope is accurate to measure stresses in the wafers by using the location dependant stress optic coefficients given by equation 6.3.

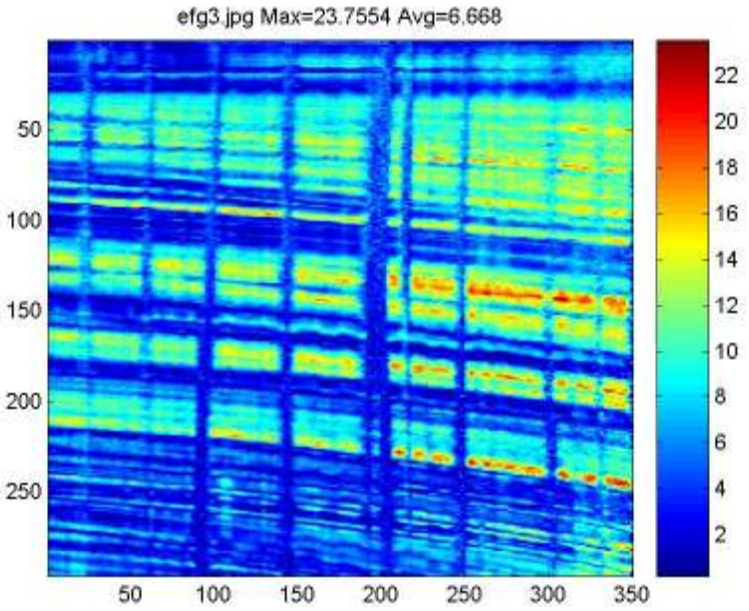

Figure 6.9 Stress measured by the typical polariscope.

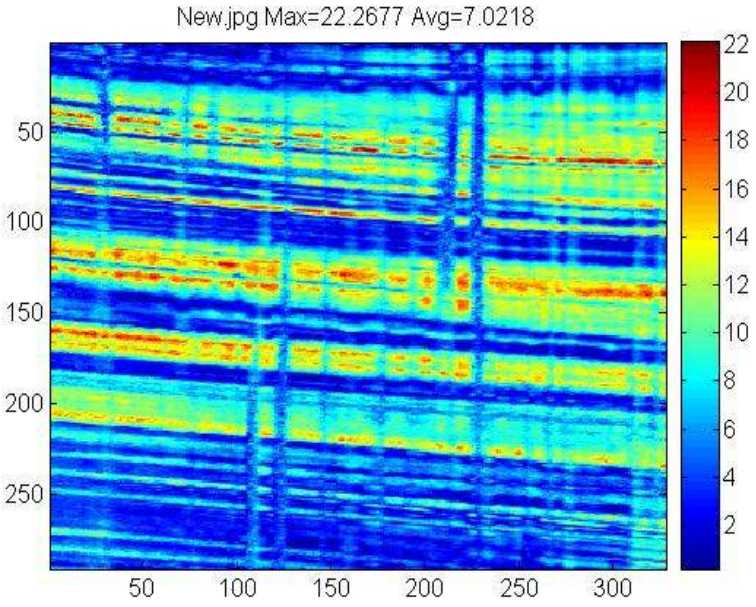

Figure 6.10 Stress measured by the new polariscope.

6.6 Conclusions

A new setup of the polariscope was built and stress optic coefficients were found to be location dependent. The system can accurately measure the whole field stresses for wafers as large as 156×156 mm.

Chapter 7

Stress Separation

7.1 Introduction

As mentioned earlier, the polariscope can measure the maximum shear stress in the thin silicon sheet, but the extraction of principle stresses， generally referred to as stress separation, is still a major issue in the measurement. The major difficulty for stress separation is that there are ambiguities to determine both the isoclinic and isochromatic parameters in the phase shifting photoelasticity. Another difficulty is that the most common used traditional stress separation techniques such as the Lame–Maxwell (LM) method [56] and the shear difference method need the stress information at the boundaries of the sample. To properly capture the whole wafer boundaries is very critical to obtain the full stress components. In this thesis, shear difference method is used to automatically obtain the three stress components σ_x , σ_y and τ_{xy} . Comparing to the other stress separation methods, this method can be used to extract full stress components not only for applied stresses field but also for residual stresses.

A good deal of work has already been done on stress separation. Researchers have been focusing on how to solve the system ambiguity when determining the maximum shear stress and principle stress orientation. T. Liu et al. [57] used a two step loading method to solve the system ambiguity. With this method, the system ambiguity can be resolved when the two sequential loads are in the same direction, which is not applicable

to a measure of the residual stress. G. Petrucci and G. Restivo tried to separate stresses along stress trajectories by adjusting stress orientation empirically[58]. M. Ramji and K. Ramesh [59] used a ten step-phasing method and the technique uses domain masking to solve the ambiguity. In domain masking, a seed of high quality needs to be found in the phase map, which is not applicable in the case of residual stresses. This thesis is focusing on obtaining the full stress components of the residual stresses by resolving the system ambiguity and applying shear difference method.

7.2 Resolve System Ambiguity

Figure 7.1 illustrates the concept of the system ambiguity. Four stress states are shown in figure 7.1 and described by equation 7.1. The maximum shear stress of the four stress states is equal and the stress in the x direction is bigger than the stress in the y direction. The polariscope can't distinguish between those four stress states since all of them have the same phase retardation and principle stress orientation. It is important to distinguish the tensile stress (case 1, 2) from the compressive stress (case 3, 4) since the tensile stress will initiate crack growth. Stress separation is the procedure to distinguish the system ambiguity and extract the normal stresses from the maximum shear stress that the polariscope measured.

$$2\tau_{\max} = \left|\sigma_{11} - \sigma_{12}\right| = \left|\sigma_{21} - \sigma_{22}\right| = \left|\sigma_{31} - \sigma_{32}\right| = \left|\sigma_{41} - \sigma_{42}\right| \qquad (7.1)$$

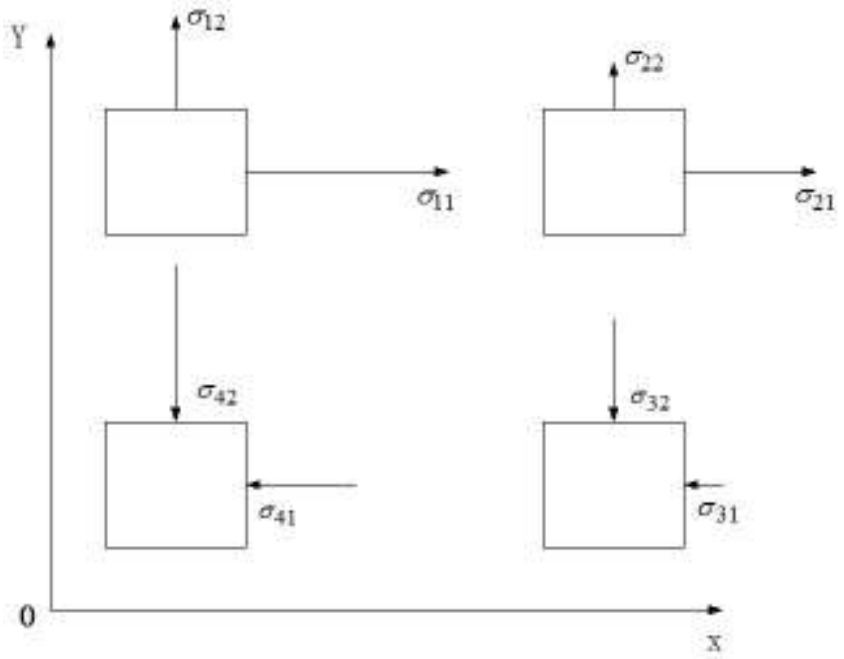

Figure 7.1 Demonstration of the system ambiguity away from the edges.

Figure 6.2 shows that there are only two stress states at the boundaries, either tensile or compressive along the tangential direction. The traction stresses including shear stress and normal stress in the y direction are zero.

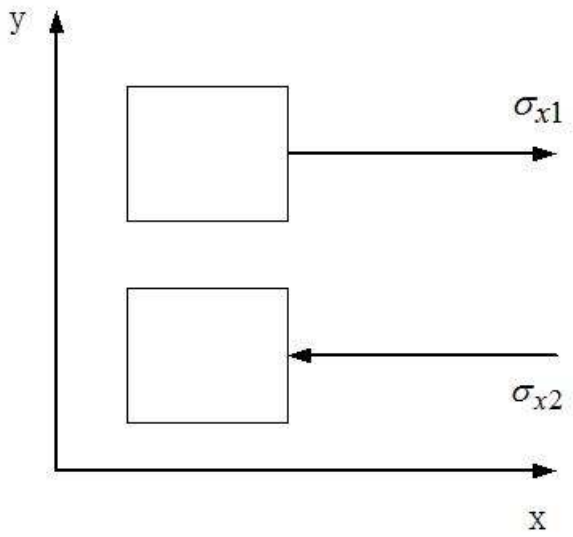

Figure 7.2 Illustration of the two stress states at the boundary.

As described in chapter 3, six phase stepping method was used in this thesis to obtain the two photoelastic parameters, namely the phase retardation and the isoclinic angle. For both of these two parameters, the inverse trigonometric functions need to be solved as shown in equation 3.3 and 3.4, and the solution of equation 3.3 will only have a period of π/2, which is not sufficient to represent all the stress states. In order to fully interpret all the directions of the random residual stresses, a new function arctan2 was used to extend the period of stress orientation from π/2 to π.

Arctan2 is a Matlab function which has a period of 2π. In terms of the standard arctan function, which is with a range of (−π/2, π/2), arctan2 can be expressed as equation 7.2 and figure 7.3 is a three dimension plot of function arctan2.

$$\operatorname{atan2}(y,x) = \begin{cases} \arctan(\frac{y}{x}) & x > 0 \\ \pi + \arctan(\frac{y}{x}) & y \geq 0, x < 0 \\ -\pi + \arctan(\frac{y}{x}) & y < 0, x < 0 \\ \frac{\pi}{2} & y > 0, x = 0 \\ -\frac{\pi}{2} & y < 0, x = 0 \\ \text{undefined} & y = 0, x = 0 \end{cases} \tag{7.2}$$

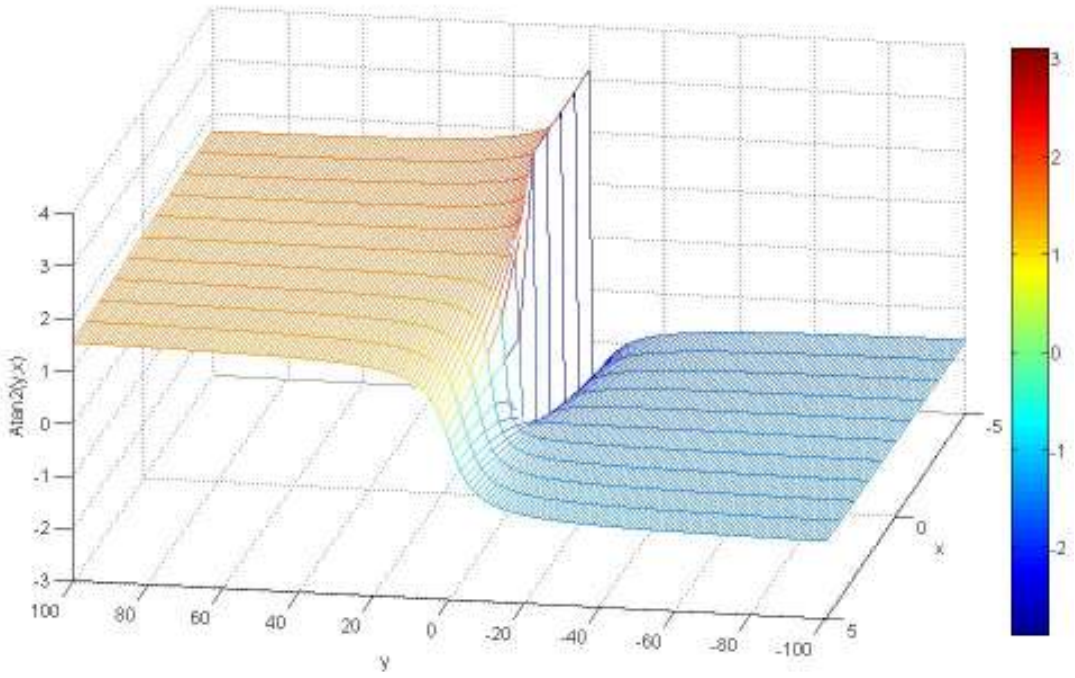

Figure 7.3 Three dimension plot of arctan2 function.

Now the principle stress orientation θ and phase retardation δ can be calculated using arctan2 functions as shown in equation 7.3 and 7.4 instead of equation 3.3 and 3.4.

$$\theta = \frac{1}{2} a\tan 2(I_5 - I_3, I_4 - I_6) \tag{7.3}$$

$$\alpha = a\tan 2\left[(I_5 - I_3)\sin 2\theta + (I_4 - I_6)\cos 2\theta,\ I_1 - I_2\right] \tag{7.4}$$

Using equations 7.3 and 7.4, the range of stress orientation θ is extended from (−π/4, π/4) to (−π/2, π/2) and the range of phase retardation δ is extended from (−π/2, π/2) to (−π, π). Now mathematically both the stress orientation θ and the phase retardation δ are sufficient to represent all the random stress states. The arctan2 function chooses one solution from the two possible solutions from equations 3.3 and 3.4 in the range of (−π/2, π/2).

By using the arctan2 function, the polariscope system can completely distinguish the two stress states at the boundaries. The principle stress orientations for the two stress states have a difference of π/2 though they have the same magnitude of maximum shear stress. Figure 7.4 (a) is the Phase map and principle stress orientation calculated by arctan2 function for a single crystal pure bending beam. Clearly, by applying arctan2 function, the uniaxial stress states between compressive and tensile stress can be distinguished by the principle stress orientation measured by the polariscope as shown in figure 7.4 (b).

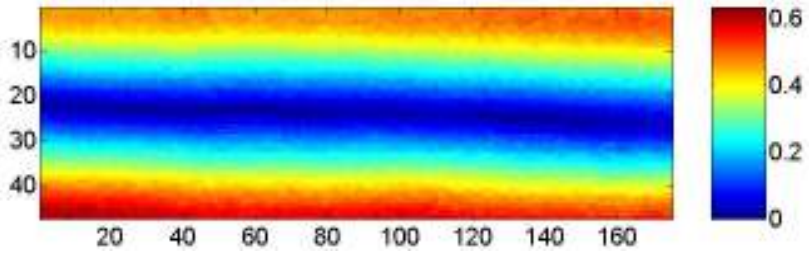

(a) Phase map

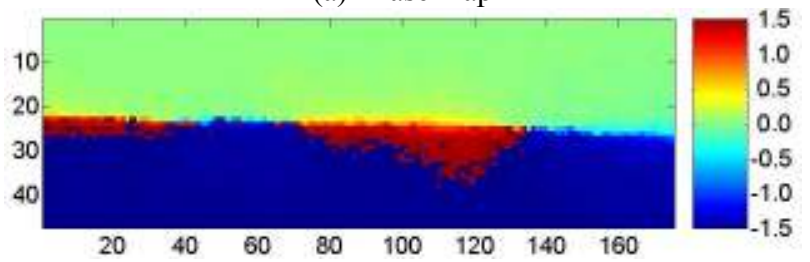

(b) Principle stress orientation

Figure 7.4 Phase map and principle stress orientation calculated by arctan2 function.

Although arctan2 function can completely distinguish the stress states at the boundary, it can't distinguish all the stress states in the middle of the samples as shown in figure 7.1. In this thesis, shear difference method is used to calculate full stress components from the measurement of polariscope. To use shear difference method, boundary conditions and a fully determined shear stress in the xy plane for the entire sample are needed. And it can be proved that by using arctan2 function, shear stresses in the xy plane are fully determined.

Table 7.1 shows the maximum shear stress calculated by the arctan2 function and the sign of τ_{xy}. The phase retardation δ is always positive, which leads to the fact that $\tau_{\max}$ is always positive. This contradicts the fact that the stress state $\tau_{\max}$ may be negative. Table 7.2 shows the calculated θ and δ using the second solution for θ in the range $[-\pi/2, \pi/2]$. In this case, $\tau_{\max}$ is negative. Table 7.1 and 7.2 show that the in-plane shear stress τ_{xy} will hold the same value and sign no matter which θ value we

choose in the range of (−π/2, π/2) , which proved that the in plane shear stresses are fully determined.

Table 7.1 Shear stresses calculated by the arctan2 function.

$I_5 - I_3$	$I_4 - I_6$	$\sin 2\theta$	$\cos 2\theta$	θ	δ	$\tau_{\max}$	$\tau_{xy} = \tau_{\max} \sin 2\theta$
+	+	+	+	$\left(0, \frac{\pi}{4}\right)$	+	+	+
+	–	+	-	$\left(\frac{\pi}{4}, \frac{\pi}{2}\right)$	+	+	+
-	+	-	+	$\left(-\frac{\pi}{4}, 0\right)$	+	+	-
-	-	-	-	$\left(-\frac{\pi}{2}, -\frac{\pi}{4}\right)$	+	+	-

Table 7.2 Shear stresses calculated by using the second solution of θ in (−π/2, π/2).

$I_5 - I_3$	$I_4 - I_6$	$\sin 2\theta$	$\cos 2\theta$	θ	δ	$\tau_{\max}$	$\tau_{xy} = \tau_{\max} \sin 2\theta$
+	+	-	-	$\left(-\frac{\pi}{2}, -\frac{\pi}{4}\right)$	-	-	+
+	–	–	+	$\left(-\frac{\pi}{4}, 0\right)$	-	-	+
-	+	+	–	$\left(\frac{\pi}{4}, \frac{\pi}{2}\right)$	-	-	-
-	-	+	+	$\left(0, \frac{\pi}{4}\right)$	-	-	-

7.3 Shear Difference Method

The Equations of equilibrium for a free body in x and y directions are shown in equation 6.4 and 6.5 respectively.

$$\frac{\partial \sigma_y}{\partial y} + \frac{\partial \tau_{xy}}{\partial x} = 0 \tag{7.4}$$

$$\frac{\partial \sigma_x}{\partial x} + \frac{\partial \tau_{yx}}{\partial y} = 0 \tag{7.5}$$

Equation 7.4 and 7.5 can be converted to Finite Element Analysis (FEA) form and at the free boundary of the beam traction forces are zero as shown in figure 7.5:

$$\left(\sigma_y\right)_j = \left(\sigma_y\right)_i - \int_i^j \frac{\partial \tau_{xy}}{\partial x} dy \qquad \left(\sigma_y\right)_{i=0} = 0 \tag{7.6}$$

$$\left(\sigma_x\right)_j = \left(\sigma_x\right)_i - \int_i^j \frac{\partial \tau_{yx}}{\partial y} dx \qquad \left(\sigma x\right)_{i=0} = 0 \tag{7.7}$$

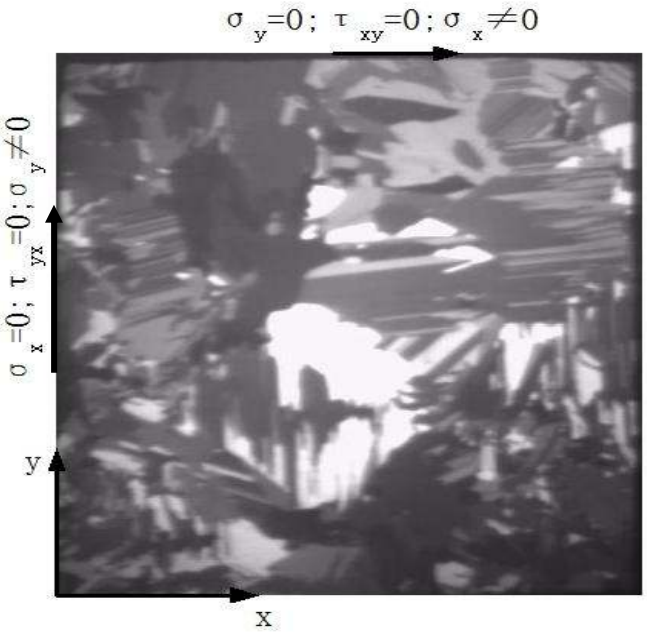

Figure 7.5 Boundary conditions of a 156×156 mm cast wafer.

The sample boundaries need to be properly captured when utilizing shear difference method. To calculate the normal stress, shear stress in the xy plane needs to be calculated first. Equation 7.8 is the transformation of stresses to the xy plane coordinates, where shear stress in the xy plane can be obtained.

$$\tau_{xy} = \frac{1}{2}\left|\sigma_1 - \sigma_2\right| \sin 2\theta = \tau \sin 2\theta = \frac{\lambda}{4\pi t C(\varphi,\theta)} \delta \sin 2\theta \tag{7.8}$$

Equation 7.9 is used to calculate the principal stresses after normal stresses in x and y directions are calculated using equations 7.6 and 7.7 respectively.

$$\sigma_{1,2} = \frac{\sigma_x + \sigma_y}{2} \pm \sqrt{\left(\frac{\sigma_x - \sigma_y}{2}\right)^2 + \tau_{xy}{}^2} \tag{7.9}$$

7.4 Stress Separation for Silicon Beams

To verify the shear difference method, four point bending, shown in Figure 5.4, was used to introduce a known stress field to a silicon beam. The residual stresses in the wafers were assumed to be negligible compared to the applied stresses. To further simplify the procedure, CZ beams were used.

The stress state of the CZ beam is shown as equation 7.10, which is a pure bending stress state with maximum shear of 32 MPa. In equation 7.10, y is the distance to the neutral axis.

$$\begin{bmatrix} \sigma_x & \tau_{xy} \\ \tau_{xy} & \sigma_y \end{bmatrix} = \begin{bmatrix} 32 \times \frac{y}{5} & 0 \\ 0 & 0 \end{bmatrix} \tag{7.10}$$

The maximum shear stress measured by the polariscope system is shown in figure 7.6. Since the residual stress in the CZ wafers is assumed negligible, the stress state in figure 7.6 is very close to a pure bending stress.

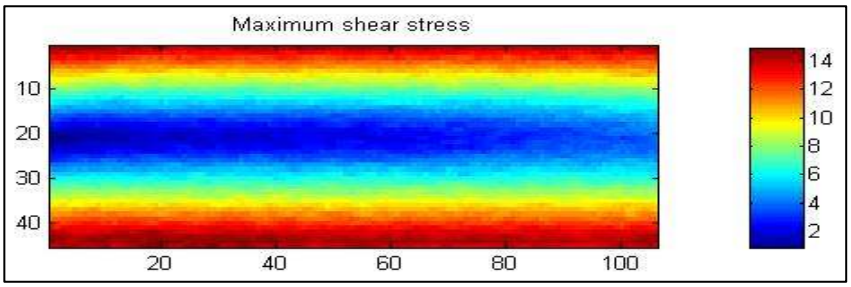

Figure 7.6 Bending stresses in CZ beam measured by polariscope.

The shear stresses in the xy plane are calculated from the polariscope measurement using equation 7.8, as shown in figure 7.7. The shear stresses in the xy plane are small since all the shear stress comes from the residual stress, which is assumed negligible in the CZ wafer.

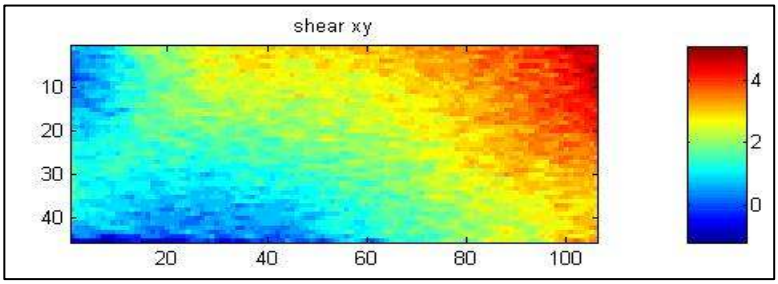

Figure 7.7 Shear stresses in the xy plane.

Finally, normal stresses in xy plane are calculated using equations 7.6 and 7.7, which are shown in figure 7.8 and 7.9 respectively. The normal stress in the x direction is uniform along the longitudinal direction and tensile at the bottom, compressive at the top. The maximum stress is close to 32 MPa. The stress in the y direction is small since all the

normal stresses in y direction comes from the residual stress. All of this shows that derived stress state is in good agreement with the applied stress.

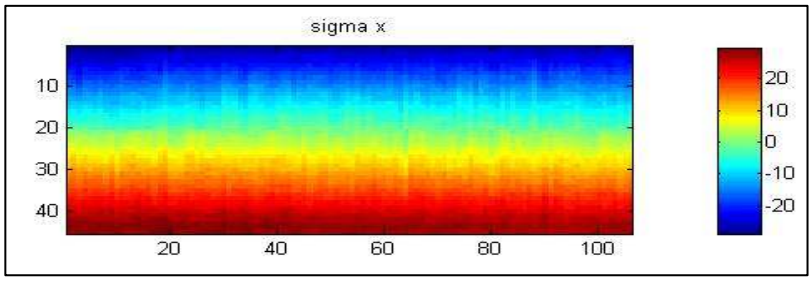

Figure 7.8 Normal stresses σ_x in xy plane.

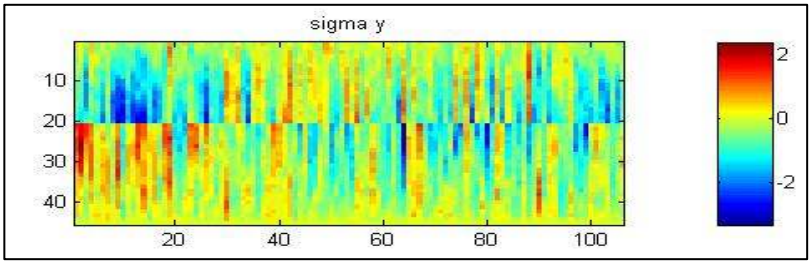

Figure 7.9 Normal stresses σ_y in xy plane.

The same methodology was applied to an EFG beam. The difference is that the EFG beam has a much bigger stress than CZ beam, which is shown in figure 7.10.

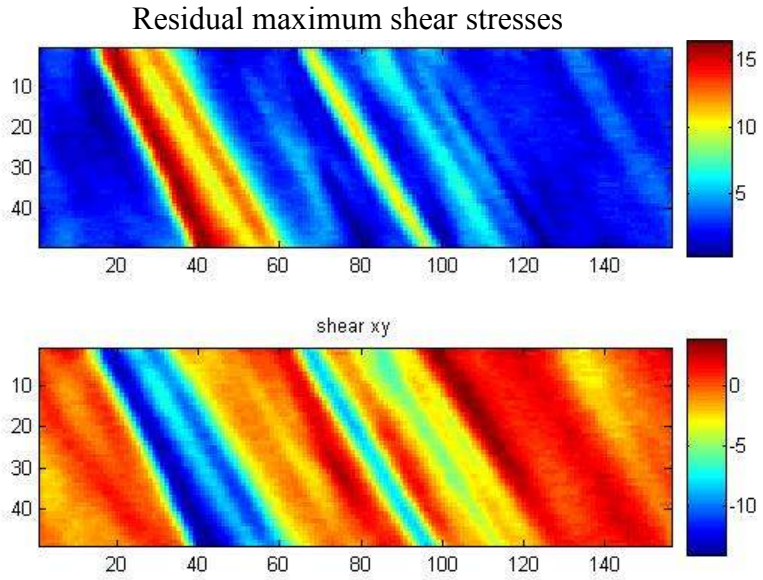

Figure 7.10 Residual shear stresses and shear stresses in xy plane.

Figure 7.11 shows the residual normal stresses in the xy plane obtained by shear difference method. The maximum tensile stress is about 20 MPa.

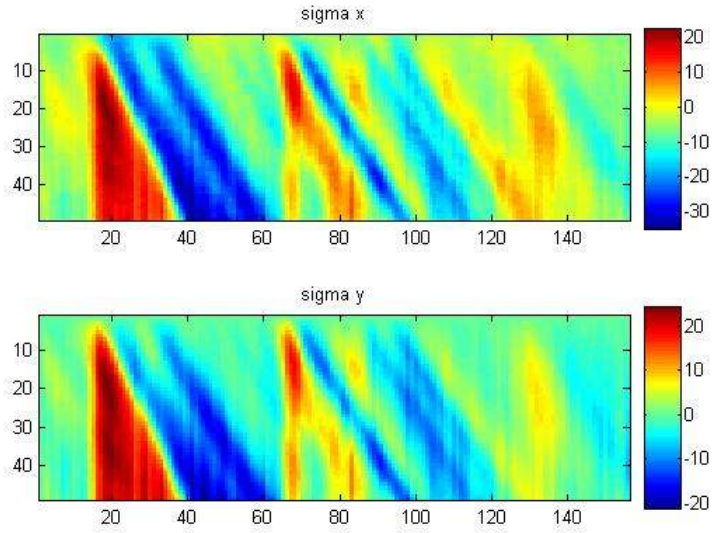

Figure 7.11 Residual normal stresses in the xy plane.

Four point bending stresses are applied to the beam and total maximum shear stresses including residual and applied stresses were measured using polariscope as shown in figure 7.12

.

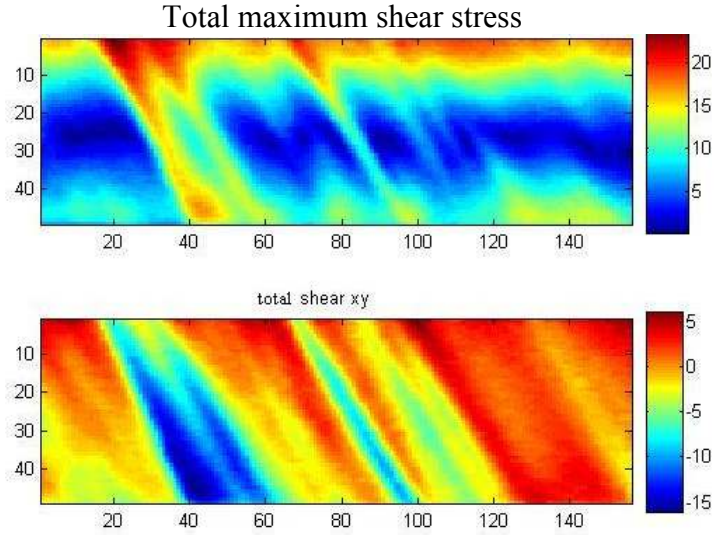

Figure 7.12 Total shear stresses and corresponding shear stresses in xy plane.

Figure 7.13 shows the total normal stresses including residual and applied stresses in the xy plane obtained by shear difference method. The maximum normal stress is about 40 MPa.

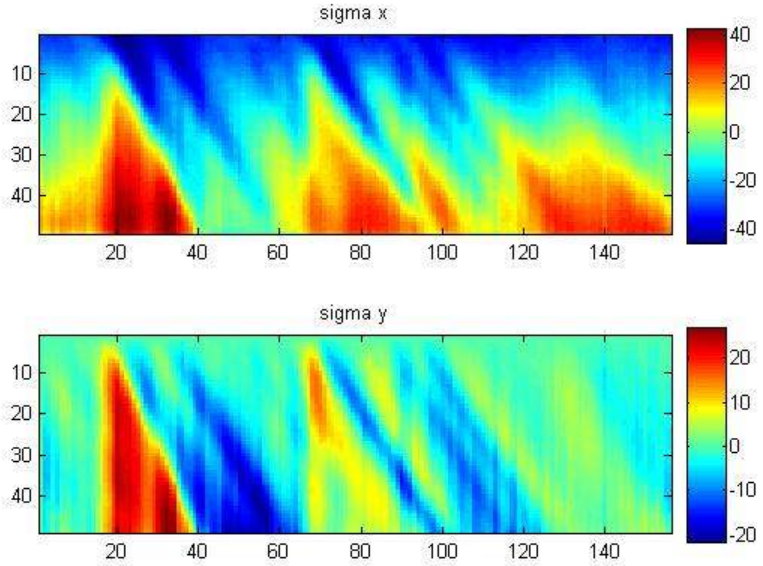

Figure 7.13 Total normal stresses in xy plane.

Finally, pure bending stress in the x direction can be calculated by subtracting the residual normal stress from the total stress, shown in figure 7.14, which is in good agreement with the applied stress.

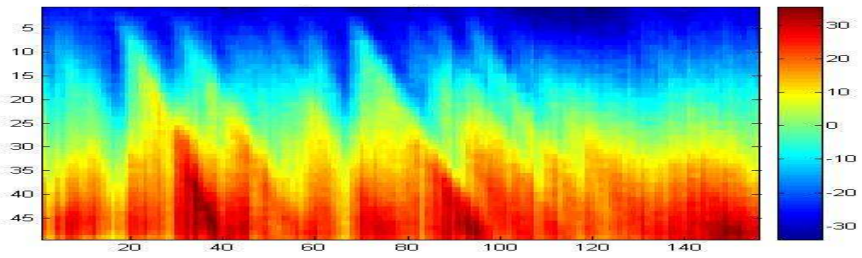

Figure 7.14 Four point bending stresses calculated by shear difference method.

7.5 Stress Separation for a Cast Silicon Wafer

The same procedure was preformed for 156×156 mm cast wafers. Residual stresses of the entire wafer were measured by the new polariscope system described in chapter 6. Figure 7.15 shows residual shear stresses and shear stresses in xy plane.

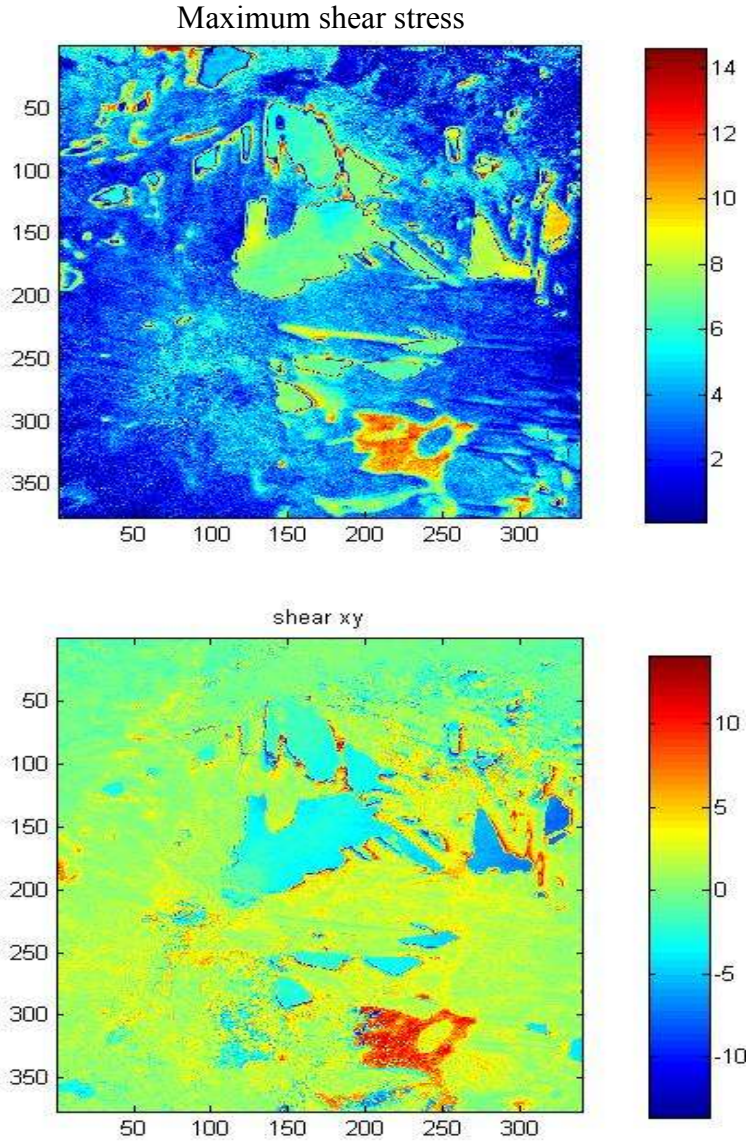

Figure 7.15 Maximum shear stresses and shear stresses for a 156mm cast wafer.

Normal stresses in x and y directions are calculated using equation 7.6 and 7.7 respectively. The maximum tensile stress is about 27 MPa as shown in figure 7.16. Due to the integration, errors are accumulated in the integration path. The error is less than 1 MPa within 10mm of the integration path.

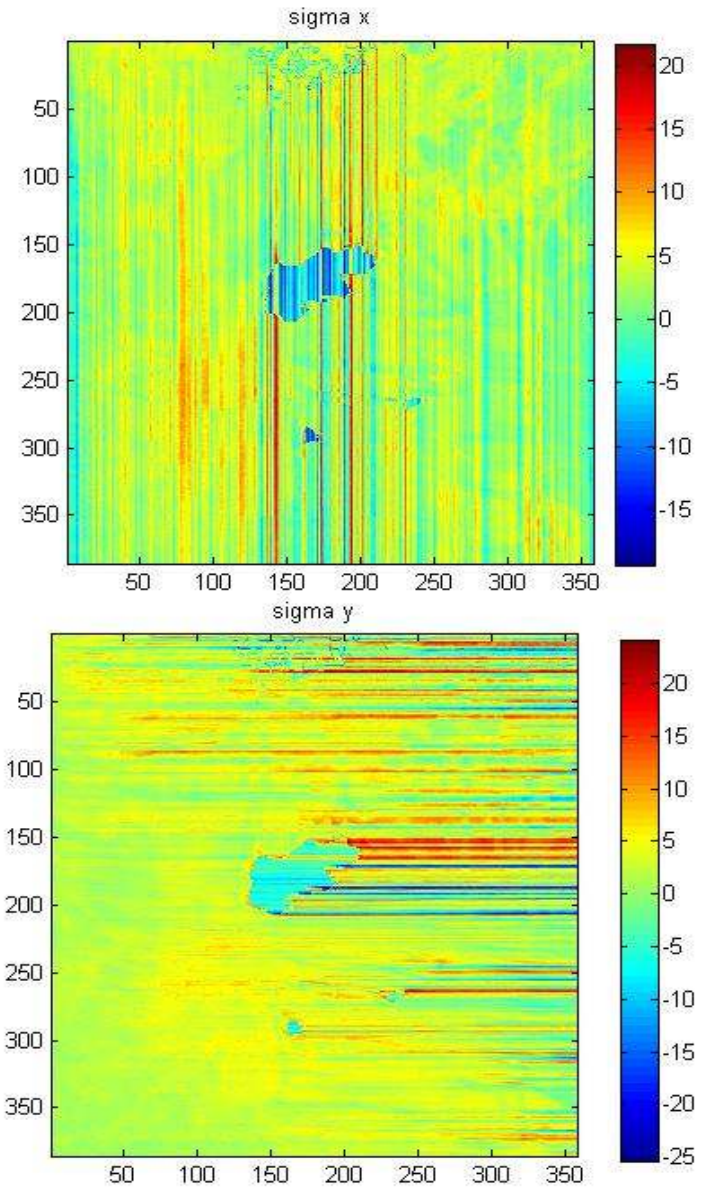

Figure 7.16 normal stresses in x and y direction

7.6 Conclusion

System ambiguity is resolved by using the arctan2 function. The shear difference method is used to calculate the full stress components. The methodology is first verified by successfully obtaining the full stress components of the four point bending beams. Finally, full stress components are obtained for the entire cast wafer. The accuracy is about 1 MPa within 10mm from the starting integration point.

Chapter 8

Thermal Stress Analysis and Simulation

8.1 Summary

In the measurement using circular polariscope as shown in figure 2.1, the wafer is illuminated by the light source. Since the energy profile on the wafer is non-uniform, the resulted temperature gradients will cause thermal stress in the wafer.

8.2 Thermal Transient Study

When measure stresses in cast wafers using polariscope, it takes a couple of seconds to obtain the thermal steady state. As mentioned in the earlier chapters, six phase stepping method is used to obtain the photoelastic parameters by rotating the second waveplate and polarizer six times. Usually the measurement takes about 15 seconds and the six images are not taken at the same time. If it is not under thermal steady state, the six images may not be taken under the same stress state due to the thermal stresses. Based on the measurement results of the cast wafers, measuring stresses in thermal transit state increases the measurement error dramatically. Therefore, it is critical to know how long it takes the system to reach thermal steady state.

A thermal transient model of the system was developed using ANSYS. Attachment A is the code of the thermal ANSYS model. The light source was simulated as a heat flux on the wafer surface. Although the power of the light source is 200 watt, the energy

hitting on the wafer is much smaller than 200 watt, which is about 10 watt because a small aperture was sited in front of the light source. The transient model calculated the whole field temperature of the wafer at different time point. The temperature of a node, which is located at the center of the wafer, was extracted and plotted with time, as shown in figure 8.1. It can be seen from figure 8.1 that it takes about 20 to 30 seconds to reach the thermal steady state. The result is very close to the experimental observation of the measurements of cast wafers.

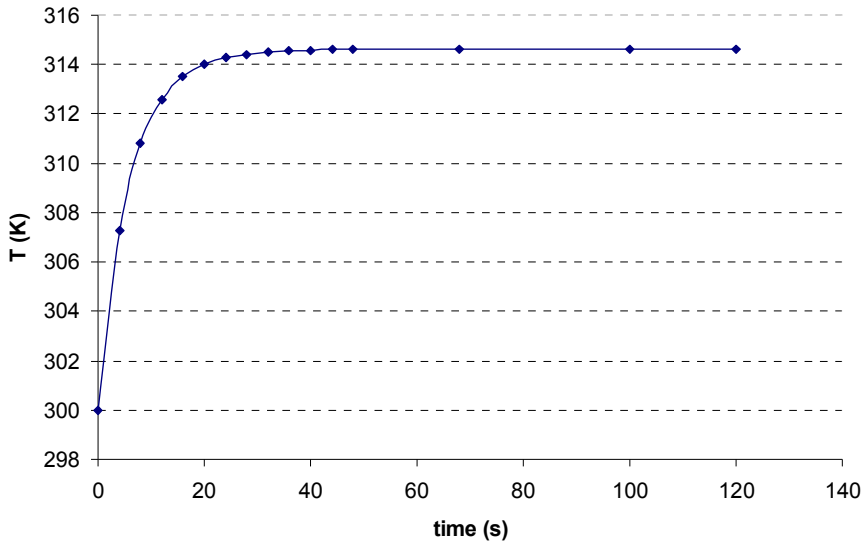

Figure 8.1 Temperatures vs. time of a node at the center of the wafer.

8.3 Thermal Stress at Steady State

Structural ANSYS model was created to calculate the thermal stress at the final steady state and Attachment B is the code of the structure ANSYS model. The temperature profile of the wafer is measured by a thermal camera as shown in figure 8.2. The highest temperature is about 24^0C and the lowest temperature is about 22^0C. The temperature difference is small since silicon is a good

thermal conductor. The free stress state is assumed to be 20^0C which is the room temperature. The temperature profile was imported into the structural model as the thermal load. The calculated thermal normal stresses in x, y directions and shear stresses in xy plane are shown in figure 8.3, 8.4 and 8.5 respectively. The maximum stress is below 1 MPa. Comparing to the residual stress magnitude of the wafers, the thermal stresses are negligible.

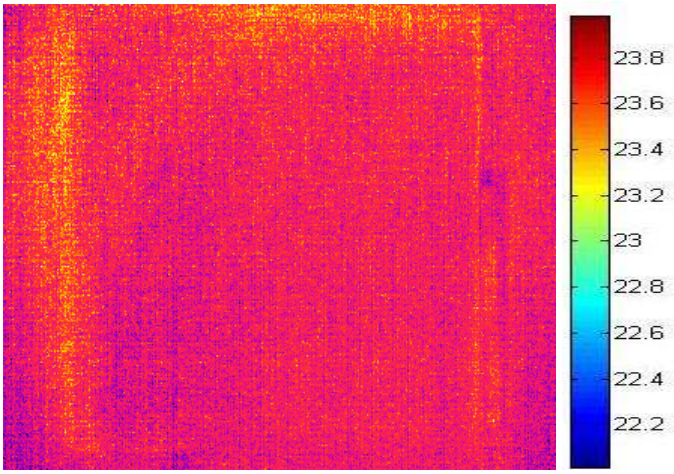

Figure 8.2 Temperature profile of a 156mm wafer measured by thermal camera.

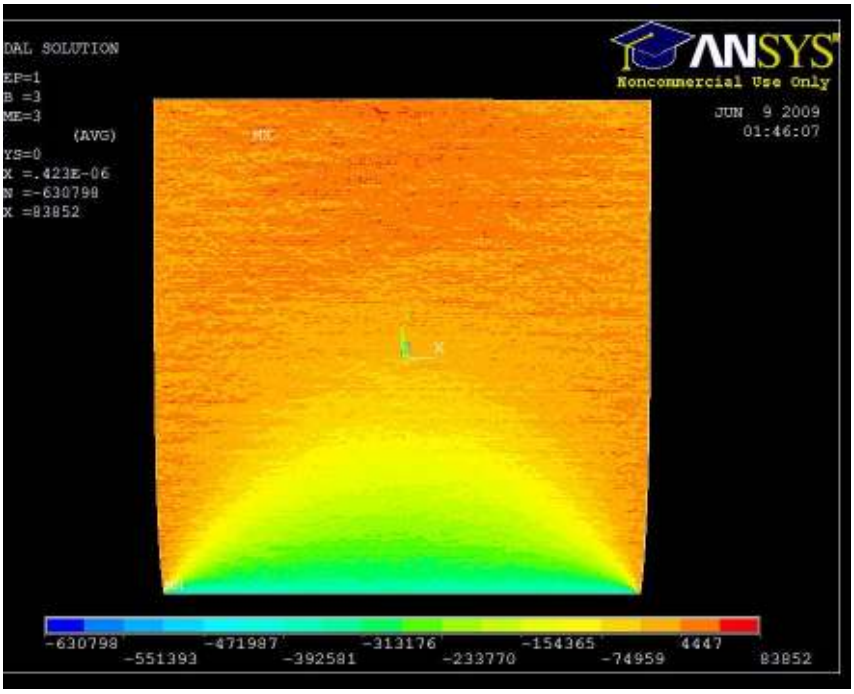

Figure 8.3 Thermal normal stresses in x direction.

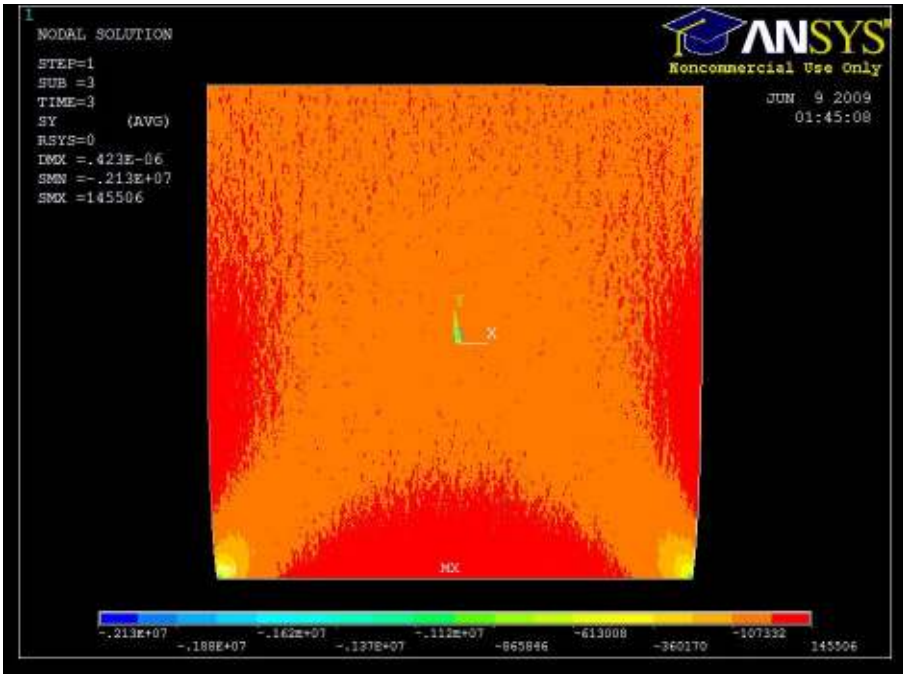

Figure 8.4 Thermal normal stresses in y direction.

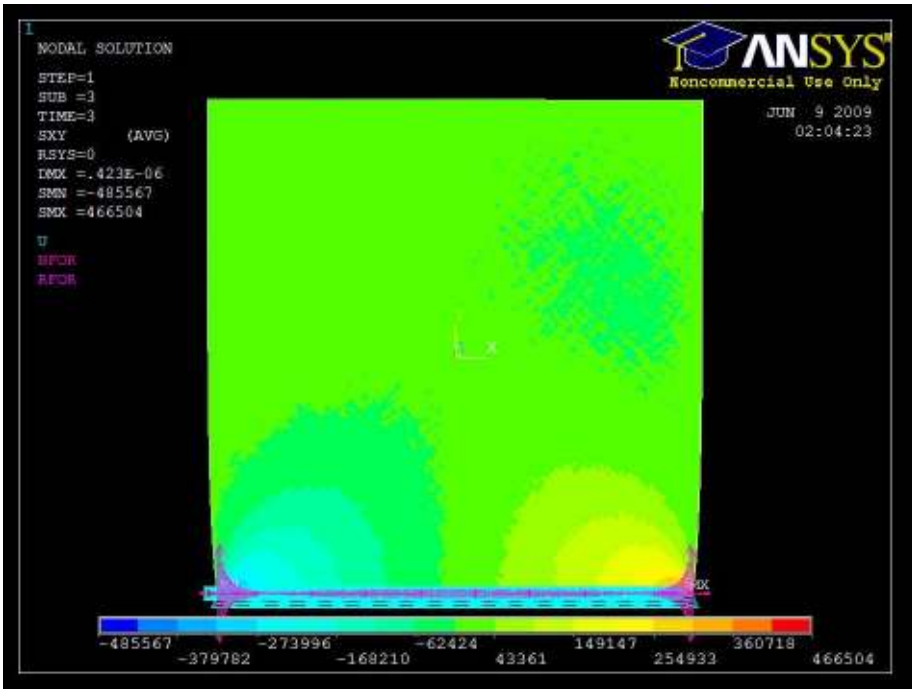

Figure 8.5 Thermal shear stresses in xy plane.

8.4 Conclusions

The time to obtain thermal steady state is calculated using thermal ANSYS model. Then the measured temperature profile is imported to a structural ANSYS model and the thermal stresses calculated from the model are negligible comparing to the stress magnitude in the wafers.

Chapter 9

System Alignment and Error Analysis

9.1 Summary

This chapter summarizes the method to align the system and the way to calibrate the camera. The results show that the error of the system is about 1 MPa.

9.2 Introduction

Traditional polariscope is usually used for a specimen with a thickness of the order of millimeters and stress level of 100 MPa, where multiple fringes can be observed and phase unwrapping is required to remove the discontinuity in the phase difference[60-62]. The error, which is of the order of a fractional fringe, is negligible compared with multiple fringes. However, for a photovoltaic silicon wafer with a thickness less than 300 μm and stress level around 10 MPa, only a partial fringe can be observed, and the error analysis is therefore crucial to determine the system reliability.

The errors associated with wavelength mismatch of the quarter waveplates has been analyzed by Patterson [63] [64]. His results show that the maximum error is of the order of 0.012 fringe order. In this chapter, the wavelength mismatch is not considered because the relatively narrow bandwidth (10 nm) of the monochromatic light obtained using the band pass filter. The error sources including the angular misalignment in the two waveplates and the two polarizers, and the digitization error in the image grabber are

analyzed by S, He [37]. In this thesis, the system alignment and the calibration of the infrared camera is presented. And the method to subtract the system error is also described.

9.3 System Alignment

The sources of error considered here is the misalignment of the light source, two waveplates, the polarizers, the lenses and the camera. The maximum error in stress is approximately 1.4 MPa [37], which is fairly large comparing to the residual stresses in the wafers and it is important to align the system carefully. In the case of there is no assistant equipments, such as the rails and stages, it is critical to have a standard procedure to align all the optics in the polariscope system.

As introduced in chapter 2, the circular polariscope uses a tungsten light source, which has visible light. Thus the alignment of the polariscope can be justified by checking the light path visually. Figure 9.1 shows the schematic of light path of the polariscope system. The double sides arrows mean that the light transmitted and reflected follow the same path after the system is aligned perfectly.

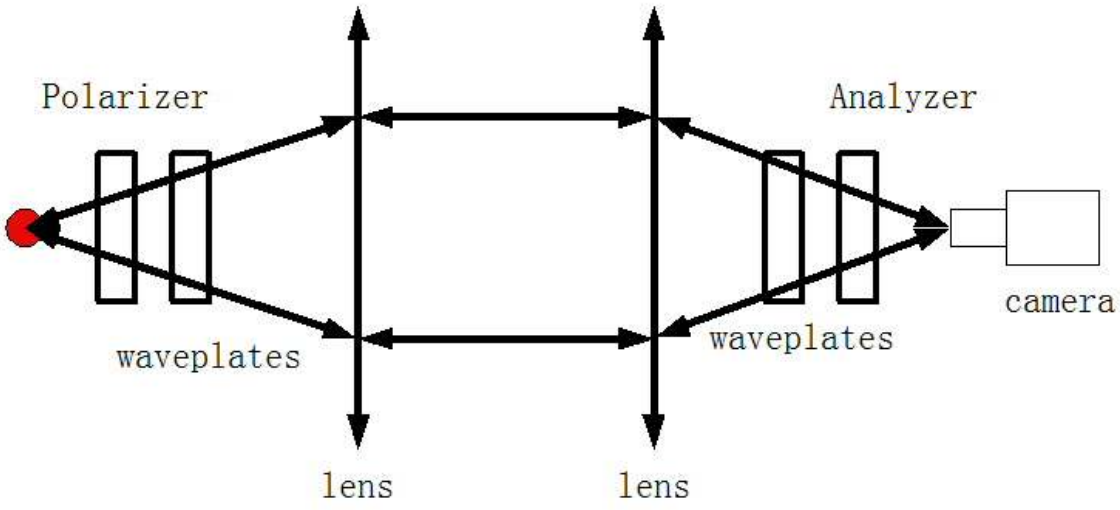

Figure 9.1 Schematic of light path through the circular polariscope.

An opaque plate with a circular hole of 5mm in diameter is at the focus of the light source which can convert the light source to a point source. An opaque paper can be used to check if the light source is focused at the hole. If a focused image of the filament is seen on the paper, then the light source is converted to a point source at the hole.

The next step is to align the two big lenses. The point source is placed at the focus of the first lens, which results in a collimated beam behind the first lens. If an opaque paper is behind the lens, a circular light spot can be seen as shown in figure 9.2. The size of the collimated beam should remain the same if the paper is moved further or closer to the lens.

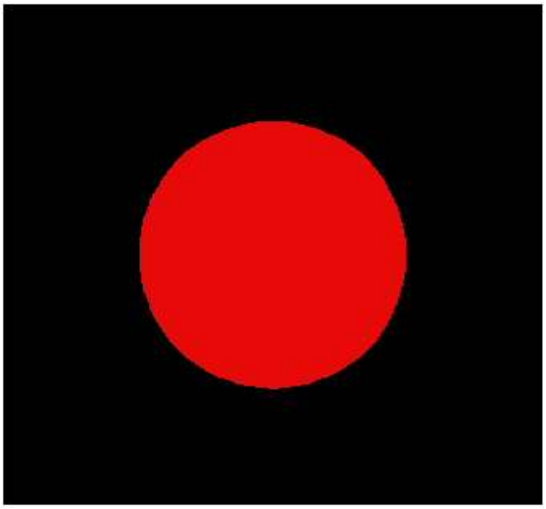

Figure 9.2 Collimated light spot between the two lenses.

The second lens is identical to the first one. So the first lens can be taken as the reference of the second lens. The alignment of the second lens can be examined by checking whether the point source is at the center of the reflected light or not.

After positioned the two big lenses, the sequence of aligning all the other optics is from the end to the beginning of the light path. In this way, the reflected light of any optic will not be blocked by the one in front of it. To make sure if the optics are properly aligned, the reflected light and the light source should be co-centered. Figure 9.3 is the reflected light pattern of the aligned system. The dashed lines mean that they can't be seen in the final setup.

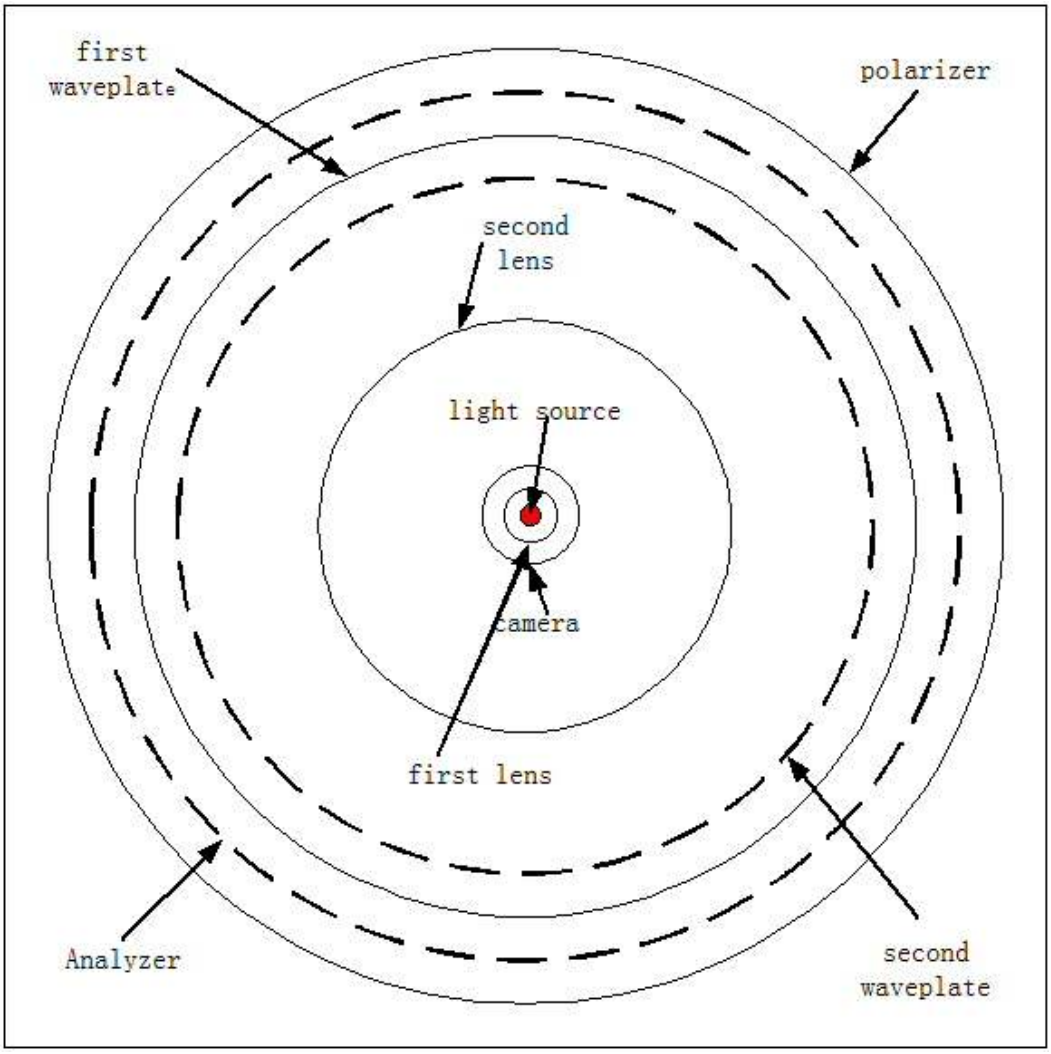

Figure 9.3 Reflected light pattern of different optics of the aligned polariscope.

After the system is aligned, light transmission image is captured by the infrared camera. Without any sample in the system, the image captured by the camera is a diffraction pattern of the circular hole, which is called airy disk as shown in figure 9.4. Both figure 9.3 and 9.4 need to be checked in order to make sure if the system is properly aligned.

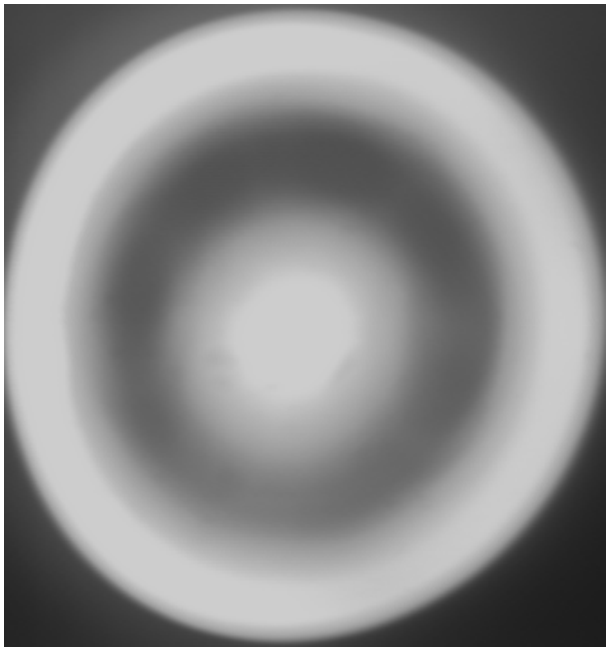

Figure 9.4 Airy disk of the aligned polariscope.

9.4 Calibration of the Infrared Camera

As described in chapter 3, the stress optic law is a linear function and six phase stepping method is used to extract the two photoelastic parameters, isoclinic angle and phase retardation. Equations 7.3 and 7.4 show that the two parameters are related to the light intensity of the six images. Figure 9.5 is the comparison of the first and second images, which shows that the intensity of the six images is quite different. Thus the camera response to light power should be linear. Otherwise, the gray level of the six images will represent wrong information of the light intensity.

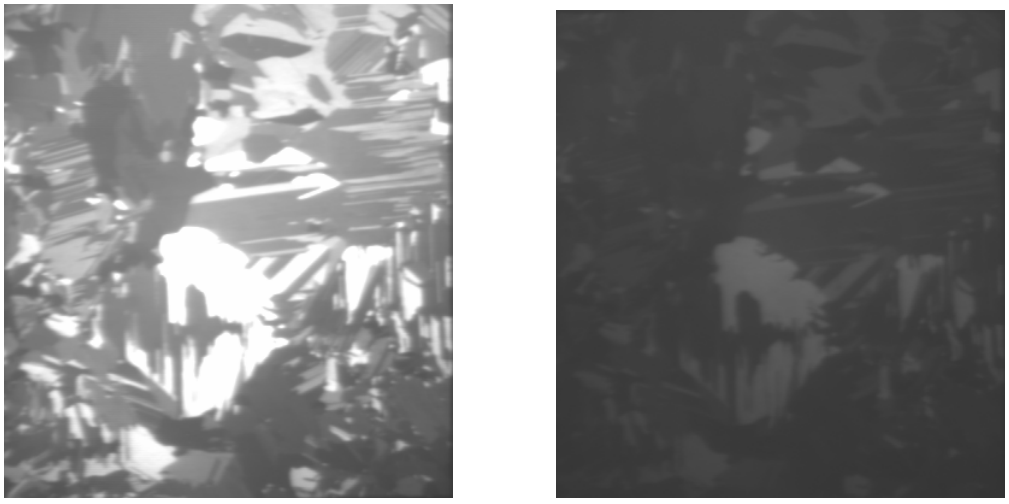

(a) (b)

Figure 9.5 The comparison of the first (a) and second (b) images of six phase stepping.

An image of a CZ wafer captured by the camera is shown in figure 9.6. The image is neither uniform nor symmetric due to the different response of the pixels in the infrared CCD camera. Experiments are designed to study the camera response to the light source power. Light source power was increased by five watt each time from 40 to 280. The response to the light power using highest camera gain is shown in figure 9.7 and the three lines come from the top left, middle and bottom right of the image respectively. It is obvious that the power response is non-linear. In order to fully interpret the full response, low and median camera gains are used to repeat the experiments and the response results are shown as figure 9.8 and 9.9 respectively.

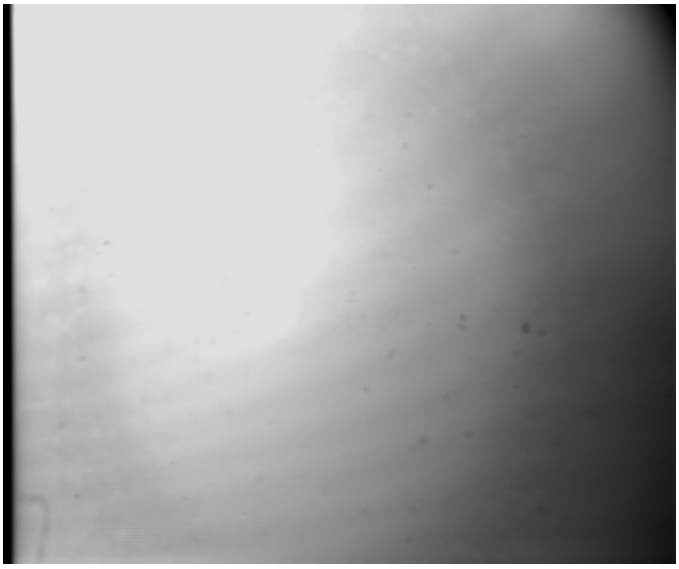

Figure 9.6 Light intensity image of a CZ wafer.

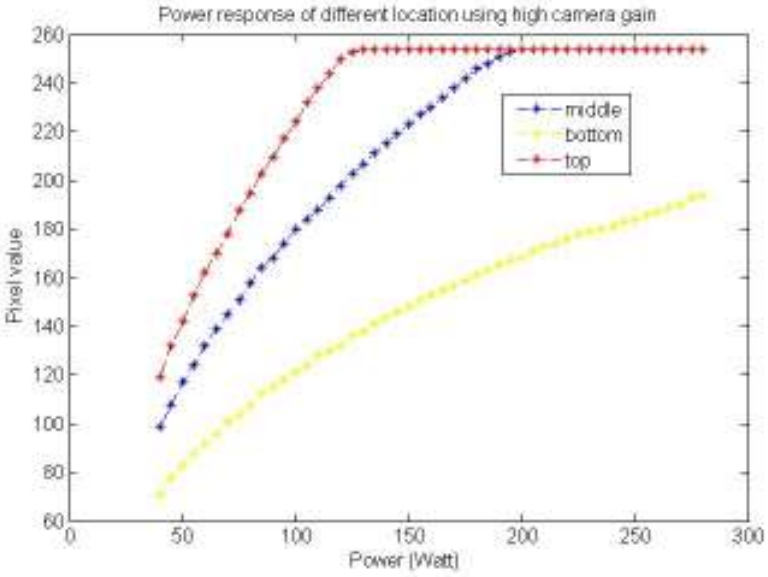

Figure 9.7 Camera responses using high camera gain.

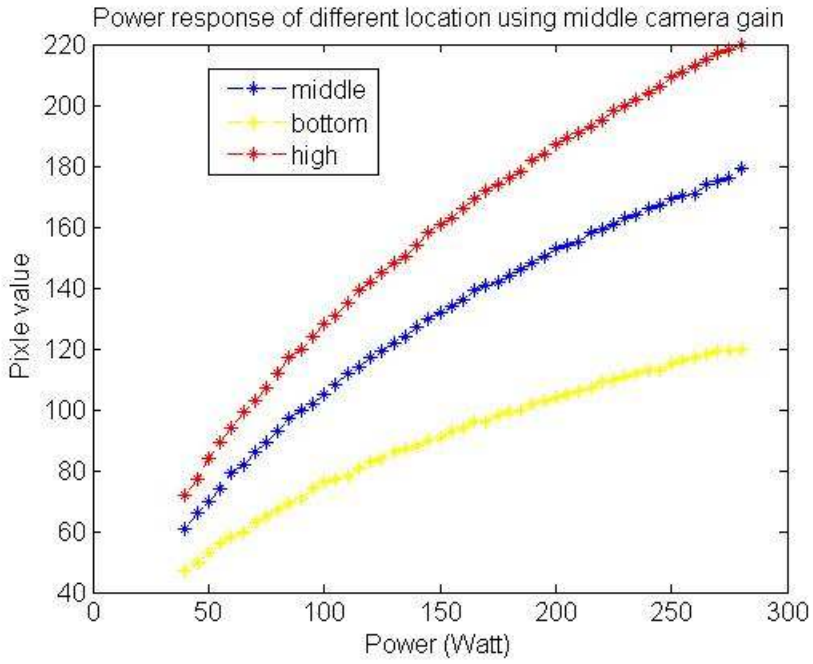

Figure 9.8 Camera responses using median camera gain.

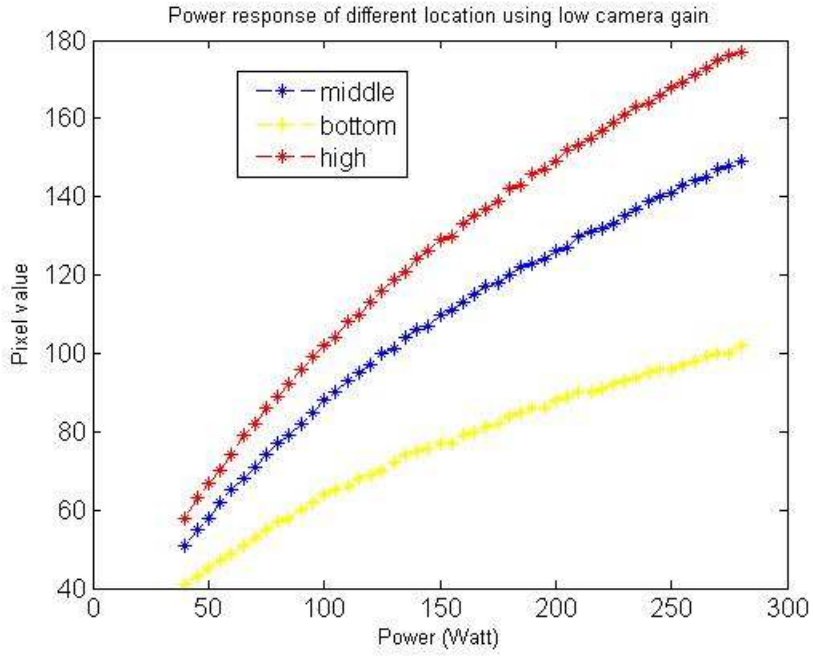

Figure 9.9 Camera responses using low camera gain.

Combining the three images from figure 9.6 to 9.8, a linear response of the camera can be found using piecewise function. Attachment C is the Matlab program to find the linear response of the camera. The program first search the pixel value of a certain location using the low camera gain in order to avoid saturation. If the pixel value falls into the range of the low camera gain, then a piecewise linear response of all the six images is simulated using low camera gain. Otherwise, keep searching using the median and high camera gain, until the program find the range containing the pixel value. Finally, the linear relations will be used to adjust all the six images simultaneously. Figure 9.10 shows images before and after adjusting the camera response. Image after adjusting the camera response has higher contrast and the difference between grain transmissions is enlarged.

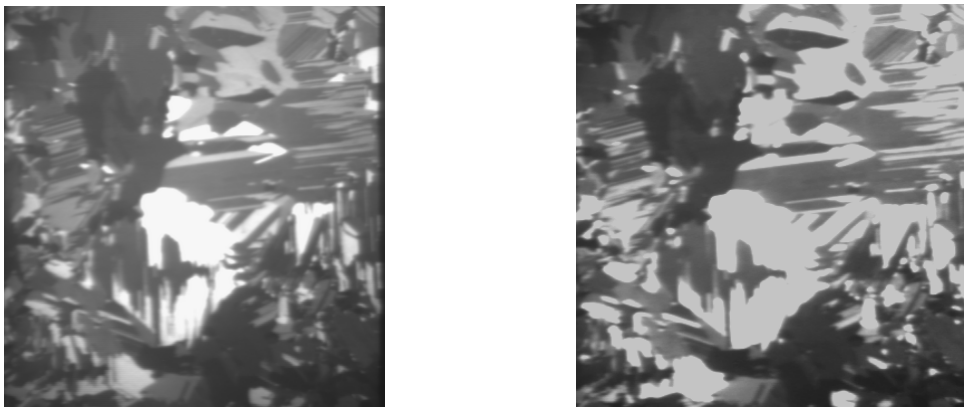

(a) (b)

Figure 9.10 Images before (a) and after (b) adjusting the camera response.

The maximum shear stresses are calculated from the adjusted six images. After calibrating the camera, systematic error is reduced dramatically, shown in figure 9.11. Grains can be seen much clearly after linearly adjusting the camera.

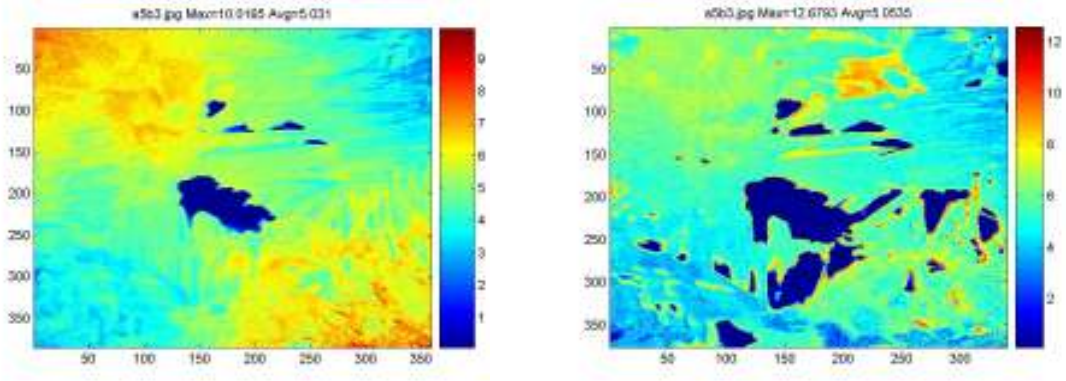

(a) (b)

Figure 9.11 Maximum shear stresses (a) before and after (b) adjusting the camera response.

9.5 System Error Analysis

To further reduce the system error, a stress free CZ wafer is measured by the polariscope and the phase map is shown in figure 9.12. Since the wafer is stress free, the phase retardation comes from the system error. For EFG wafers, which have high stress, it is not critical to get rid of the system error. But for the cast and single crystal wafers, which contain low stress, it is critical to subtract the system error.

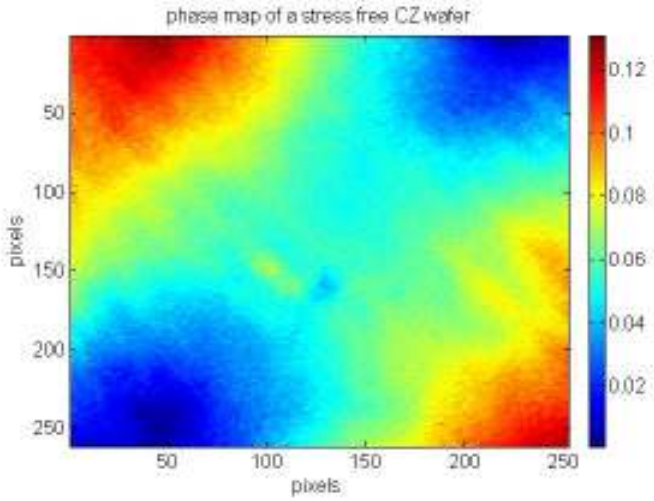

Figure 9.12 Phase map of a stress free wafer.

Figure 9.13 (a) and (b) are phase maps of CZ single crystal and cast wafer. It is obvious that they are containing the pattern of the stress free map. In order to obtain the pure residual stress state of the wafers, the system error needs to be subtracted from the phase map. Results are shown in figure 9.14 (a) and (b) respectively.

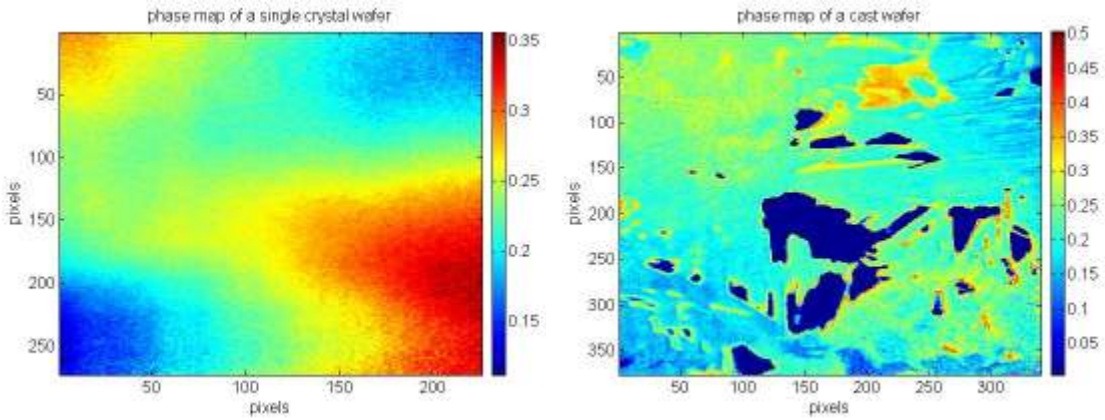

(a) (b)

Figure 9.13 Phase maps of single crystal wafer (a) and cast wafer (b).

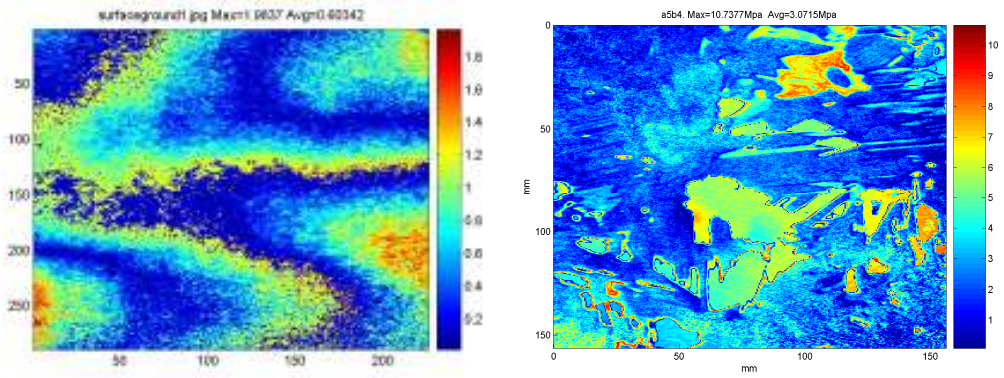

Figure 9.14 Stress maps of a CZ wafer (a) and cast wafer (b) after eliminating system error.

After subtracting the system error, stress pattern is removed from the stress map. For the cast wafers, stress difference between grains is much more evitable. After adjusting the camera and subtracting the system error, the accuracy of the polariscope system is increased to about 1 MPa.

9.6 Conclusion

System is aligned based on the light transmission path. The infrared camera is linearly calibrated in according to the linear stress optic law. System error is subtracted from the residual stress of the samples. The system error is reduced to 1 MPa.

Conclusions

The conclusions of this thesis are summarized as follows:

1. The stress-optic coefficients for different grain orientations and stress orientations were calibrated using four point bending experiments. The variation of the maximum stress optic coefficients to the minimum is about 1.7.

2. Grain orientations were characterized by light intensity of the images captured by an infrared camera in stead of x-ray diffraction. Among (100), (110), (111) orientations, (111) orientations were found to have the highest light transmission and (100) orientation has the lowest light transmission

3. A new polariscope system capable of in situ stress measurement of wafers as large as 156×156 mm was built. Location dependent stress optic coefficients were calibrated for the entire illuminating field of the system and applied to the residual stress measurement of multi crystalline silicon wafers.

4. A new formula was introduced to extend the range of the principle stress orientation from $\left(-\frac{\pi}{4},\frac{\pi}{4}\right)$ to $\left(-\frac{\pi}{2},\frac{\pi}{2}\right)$, and retardation from $(0,\pi)$ to $(0,2\pi)$. The ambiguity at the boundaries is eliminated completely. By

applying shear different method, full stress components are obtained for the entire wafer.

5. Error is reduced to 1 MPa by linearly calibrating the camera and subtracting the system pattern from the residual stress measurement. System is aligned based on the light transmission path.

6. Thermal model was built to study the thermal transient state using finite element method and structural model was also built to calculate the thermal stress induced by the light source. Thermal stresses were verified to be small comparing to the residual stress magnitude of wafers.

Appendix A

Thermal Transient Model Using ANSYS

```
/clear,nostart
/filname,thermal20transite,1
/prep7
antype,trans
!wafer geometric
BLC5,0,0,0.1,0.1,0.0002
CYL4,0,0,0.0375, , , ,0.0002
vsbv,1,2,,delete,keep
vsel,all
vglue,all
numcmp,volume
numcmp,area
numcmp,line
ET, 1, PLANE77
ET, 2, SOLID90

!defining material properties
mp,dens,1,2.33e3,,,,,
mp,kxx,1,149
```

```
mp,kyy,1,149

mp,kzz,1,149

mp,c,1,685.36


!meshing

type,1

mat,1

lsel,s,loc,z,-incc,incc

lplot

lsel,r,loc,x,-0.04-incc,0.04+incc

lplot

lsel,r,loc,y,-0.04,0.04

lplot

lesize,all,0.002

asel,s,area,,5

aplot

amesh,all


lsel,s,loc,y,-0.05-incc,-0.05+incc

lsel,a,loc,x,-0.05-incc,-0.05+incc

lsel,a,loc,y,0.05-incc,0.05+incc

lsel,a,loc,x,0.05-incc,0.05+incc

lplot
```

```
lsel,r,loc,z,-incc,incc
lplot
lesize,all,0.002
asel,s,area,,9
amesh,all
type,2
vsel,s,volu,,1
vsweep,all
vsel,s,volu,,2
vsweep,all
asel,s,loc,z,-incc,incc
aclear,all


*DEL,_FNCNAME
*DEL,_FNCMTID
*DEL,_FNCCSYS
*SET,_FNCNAME,'lightsou'
*SET,_FNCCSYS,0
! /INPUT,lightsource.func,,,1
*DIM,%_FNCNAME%,TABLE,6,10,1,,,,%_FNCCSYS%
!
! Begin of equation: 2716.16-643830.4*({X}^2+{Y}^2)
*SET,%_FNCNAME%(0,0,1), 0.0, -999
```

```
*SET,%_FNCNAME%(2,0,1), 0.0

*SET,%_FNCNAME%(3,0,1), 0.0

*SET,%_FNCNAME%(4,0,1), 0.0

*SET,%_FNCNAME%(5,0,1), 0.0

*SET,%_FNCNAME%(6,0,1), 0.0

*SET,%_FNCNAME%(0,1,1), 1.0, -1, 0, 2, 0, 0, 2

*SET,%_FNCNAME%(0,2,1), 0.0, -2, 0, 1, 2, 17, -1

*SET,%_FNCNAME%(0,3,1),   0, -1, 0, 2, 0, 0, 3

*SET,%_FNCNAME%(0,4,1), 0.0, -3, 0, 1, 3, 17, -1

*SET,%_FNCNAME%(0,5,1), 0.0, -1, 0, 1, -2, 1, -3

*SET,%_FNCNAME%(0,6,1), 0.0, -2, 0, 321915.2, 0, 0, -1

*SET,%_FNCNAME%(0,7,1), 0.0, -3, 0, 1, -2, 3, -1

*SET,%_FNCNAME%(0,8,1), 0.0, -1, 0, 1358.08, 0, 0, -3

*SET,%_FNCNAME%(0,9,1), 0.0, -2, 0, 1, -1, 2, -3

*SET,%_FNCNAME%(0,10,1), 0.0, 99, 0, 1, -2, 0, 0

! End of equation: 2716.16-643830.4*({X}^2+{Y}^2)

! LGWRITE,'funct','lgw','C:\IN-BOX\LCVD-SIC\STRESS\',COMMENT


!Specify BCs

*set,incc,1e-10

asel,s,loc,y,-0.05-incc,-0.05+incc

asel,a,loc,x,-0.05-incc,-0.05+incc

da,all,temp,300,0
```

```
asel,s,area,,5
sfa,all,,hflux,%lightsou%

!sfa,all,,hflux,1000
asel,s,loc,y,-0.05-incc,-0.05+incc
asel,a,loc,x,-0.05-incc,-0.05+incc
asel,a,area,,5
asel,inve
aplot
SFA,all,1,CONV, 30 ,300

/SOLU
nsel,all
tunif,300
vsel,s,loc,z, -incc,0.0002+incc
nplot
cm,laserspot,node
outres,nsol,all,laserspot
kbc,1
time,120
nsubst,30
allsel,all
solve
```

Appendix B

Structure Model Using ANSYS

```
/clear,nostart
/filname,struct2d,1
/prep7
!wafer geometric
BLC5,0,0,0.156,0.156
ET, 1, PLANE42
!r,1,,,0.0002
!et,1,plane42
!ET, 2, SOLID95
!defining material properties
mp,dens,1,2.33e3,,,,,
!mp,kxx,1,149
!mp,kyy,1,149
!mp,kzz,1,149
!mp,c,1,685.36
mp,ctex,1,2.6e-6
mp,ctey,1,2.6e-6
!mp,ctez,1,2.6e-6
mp,prxy,1,0.17
```

```
mp,reft,1,23
mp,ex,1,15e10
!meshing
type,1
mat,1
lsel,s,loc,y,-0.078-incc,-0.078+incc
lsel,a,loc,x,-0.078-incc,-0.078+incc
lsel,a,loc,y,0.078-incc,0.078+incc
lsel,a,loc,x,0.078-incc,0.078+incc
lplot
lsel,r,loc,z,-incc,incc
!lplot
lesize,all,0.0006
asel,s,area,,1
amesh,all

*dim,Txy1,table,260,130,1,x,y,
*Tread,Txy1,silicon_wafer9_1,txt,,
*dim,Txy2,table,260,130,1,x,y,
*Tread,Txy2,silicon_wafer9_2,txt,,
*set,incc,1e-10
*do,i,1,260
*do,j,1,130
```

```
nsel,s,loc,x,-0.078+0.0006*(i-1)-incc,-0.078+0.0006*(i-1)+incc
nsel,r,loc,y,0.078-0.0006*(j-1)-incc,0.078-0.0006*(j-1)+incc
bf,all,temp,txy1(i,j)
*enddo
*enddo
*do,i,1,260
*do,j,131,260
nsel,s,loc,x,-0.078+0.0006*(i-1)-incc,-0.078+0.0006*(i-1)+incc
nsel,r,loc,y,0.078-0.0006*(j-1)-incc,0.078-0.0006*(j-1)+incc
bf,all,temp,txy2(i,j-130)
*enddo
*enddo

asel,s,area,,1
aplot
Bfa,all,temp,%Txy%
!tunif,23
!type,2
!mat,1
!vsel,s,volu,,1
!vsweep,all
!asel,s,loc,z,-incc,incc
!aclear,all
```

```
!Specify BCs
*set,incc,1e-10
lsel,s,loc,y,-0.078-incc,-0.078+incc
dl,all,,all,0
!dl,all,,uy,0
!lsel,s,loc,x,-0.078-incc,-0.078+incc
!dl,all,,ux,0
!dl,all,,uy,0
!lsel,s,loc,x,0.078-incc,0.078+incc
!dl,all,,ux,0
!dl,all,,uy,0
!lsel,s,loc,y,0.078-incc,0.078+incc
!dl,all,,ux,0
!dl,all,,uy,0
FINISH
/SOL
kbc,0
time,3
nsubst,3
!ldread,temp,1,,,,thermal20for2d,rth
allsel,all
solve
FINISH
```

Appendix C

Matlab Code for Adjusting Camera Response

```
clear;
%%% load the images at different power%%%%
I1(1:480,1:640,1)=imread('e:\experiments\memc\response\top\40.bmp');
I1(1:480,1:640,2)=imread('e:\experiments\memc\response\top\45.bmp');
I1(1:480,1:640,3)=imread('e:\experiments\memc\response\top\50.bmp');
I1(1:480,1:640,4)=imread('e:\experiments\memc\response\top\55.bmp');
I1(1:480,1:640,5)=imread('e:\experiments\memc\response\top\60.bmp');
I1(1:480,1:640,6)=imread('e:\experiments\memc\response\top\65.bmp');
I1(1:480,1:640,7)=imread('e:\experiments\memc\response\top\70.bmp');
I1(1:480,1:640,8)=imread('e:\experiments\memc\response\top\75.bmp');
I1(1:480,1:640,9)=imread('e:\experiments\memc\response\top\80.bmp');
I1(1:480,1:640,10)=imread('e:\experiments\memc\response\top\85.bmp');
I1(1:480,1:640,11)=imread('e:\experiments\memc\response\top\90.bmp');
I1(1:480,1:640,12)=imread('e:\experiments\memc\response\top\95.bmp');
I1(1:480,1:640,13)=imread('e:\experiments\memc\response\top\100.bmp');
I1(1:480,1:640,14)=imread('e:\experiments\memc\response\top\105.bmp');
I1(1:480,1:640,15)=imread('e:\experiments\memc\response\top\110.bmp');
I1(1:480,1:640,16)=imread('e:\experiments\memc\response\top\115.bmp');
I1(1:480,1:640,17)=imread('e:\experiments\memc\response\top\120.bmp');
```

```
I1(1:480,1:640,18)=imread('e:\experiments\memc\response\top\125.bmp');
I1(1:480,1:640,19)=imread('e:\experiments\memc\response\top\130.bmp');
I1(1:480,1:640,20)=imread('e:\experiments\memc\response\top\135.bmp');
I1(1:480,1:640,21)=imread('e:\experiments\memc\response\top\140.bmp');
I1(1:480,1:640,22)=imread('e:\experiments\memc\response\top\145.bmp');
I1(1:480,1:640,23)=imread('e:\experiments\memc\response\top\150.bmp');
I1(1:480,1:640,24)=imread('e:\experiments\memc\response\top\155.bmp');
I1(1:480,1:640,25)=imread('e:\experiments\memc\response\top\160.bmp');
I1(1:480,1:640,26)=imread('e:\experiments\memc\response\top\165.bmp');
I1(1:480,1:640,27)=imread('e:\experiments\memc\response\top\170.bmp');
I1(1:480,1:640,28)=imread('e:\experiments\memc\response\top\175.bmp');
I1(1:480,1:640,29)=imread('e:\experiments\memc\response\top\180.bmp');
I1(1:480,1:640,30)=imread('e:\experiments\memc\response\top\185.bmp');
I1(1:480,1:640,31)=imread('e:\experiments\memc\response\top\190.bmp');
I1(1:480,1:640,32)=imread('e:\experiments\memc\response\top\195.bmp');
I1(1:480,1:640,33)=imread('e:\experiments\memc\response\top\200.bmp');
I1(1:480,1:640,34)=imread('e:\experiments\memc\response\top\205.bmp');
I1(1:480,1:640,35)=imread('e:\experiments\memc\response\top\210.bmp');
I1(1:480,1:640,36)=imread('e:\experiments\memc\response\top\215.bmp');
I1(1:480,1:640,37)=imread('e:\experiments\memc\response\top\220.bmp');
I1(1:480,1:640,38)=imread('e:\experiments\memc\response\top\225.bmp');
I1(1:480,1:640,39)=imread('e:\experiments\memc\response\top\230.bmp');
I1(1:480,1:640,40)=imread('e:\experiments\memc\response\top\235.bmp');
```

```
I1(1:480,1:640,41)=imread('e:\experiments\memc\response\top\240.bmp');
I1(1:480,1:640,42)=imread('e:\experiments\memc\response\top\245.bmp');
I1(1:480,1:640,43)=imread('e:\experiments\memc\response\top\250.bmp');
I1(1:480,1:640,44)=imread('e:\experiments\memc\response\top\255.bmp');
I1(1:480,1:640,45)=imread('e:\experiments\memc\response\top\260.bmp');
I1(1:480,1:640,46)=imread('e:\experiments\memc\response\top\265.bmp');
I1(1:480,1:640,47)=imread('e:\experiments\memc\response\top\270.bmp');
I1(1:480,1:640,48)=imread('e:\experiments\memc\response\top\275.bmp');
I1(1:480,1:640,49)=imread('e:\experiments\memc\response\top\280.bmp');
%%%% plot pixel level response to power%%%
%for i=1:49
   % o1(i)=I1(240,320,i);
    %p1(i)=I1(400,400,i);
    %q1(i)=I1(50,50,i);
%end
%x=(40:5:280);
%figure;
%plot(x,o1,'b*--')
%hold on
%plot(x,p1,'b*--')
%plot(x,q1,'b*--')
I2(1:480,1:640,1)=imread('e:\experiments\memc\response\middle\40.bmp');
I2(1:480,1:640,2)=imread('e:\experiments\memc\response\middle\45.bmp');
```

```
I2(1:480,1:640,3)=imread('e:\experiments\memc\response\middle\50.bmp');
I2(1:480,1:640,4)=imread('e:\experiments\memc\response\middle\55.bmp');
I2(1:480,1:640,5)=imread('e:\experiments\memc\response\middle\60.bmp');
I2(1:480,1:640,6)=imread('e:\experiments\memc\response\middle\65.bmp');
I2(1:480,1:640,7)=imread('e:\experiments\memc\response\middle\70.bmp');
I2(1:480,1:640,8)=imread('e:\experiments\memc\response\middle\75.bmp');
I2(1:480,1:640,9)=imread('e:\experiments\memc\response\middle\80.bmp');
I2(1:480,1:640,10)=imread('e:\experiments\memc\response\middle\85.bmp');
I2(1:480,1:640,11)=imread('e:\experiments\memc\response\middle\90.bmp');
I2(1:480,1:640,12)=imread('e:\experiments\memc\response\middle\95.bmp');
I2(1:480,1:640,13)=imread('e:\experiments\memc\response\middle\100.bmp');
I2(1:480,1:640,14)=imread('e:\experiments\memc\response\middle\105.bmp');
I2(1:480,1:640,15)=imread('e:\experiments\memc\response\middle\110.bmp');
I2(1:480,1:640,16)=imread('e:\experiments\memc\response\middle\115.bmp');
I2(1:480,1:640,17)=imread('e:\experiments\memc\response\middle\120.bmp');
I2(1:480,1:640,18)=imread('e:\experiments\memc\response\middle\125.bmp');
I2(1:480,1:640,19)=imread('e:\experiments\memc\response\middle\130.bmp');
I2(1:480,1:640,20)=imread('e:\experiments\memc\response\middle\135.bmp');
I2(1:480,1:640,21)=imread('e:\experiments\memc\response\middle\140.bmp');
I2(1:480,1:640,22)=imread('e:\experiments\memc\response\middle\145.bmp');
I2(1:480,1:640,23)=imread('e:\experiments\memc\response\middle\150.bmp');
I2(1:480,1:640,24)=imread('e:\experiments\memc\response\middle\155.bmp');
I2(1:480,1:640,25)=imread('e:\experiments\memc\response\middle\160.bmp');
```

```
I2(1:480,1:640,26)=imread('e:\experiments\memc\response\middle\165.bmp');
I2(1:480,1:640,27)=imread('e:\experiments\memc\response\middle\170.bmp');
I2(1:480,1:640,28)=imread('e:\experiments\memc\response\middle\175.bmp');
I2(1:480,1:640,29)=imread('e:\experiments\memc\response\middle\180.bmp');
I2(1:480,1:640,30)=imread('e:\experiments\memc\response\middle\185.bmp');
I2(1:480,1:640,31)=imread('e:\experiments\memc\response\middle\190.bmp');
I2(1:480,1:640,32)=imread('e:\experiments\memc\response\middle\195.bmp');
I2(1:480,1:640,33)=imread('e:\experiments\memc\response\middle\200.bmp');
I2(1:480,1:640,34)=imread('e:\experiments\memc\response\middle\205.bmp');
I2(1:480,1:640,35)=imread('e:\experiments\memc\response\middle\210.bmp');
I2(1:480,1:640,36)=imread('e:\experiments\memc\response\middle\215.bmp');
I2(1:480,1:640,37)=imread('e:\experiments\memc\response\middle\220.bmp');
I2(1:480,1:640,38)=imread('e:\experiments\memc\response\middle\225.bmp');
I2(1:480,1:640,39)=imread('e:\experiments\memc\response\middle\230.bmp');
I2(1:480,1:640,40)=imread('e:\experiments\memc\response\middle\235.bmp');
I2(1:480,1:640,41)=imread('e:\experiments\memc\response\middle\240.bmp');
I2(1:480,1:640,42)=imread('e:\experiments\memc\response\middle\245.bmp');
I2(1:480,1:640,43)=imread('e:\experiments\memc\response\middle\250.bmp');
I2(1:480,1:640,44)=imread('e:\experiments\memc\response\middle\255.bmp');
I2(1:480,1:640,45)=imread('e:\experiments\memc\response\middle\260.bmp');
I2(1:480,1:640,46)=imread('e:\experiments\memc\response\middle\265.bmp');
I2(1:480,1:640,47)=imread('e:\experiments\memc\response\middle\270.bmp');
I2(1:480,1:640,48)=imread('e:\experiments\memc\response\middle\275.bmp');
```

```
I2(1:480,1:640,49)=imread('e:\experiments\memc\response\middle\280.bmp');


%for i=1:49
    %o1(i)=I2(240,320,i);
   % p1(i)=I2(400,400,i);
    %q1(i)=I2(50,50,i);
%end
%x=(40:5:280);
%figure;
%plot(x,o1,'b*--')
%hold on
%plot(x,p1,'b*--')
%plot(x,q1,'b*--')


I3(1:480,1:640,1)=imread('e:\experiments\memc\response\bottom\40.bmp');
I3(1:480,1:640,2)=imread('e:\experiments\memc\response\bottom\45.bmp');
I3(1:480,1:640,3)=imread('e:\experiments\memc\response\bottom\50.bmp');
I3(1:480,1:640,4)=imread('e:\experiments\memc\response\bottom\55.bmp');
I3(1:480,1:640,5)=imread('e:\experiments\memc\response\bottom\60.bmp');
I3(1:480,1:640,6)=imread('e:\experiments\memc\response\bottom\65.bmp');
I3(1:480,1:640,7)=imread('e:\experiments\memc\response\bottom\70.bmp');
I3(1:480,1:640,8)=imread('e:\experiments\memc\response\bottom\75.bmp');
I3(1:480,1:640,9)=imread('e:\experiments\memc\response\bottom\80.bmp');
```

```
I3(1:480,1:640,10)=imread('e:\experiments\memc\response\bottom\85.bmp');
I3(1:480,1:640,11)=imread('e:\experiments\memc\response\bottom\90.bmp');
I3(1:480,1:640,12)=imread('e:\experiments\memc\response\bottom\95.bmp');
I3(1:480,1:640,13)=imread('e:\experiments\memc\response\bottom\100.bmp');
I3(1:480,1:640,14)=imread('e:\experiments\memc\response\bottom\105.bmp');
I3(1:480,1:640,15)=imread('e:\experiments\memc\response\bottom\110.bmp');
I3(1:480,1:640,16)=imread('e:\experiments\memc\response\bottom\115.bmp');
I3(1:480,1:640,17)=imread('e:\experiments\memc\response\bottom\120.bmp');
I3(1:480,1:640,18)=imread('e:\experiments\memc\response\bottom\125.bmp');
I3(1:480,1:640,19)=imread('e:\experiments\memc\response\bottom\130.bmp');
I3(1:480,1:640,20)=imread('e:\experiments\memc\response\bottom\135.bmp');
I3(1:480,1:640,21)=imread('e:\experiments\memc\response\bottom\140.bmp');
I3(1:480,1:640,22)=imread('e:\experiments\memc\response\bottom\145.bmp');
I3(1:480,1:640,23)=imread('e:\experiments\memc\response\bottom\150.bmp');
I3(1:480,1:640,24)=imread('e:\experiments\memc\response\bottom\155.bmp');
I3(1:480,1:640,25)=imread('e:\experiments\memc\response\bottom\160.bmp');
I3(1:480,1:640,26)=imread('e:\experiments\memc\response\bottom\165.bmp');
I3(1:480,1:640,27)=imread('e:\experiments\memc\response\bottom\170.bmp');
I3(1:480,1:640,28)=imread('e:\experiments\memc\response\bottom\175.bmp');
I3(1:480,1:640,29)=imread('e:\experiments\memc\response\bottom\180.bmp');
I3(1:480,1:640,30)=imread('e:\experiments\memc\response\bottom\185.bmp');
I3(1:480,1:640,31)=imread('e:\experiments\memc\response\bottom\190.bmp');
I3(1:480,1:640,32)=imread('e:\experiments\memc\response\bottom\195.bmp');
```

```
I3(1:480,1:640,33)=imread('e:\experiments\memc\response\bottom\200.bmp');
I3(1:480,1:640,34)=imread('e:\experiments\memc\response\bottom\205.bmp');
I3(1:480,1:640,35)=imread('e:\experiments\memc\response\bottom\210.bmp');
I3(1:480,1:640,36)=imread('e:\experiments\memc\response\bottom\215.bmp');
I3(1:480,1:640,37)=imread('e:\experiments\memc\response\bottom\220.bmp');
I3(1:480,1:640,38)=imread('e:\experiments\memc\response\bottom\225.bmp');
I3(1:480,1:640,39)=imread('e:\experiments\memc\response\bottom\230.bmp');
I3(1:480,1:640,40)=imread('e:\experiments\memc\response\bottom\235.bmp');
I3(1:480,1:640,41)=imread('e:\experiments\memc\response\bottom\240.bmp');
I3(1:480,1:640,42)=imread('e:\experiments\memc\response\bottom\245.bmp');
I3(1:480,1:640,43)=imread('e:\experiments\memc\response\bottom\250.bmp');
I3(1:480,1:640,44)=imread('e:\experiments\memc\response\bottom\255.bmp');
I3(1:480,1:640,45)=imread('e:\experiments\memc\response\bottom\260.bmp');
I3(1:480,1:640,46)=imread('e:\experiments\memc\response\bottom\265.bmp');
I3(1:480,1:640,47)=imread('e:\experiments\memc\response\bottom\270.bmp');
I3(1:480,1:640,48)=imread('e:\experiments\memc\response\bottom\275.bmp');
I3(1:480,1:640,49)=imread('e:\experiments\memc\response\bottom\280.bmp');



%for i=1:49
  % o1(i)=I3(240,320,i);
 %  p1(i)=I3(400,400,i);
 %   q1(i)=I3(50,50,i);
```

```
%end
%x=(40:5:280);
%figure;
%plot(x,o1,'b*--')
%hold on
%plot(x,p1,'b*--')
%plot(x,q1,'b*--')

%%% Load the original images%%
I11=double(imread('e:\experiments\memc\newetched\a5b3-6\1.bmp'));
I21=double(imread('e:\experiments\memc\newetched\a5b3-6\2.bmp'));
I31=double(imread('e:\experiments\memc\newetched\a5b3-6\3.bmp'));
I41=double(imread('e:\experiments\memc\newetched\a5b3-6\4.bmp'));
I51=double(imread('e:\experiments\memc\newetched\a5b3-6\5.bmp'));
I61=double(imread('e:\experiments\memc\newetched\a5b3-6\6.bmp'));

x=(40:5:280);
Itop=cast(I1,'double');
Imiddle=cast(I2,'double');
Ibottom=cast(I3,'double');
Itop=Itop(50:450,50:440,:);
Imiddle=Imiddle(50:450,50:440,:);
Ibottom=Ibottom(50:450,50:440,:);
```

```
%I1=I(50:450,50:440,:);
 I21=I21(50:450,50:440);
%dummy=zeros(1:401,1:391,1:49);
for i=1:401
   for j=1:391
      dummy1(1:49)=Itop(i,j,:);
      dummy2(1:49)=Imiddle(i,j,:);
      dummy3(1:49)=Ibottom(i,j,:);
      n1=find(dummy1>I21(i,j),1,'first');
      if n1==1
         n2=find(dummy2>I21(i,j),1,'first');
         if n2==1
            n3=find(dummy3>I21(i,j),1,'first');
            if n3==1
               power=x(2)-5*(dummy3(2)-I21(i,j))/(dummy3(2)-dummy3(1));
               dummy(i,j,:)=Ibottom(i,j,:);%save matrix for set 2 to 6

            elseif isempty(n3)
              if dummy3(49)==dummy3(48)
                 power=x(49);
              else
```

```
                power=x(40)+45*(I21(i,j)-dummy3(40))/(dummy3(49)-dummy3(40));
            end
            dummy(i,j,:)=Ibottom(i,j,:);
        else
            power=x(n3-1)+((I21(i,j)-dummy3(n3-1))/(dummy3(n3)-dummy3(n3-1)))*5;
            dummy(i,j,:)=Ibottom(i,j,:);
        end
    else
        power=x(n2-1)+((I21(i,j)-dummy2(n2-1))/(dummy2(n2)-dummy2(n2-1)))*5;
        dummy(i,j,:)=Imiddle(i,j,:);
    end
else
    power=x(n1-1)+((I21(i,j)-dummy1(n1-1))/(dummy1(n1)-dummy1(n1-1)))*5;
    dummy(i,j,:)=Itop(i,j,:);
end
I12(i,j)=0.7*power;
end
end



I11=I11(50:450,50:440);
for i=1:401
  for j=1:391
```

```
        %dummy(1:49)=I1(i,j,:);
        dummy4=dummy(i,j,:);
        n=find(dummy4>I11(i,j),1,'first');
        if n==1
           power=x(1);
        elseif isempty(n)
           power=x(49);
        else
           if dummy4(n)==dummy4(n-1)
              power=x(n);
            else
              power=x(n-1)+((I11(i,j)-dummy4(n-1))/(dummy4(n)-dummy4(n-1)))*5;
           end
        end
        if power<0
           power=-power;
        else
           power=power;
        end
              I111(i,j)=0.7*power;
    end
end
```

```
I31=I31(50:450,50:440);


for i=1:401
   for j=1:391
      dummy4=dummy(i,j,:);
      n=find(dummy4>I31(i,j),1,'first');

      if n~=1&~isempty(n)
         if dummy4(n)==dummy4(n-1)
            power=x(n);
         else
            power=x(n-1)+((I31(i,j)-dummy4(n-1))/(dummy4(n)-dummy4(n-1)))*5;
         end

      elseif n==1
         if dummy4(2)==dummy4(1)
            power=x(1);
         else
         power=x(2)-5*(dummy4(2)-I31(i,j))/(dummy4(2)-dummy4(1));
         end
      elseif isempty(n)
                power=x(49);
```

```
        end


 if power<0
            power=0;
        else
            power=power;
        end
          I13(i,j)=0.7*power;
    end
end



I41=I41(50:450,50:440);
for i=1:401
    for j=1:391
        dummy4=dummy(i,j,:);
        n=find(dummy4>I41(i,j),1,'first');


        if n~=1&~isempty(n)
            if dummy4(n)==dummy4(n-1)
              power=x(n);
            else
              power=x(n-1)+((I41(i,j)-dummy4(n-1))/(dummy4(n)-dummy4(n-1)))*5;
```

```
            end


        elseif n==1
            if dummy(2)==dummy(1)
                power=x(1);
            else
            power=x(2)-5*(dummy4(2)-I41(i,j))/(dummy4(2)-dummy4(1));
            end
        elseif isempty(n)


                power=x(49);


        end
        if power<0
            power=0;
        else
            power=power;
        end


        I14(i,j)=0.7*power;
    end
end
I51=I51(50:450,50:440);
```

```
for i=1:401
   for j=1:391
      dummy4=dummy(i,j,:);
      n=find(dummy4>I51(i,j),1,'first');

      if n~=1&~isempty(n)
         if dummy(n)==dummy(n-1)
            power=x(n);
         else
            power=x(n-1)+((I51(i,j)-dummy4(n-1))/(dummy4(n)-dummy4(n-1)))*5;
         end

      elseif n==1
         if dummy4(2)==dummy4(1)
            power=x(1);
         else
         power=x(2)-5*(dummy4(2)-I51(i,j))/(dummy4(2)-dummy4(1));
         end
      elseif isempty(n)

            power=x(49);

      end
```

```
        if power<0
            power=0;
        else
            power=power;
        end
         I15(i,j)=0.7*power;
    end
end



I61=I61(50:450,50:440);
for i=1:401
    for j=1:391
        dummy4=dummy(i,j,:);
        n=find(dummy4>I61(i,j),1,'first');
        if n~=1&~isempty(n)
            if dummy4(n)==dummy4(n-1)
               power=x(n);
            else
               power=x(n-1)+((I61(i,j)-dummy4(n-1))/(dummy4(n)-dummy4(n-1)))*5;
            end


        elseif n==1
```

```
        if dummy4(2)==dummy4(1)
            power=x(1);
        else
        power=x(2)-5*(dummy4(2)-I61(i,j))/(dummy4(2)-dummy4(1));
        end
    elseif isempty(n)

            power=x(49);

    end
    if power<0
        power=0;
    else
        power=power;
    end

    I16(i,j)=0.7*power;
  end
end
```

```
%%% save the adjusted images%%
 I111=uint8(I111);
imwrite( I111,'e:\experiments\memc\newetched_calibrated\a5b3-6\1.bmp','bmp');
I12=uint8(I12);
imwrite(I12,'e:\experiments\memc\newetched_calibrated\a5b3-6\2.bmp','bmp');
I13=uint8(I13);
imwrite(I13,'e:\experiments\memc\newetched_calibrated\a5b3-6\3.bmp','bmp');
I14=uint8(I14);
imwrite(I14,'e:\experiments\memc\newetched_calibrated\a5b3-6\4.bmp','bmp');
I15=uint8(I15);
imwrite(I15,'e:\experiments\memc\newetched_calibrated\a5b3-6\5.bmp','bmp');
I16=uint8(I16);
imwrite(I16,'e:\experiments\memc\newetched_calibrated\a5b3-6\6.bmp','bmp');
```

References

1. Higashino, Toshiyuki et al. “Temperature gradient and heat balance at the solid-liquid interface in CZ silicon growth”, Journal of the Vacuum Society of Japan, v 43, n 5, p 603-606, 2000.
2. L. C. Garone, C. V. Hari Rao, A. D. Morrison, T. Surek, and K. V. Ravi. “Orientation dependence of defect structure in efg silicon ribbons”, Applied Physics Letters, 29(8) 492:511, 1976.
3. Sheoran, Manav et al. “ Bulk lifetime and efficiency enhancement due to gettering and hydrogenation of defects during cast multicrystalline silicon solar cell fabrication”, Solid-State Electronics, v 52, n 5, p 612-617, May 2008
4. Shimokawa, Ryuichi et al. “Solar characteristics of high-efficiency polycrystalline silicon solar cells using SOG-cast wafers”, Japanese Journal of Applied Physics, Part 1: Regular Papers & Short Notes, v 26, n 10, p 1667-1673, Oct 1987
5. Bei Wu et al. “Bulk multicrystalline silicon growth for photovoltaic (PV) application”, Journal of Crystal Growth 310 (2008) 2178–2184
6. Hewitt, Geoff F. and Pugh, Simon J. “Approximate design and costing methods for heat exchangers”, Heat Transfer Engineering, v 28, n 2, p 76-86, February 2007
7. C.K. Bhihe et. al. “Residual stresses in crystal growth”, *Journal of Crystal Growth.* Vol. 137. p. 86-90. 1994.B. Chalmers.
8. J.C. Lambropoulos, et. al. “Plastic deformation influence on stress generated during silicon sheet growth at high speeds”, *Journal of Crystal Growth.* Vol. 65. p. 324-330. 1983

9. T. Zheng. “A study of residual stresses in thin anisotropic (silicon) plates”, PhD thesis, 2000
10. J.P. Kalejs. “Modeling contributions in commercialization of silicon ribbon growth from the melt”. *Journal of Crystal Growth*, 230 (1-2) p.10-21, 2001.
11. j. f. flavenot. “Handbook of measurement of residual stresses”, Society for Experimental Mechanics ,35 – 48; 1996
12. Todd, R.I. et al. “Thermal residual stresses and their toughening effect in Al2O3 platelet reinforced glass”, Acta Materialia, v 47, n 11, p 3233-40, 8 Sept. 1999
13. Peitl, O. and Zanotto. E.D. “Thermal shock properties of chemically toughened borosilicate glass”, Source: Journal of Non-Crystalline Solids, v 247, p 39-49, May 1999
14. Neto, P., Alfaiate, J.and Vinagre, J. “ Numerical modelling of concrete beams reinforced with pre-stressed CFRP”, International Journal of Fracture, v 157, n 1-2, p 159-173, 2009
15. Iskhakov, I. and Ribakov. “Two-layer pre-stressed beams consisting of normal and steel fibered high strength concrete”, Y. Source: Materials and Design, v 29, n 8, p 1616-22, 2008
16. R. G. Seidensticker and R. H. Hopkins. “Silicon ribbon growth by the dendritic web process”. Journal of Crystal Growth, 50(1):221–235, 1980.
17. V. Garcia. “Effect of Dislocation Density on Residual Stress in Edge-Defined Film-Fed Growth Silicon Wafers”, Master Thesis

18. He, S. Danyluk, S.; Tarasov, I.; Ostapenko, S. "Residual stresses in polycrystalline silicon sheet and their relation to electron-hole lifetime", Applied Physics Letters, v 89, n 11, p 111909-1-3, 11 Sept. 2006
19. K. Ramesh and S.K. Mangal. "Data acquisition techniques in digital photoelasticity: a review.", Optics and lasers in engineering, 30:53–75, 1998.
20. E. A. Patterson. "Digital photoelasticity: principles, practices and potential.", Strain, 38:27–39, 2002.
21. P. Doig and P.E.J. Flewitt. "Non-destructive stress measurement using x-ray diffraction methods". NDT International, 11(3):127–131, 1978.
22. S. Shin and H. Yano. "Evaluation of error of x-ray residual stress measurement method. In Japan Soc. Instrum. & Control Eng, Tokyo, editor, Recent Advances in Weighing Technology and Force Measurement", 10th International Conference of the IMEKO Technical Committee TC-3 on Measurement of Force and Mass, Kobe, Japan, 1984.
23. A. S. M. Y. Munsi, A. J. Waddell, and C. A. Walker. "A method for determining x-ray elastic constants for the measurement of residual stress", Strain, 39(1):3–10, 2003.
24. Baczmanski, A.; Braham, C.; Seiler, W.; Shiraki, N. "Multi-reflection method and grazing incidence geometry used for stress measurement by X-ray diffraction", Source: Surface & Coatings Technology, v 182, n 1, p 43-54, 1 April 2004
25. K. Y. Kim and W. Sachse. "The theory of thermodynamic-acoustoelastic stress gauge", Journal of Applied Physics, 80(9):4934–4943, 1996
26. H. R. Dorfi, H. R. Busby, and M. Janssen. "Acoustoelasticity: Ultrasonic stress field reconstruction", Experimental Mechanics, 36(4):325–332, 1996.

27. R. B. thompson, W. Y. lu, and A. A. clark. “Handbook of measurement of residual stresses”, Society for Experimental Mechanics, 149 – 178, 1996
28. R. B. thompson, et al. “Non-destructive evaluation, application to materials processing”, American Society for Metals, 137 – 145,1984
29. A. T. Andonian and S. Danyluk. “ Non-destructive determination of residual-stresses in circular silicon-wafers”, Mechanics Research Communications,11(2):97–104, 1984
30. A. T. Andonian and S. Danyluk. “Residual-stresses of thin, short rectangular-plates”, Journal of Materials Science, 20(12):4459–4464, 1985.
31. K. Ghaffari, B. Wang, S. Danyluk, M. Billone, and G. Pharr. “Optical interferometric determination of in-plane residual stresses in sio2 films on silicon substrates”, Materials Evaluation, 54(10):1167–1170, 1996
32. Y. Kwon, S. Danyluk, L. Bucciarelli, and J. P. Kalejs. “Residual-stress measurement in silicon sheet by shadow moire interferometry”, Journal of Crystal Growth, 82(1-2):221–227, 1987.
33. H. W. Park and S. Danyluk. “Residual-stress measurement in filament- evaporated aluminum films on single-crystal silicon-wafers”, Journal of Materials Science, 26(1):23–27 1991.
34. Paradowska, A.M. et al. “Residual stress distribution in steel butt welds measured using neutron and synchrotron diffraction”, Journal of Physics Condensed Matter, v 21, n 12, 2009
35. Mari, D. et al. “Measurement of residual thermal stress in WC-Co by neutron diffraction”, International Journal of Refractory Metals & Hard Materials, v 27, n 2, p 282-7, March 2009

36. Tieyu Zheng and Steven Danyluk. “Study of stresses in thin silicon wafers with near-infrared phase stepping photoelasticity”, Journal of materials research, vol. 17 no. 1, Jan 2002

37. S. He. Near Infrared Photoelasticity of Polycrystalline Silicon and it’s Relation to In-plane Residual Stresses, PhD thesis, 2005

38. S. He and S. Danyluk. “Residual Stress Characterization for Solar Cells by Infrared Polariscopy”, National Center for Photovoltaics and Solar Program Review Meeting, Denver Colorado, 2003.

39. T. Zheng and S. Danyluk. “Nondestructive measurement of in plane residual stress in thin silicon substrates by infrared transmission”, Matl. Evaluation, vol 50, no 10, Oct 2001, pp1227-1233

40. S. He, T. Zheng and S. Danyluk. “Analysis and determination of stress-optic coefficient of thin single crystal silicon samples” Journal of applied physics, vol 96, number 6, 15 Dec 2004, pp3103-3109

41. David Brewster. “On the communication of the structure of doubly refracting crystals to glass, muriate of soda, flour spar and other substances by mechanical compression and dilatation”, Philosophical Transactions of the Royal Society, pages 156–178, 1816.

42. D. Brewster. “Experiments on the depolarization of light as exhibited by various mineral, animal and vegetable bodies with a reference of the phenomena to the general principle of polarization”, Phil. Tras. 1815, pp.29-53

43. E.G. Coker and L.N.G. Filon. “A Treatise on Photoelasticity”, Cambridge University Press, 1931

44. K. Ramesh. “Digital photoelasticity advanced techniques and applications”, Springer-Velag, New York, 2000.
45. F. W. Hecker and B. Morche. “Computer-aided measurement of relative retardations in plane photoelalsticity”, Experimental Stress Analysis, pages 535–543, 1986
46. Meyer, C. et al. “Nonlinear optical mapping of silicon carbide polytypes in 6H-SiC epilayers”, Applied Physics Letters, v 69, n 15, p 2243, Oct 7 1996
47. Seong-Min Jeong and Kitamura, T. “Structural transformation of single crystal silicon under uniaxial stress”, Key Engineering Materials, v 345-346, pt.2, p 963-6, 2007
48. Horie, H. et al. “Photoviscoelastic stress and strain analysis of a circular disk under nonproportional orthogonal compression”, Nippon Kikai Gakkai Ronbunshu, A Hen/Transactions of the Japan Society of Mechanical Engineers, Part A, v 61, n 591, p 2489-2494, Nov 1995
49. Cloud, Gary. “Optical methods in experimental mechanics: Part 34: Photoelasticity VI - The circular polariscope”, Experimental Techniques, v 32, n 6, p 21-23, 2008
50. Jing-Fung Lin et al. “Measurements of the principal axis and phase retardation using a new circular polariscope and the Senarmont setup”, Proceedings of the SPIE - The International Society for Optical Engineering, v 5852, n 1, p 240-4, 2005
51. Umezaki, E. and Pinit, P. “Digitally whole-field analysis of isoclinic parameter in photoelasticity by four-step color phase-shifting technique”, Optics and Lasers in Engineering, v 45, n 7, p 795-807, July 2007

52. Yoneyama, S. et al. “Instantaneous phase-stepping photoelasticity for the study of crack growth behavior”, Proceedings of the SEM Annual Conference and Exposition on Experimental and Applied Mechanics 2007, v 2, p 720-731, 2007,
53. Pinit, P. Susumu, T.; Umezaki, E. “Determination of principal-stress directions by three-step color phase shifting technique”, Key Engineering Materials, v 321-323, pt.2, p 1284-7, 2006
54. Jones, F.R. et al. “Phase-stepping photoelasticity for the measurement of interfacial shear stress in single fibre composites”, Composites Part A (Applied Science and Manufacturing), v 37, n 2, p 216-21, Feb. 2006
55. Ramji, M.and Ramesh, K. “A new six-step phase shifting technique using mixed - Polariscope in Digital Photoelasticity”, Key Engineering Materials, v 326-328 I, p 35-38, 2006
56. Matchett, A.J.; O'Neill, J.C.; Shaw, A.P. “Stress distributions in 2-dimensional, wedge hoppers with circular arc stress orientation - a co-ordinate-specific Lame-Maxwell model”, Powder Technology, v 187, n 3, p 298-306, 20 Nov. 2008
57. T. Liu, A. Asundi and C. boay. “Full field automated photoelasticity suing two-load-step method”, Opt. Eng. 40(8) 1629-1635, Aug 2001
58. Giovanni Petrucci & Gaetano Restivo. “Automated Stress Separation Along Stress Trajectories”, Society for Experimental Mechanics 2007, pp 733-743
59. M. Ramji, K. Ramesh. “Whole field evaluation of stress components in digital photoelasticity: Issues, implementation and application”, Optics and Lasers in Engineering 46 , 257–271 2008

60. Ramji, M. et al. “Assessment of autonomous phase unwrapping of isochromatic phase maps in digital photoelasticity”, Sadhana - Academy Proceedings in Engineering Sciences, v 33, n 1, p 27-44, February 2008
61. Baldi, Antonio et al. “A temporal phase unwrapping algorithm for photoelastic stress analysis”, Optics and Lasers in Engineering, v 45, n 5, p 612-617, May 2007, Optical Methods in Experimental Mechanics
62. Siegmann, P. et al. “A robust approach to demodulating and unwrapping phase-stepped photoelastic data”, Experimental Mechanics, v 45, n 3, p 278-289, June 2005
63. E. A. Patterson, W. Ji, and Z. F. Wang. “ On image analysis for birefringence measurements in photoelasticity”, Optics and Lasers in Engineering, 28(1):17 – 36, 1997.
64. W. Ji and E. A. Patterson. “Simulation of errors in automated photoelasticity. Experimental Mechanics”, 38(2):132 – 139, 1998.

,